

*Digital Comprehensive Summaries of Uppsala Dissertations
from the Faculty of Science and Technology 2644*

Nanoscale Engineering with Ions: Formation of Nanostructures and Tuning of Material Properties

RAJDEEP KAUR



ACTA UNIVERSITATIS
UPSALIENSIS
2026



UPPSALA
UNIVERSITET

Dissertation presented at Uppsala University to be publicly examined in Heinz-Otto Kreiss (Å101195), Ångströmlaboratoriet, Lägerhyddsvägen 1, Uppsala, Friday, 10 April 2026 at 09:15 for the degree of Doctor of Philosophy. The examination will be conducted in English. Faculty examiner: Dr Katharina Lorenz (University of Lisbon, Portugal).

Abstract

Kaur, R. 2026. Nanoscale Engineering with Ions: Formation of Nanostructures and Tuning of Material Properties. *Digital Comprehensive Summaries of Uppsala Dissertations from the Faculty of Science and Technology* 2644. 85 pp. Uppsala. ISBN 978-91-513-2751-8.

Understanding ion-matter interactions is fundamental to advancing nanoscale engineering using ions. This thesis presents a comprehensive investigation into energy deposition by energetic ions across the keV-MeV energy regime and its correlation to observable changes in the structural and material properties. By expanding the investigation across different material systems, *viz.*, crystalline, polymeric and amorphous, this thesis provides a unified perspective on energy transfer processes and, at the same time, illustrates how they can be utilised to modify material properties.

The first section of the thesis focuses on the nanoscale structural modification induced by MeV ions. The impact of energy deposition, in the MeV energy regime, on the formation of surface nanostructures in single-crystal CaF₂ and nanoscale ion tracks in polyimide foils is investigated. In polyimide foils, the effect of the evolution of the ion charge state on energy deposition, and consequently on ion track formation, is studied. Extending this approach, amorphous TiO₂ films are investigated under separate and sequential irradiation by MeV ions and keV electrons. This analysis across different materials provides a broader understanding of the relationship between energy transfer processes and structural modifications.

The second section of the thesis focuses on understanding how keV ion implantation can be used to introduce controlled local structural modifications in Pd/TiO₂/Pd memristors to tune their functional properties. The ion-induced structural modifications are correlated with variations in resistive switching properties. Complementary ¹⁸O isotope tracing with nuclear reaction analysis is used to probe atomic migration under applied voltage in ion-implanted memristors, revealing how ion-induced modifications influence atomic migration, which in turn governs the switching mechanisms.

Overall, this thesis demonstrates that energetic ions can systematically induce modifications across material systems and energy regimes. By correlating energy deposition with observed material modifications, the thesis provides a coherent framework for understanding how fundamental ion-matter interactions lead to structural changes and influence the material properties. These insights provide a general perspective on employing energetic ions as a potential tool for nanoscale engineering, ranging from the formation of nanostructures to the tuning of material properties.

Keywords: Ion irradiation, ion implantation, calcium fluoride, polyimide, titanium dioxide, material modification, nanostructures, nanopores, memristors, resistive switching

Rajdeep Kaur, Department of Physics and Astronomy, Materials Physics, 516, Uppsala University, SE-751 20 Uppsala, Sweden. Department of Physics and Astronomy, Applied Nuclear Physics, Box 516, Uppsala University, SE-751 20 Uppsala, Sweden. Tandem Laboratory, Box 529, Uppsala University, SE-75120 Uppsala, Sweden.

© Rajdeep Kaur 2026

ISSN 1651-6214

ISBN 978-91-513-2751-8

URN urn:nbn:se:uu:diva-580192 (<http://urn.kb.se/resolve?urn=urn:nbn:se:uu:diva-580192>)

To my family

List of Papers

This thesis is based on the following papers, referred to in the text by their Roman numerals.

- I. Surface characterisation of CaF₂ crystals irradiated with MeV ions below charge state equilibrium**
Kaur, R., Ström, P., Primetzhofer, D. *Nuclear Instruments and Methods in Physics Research B*, 536:132–137 (2023)
DOI: 10.1016/j.nimb.2023.01.004
- II. Ion track formation and nanopore etching in polyimide: Possibilities in the MeV ion energy regime**
Kaur, R., Eljamal, G., Tran, T. T., Primetzhofer, D., Ström, P. *Macromolecular Materials and Engineering*, 309(1):2300232 (2023)
DOI: 10.1002/mame.202300232
- III. Charge equilibration and irradiation damage threshold for MeV ions in polyimide**
Kaur, R., Primetzhofer, D., Ström, P. *Nuclear Instruments and Methods in Physics Research B*, 551:165335 (2024)
DOI: 10.1016/j.nimb.2024.165335
- IV. Crystallisation of amorphous TiO₂ by energetic ions and electrons: Evidence of antagonistic effects**
Kaur, R., Tran, T. T., Pálsson, G. K., Primetzhofer, D., Ström, P. (*Manuscript under review*)
- V. Tuning TiO₂ memristors by defect engineering: From short-term memory to recoverable long-term resistance states**
Kaur, R., Tran, T. T., Lindblad, R., Zhang, Z., Primetzhofer, D., Ström, P. (*Manuscript*)
- VI. Probing oxygen migration after resistive switching in ion-implanted TiO₂ memristors**
Kaur, R., Primetzhofer, D., Ström, P. (*Manuscript*)

Reprints for the published manuscripts were made under the terms of the Creative Commons Attribution Licence (CC BY).

My contributions to the included papers

Paper I: Planned the investigation, conducted the experiments, analysed the data, interpreted the results together with co-authors, and wrote the initial manuscript.

Paper II: Participated in planning the study, conducted the experiments together with co-authors, analysed the data, interpreted the results together with co-authors, and wrote the initial manuscript.

Paper III: Participated in planning the study, conducted the experiments, analysed the data, interpreted the results together with co-authors, and wrote the initial manuscript.

Paper IV: Participated in planning the study, conducted the experiments together with co-authors, analysed the data, interpreted the results together with co-authors, and wrote the initial manuscript.

Paper V: Participated in planning the study, conducted the experiments together with co-authors, analysed the data, interpreted the results together with co-authors, and wrote the initial manuscript.

Paper VI: Participated in planning the study, conducted the experiments, analysed the data, interpreted the results together with co-authors, and wrote the initial manuscript.

This thesis is partially based on the licentiate thesis titled ‘Case Studies in Ion Beam Assisted Nanostructure Engineering’, Rajdeep Kaur, Uppsala University (2024). All chapters are edited and expanded.

Generative AI was utilised to enhance the clarity of the text and for the Swedish translation of the summary.

Other papers not included in the thesis

- VII. Thin film sputter-deposited from EUROFER97 in argon and deuterium atmosphere: Material properties and deuterium retention**
Pitthan, E., Petersson, P., Tran, T. T., Moldarev, D., Kaur, R., Shams-Latifi, J., Ström, P., Hans, M., Rubel, M., Primetzhofer, D. *Nuclear Materials and Energy*, 34:101375 (2023)
DOI: 10.1016/j.nme.2023.101375
- VIII. Sputter-deposited ultra-thin film stacks from EUROFER97 and tungsten: characterisation and interaction with low-energy D and He ions**
Shams-Latifi, J., Pitthan, E., Tran, T. T., Kaur, R., Primetzhofer, D. *Materials Research Express*, 11:016518 (2024)
DOI: 10.1088/2053-1591/ad1f97
- IX. Position-selective introduction of ferromagnetism on the micro- and nanoscale in a paramagnetic thin palladium film**
Ström, P., Vantaraki, C., Kaur, R., Tran, T. T., Nagy, G., Kapaklis, V., Primetzhofer, D. *Physica Status Solidi (RRL)- Rapid Research Letters*, 18:2400053 (2024)
DOI: 10.1002/pssr.2024000053

Contents

1. Introduction	13
1.1. Material systems investigated.....	14
1.2. Scope and organisation of the thesis.....	15
2. Ion-solid interactions.....	18
2.1. Binary collisions.....	18
2.2. Mean equilibrium charge.....	20
2.3. Stopping power and range.....	21
3. Ion beam materials modification.....	26
3.1. Nanostructure engineering.....	26
3.2. Modification of material properties.....	28
3.3. Theoretical models	29
4. Sample preparation.....	32
4.1. Ion irradiation and implantation	32
4.2. Wet chemical processing.....	34
4.3. Magnetron sputtering.....	35
5. Characterisation and analysis	37
5.1. Ion Beam Analysis (IBA).....	37
5.1.1. Rutherford Backscattering Spectrometry (RBS)	38
5.1.2. Elastic Recoil Detection Analysis (ERDA).....	40
5.1.3. Nuclear Reaction Analysis (NRA)	41
5.2. Microscopy.....	42
5.2.1. Scanning Electron Microscopy (SEM).....	43
5.2.2. Transmission Electron Microscopy (TEM).....	44
5.2.3. Atomic Force Microscopy (AFM).....	46
5.3. X-ray characterisation.....	47
5.3.1. Total X-ray scattering.....	47
5.3.2. X-ray Photoelectron Spectroscopy	49
5.4. Electrical characterisation	51
6. Results and discussion.....	52

6.1. Nanostructure engineering using MeV ions	52
6.1.1. Surface nanostructures	52
6.1.2. Bulk nanostructures	53
6.1.3. Dependence of nanostructures on properties of MeV ions ...	55
6.1.4. Charge equilibration	57
6.2. Sequential effects of MeV ion and keV electron irradiation	58
6.3. Tuning of resistive switching properties.....	60
7. Conclusions and outlook	67
8. Sammanfattning.....	70
Acknowledgements.....	73
References.....	75

Abbreviations

AFM	Atomic Force Microscopy
BE	Bottom Electrode
BW model	Bond Weakening model
CasP	Convolution approximation for swift Particles
CE model	Coulomb Explosion model
CF	Conductive Filament
CMOS	Complementary Metal-Oxide Semiconductor
EBS	Elastic Backscattering Spectrometry
EDS	Energy Dispersive X-ray Spectroscopy
ESPNN	Electronic Stopping Power Neural Network
FFT	Fast Fourier Transform
FIB	Focussed Ion Beam
GUI	Graphical User Interface
HAXPES	Hard X-ray Photoelectron Spectroscopy
HCI	Highly Charged Ions
HRS	High Resistance State
IAEA	International Atomic Energy Agency
IBA	Ion Beam Analysis
IBANDL	Ion Beam Analysis Nuclear Data Library
IDEA model	Ionization-Diffusion-Explosion-Amorphization model
LRS	Low Resistance State
MFC	Mass Flow Controller
NRA	Nuclear Reaction Analysis
PDF	Pair Distribution Function
PID	Proportional, Integral, Derivative
PIXE	Particle-induced X-ray Emission
QCM	Quartz Crystal Microbalance
RBS	Rutherford Backscattering Spectrometry
rms	Root mean square
SAED	Selected Area Electron Diffraction
SEM	Scanning Electron Microscopy
SHI	Swift Heavy Ions

SPM	Scanning Probe Microscopy
SRIM	Stopping and Range of Ions in Matter
STEM	Scanning Transmission Electron Microscopy
STX model	Exciton Self-Trapping model
TE	Top Electrode
TEM	Transmission Electron Microscopy
ToF-ERDA	Time-of-Flight Elastic Recoil Detection Analysis
TRIM	Transport of Ions in Matter
TS model	Thermal Spike model
XPS	X-ray Photoelectron Spectroscopy
XRD	X-ray Diffraction

1. Introduction

The interaction of energetic ions with matter constitutes a fundamental focus in atomic and solid-state physics. When an energetic ion traverses through a material, it transfers energy to the target atoms and electrons through several complex processes. These energy transfer processes drive the material away from thermodynamic equilibrium, resulting in modifications in structural, electrical, optical or mechanical properties. As energy deposition by ions occurs on comparably shorter time scales than those for thermal or structural equilibration, ions can drive material into transient states that are not accessible under equilibrium conditions. Thereby, ions can create non-equilibrium synthesis conditions, allowing stabilisation of metastable conditions and defect configurations that may not be accessible through conventional thermodynamic synthesis methods [1,2].

Ion-induced nanostructuring and modification of material properties have been widely studied using ions with kinetic energies ranging from a few tens of eV to GeV [3–11]. The ions interact with materials by transferring energy via electronic processes and nuclear collision cascades, with the dominant energy loss mechanism depending on the ion energy. At eV or a few keV energies, energy transfer is primarily through elastic collisions with target nuclei, while electronic processes play a less significant role. These nuclear collisions lead to displacement cascades, producing vacancies, interstitials, and defect clusters as well as localised heating in the material. At GeV energies, which lie at the other extreme of the energy scale employed in ion-beam induced nanoengineering, energy loss is dominated by fast electronic processes, such as excitation and ionisation. These electronic interactions result in highly localised energy deposition along the ion trajectory. The subsequent relaxation of this excited electronic system through processes such as electron-phonon coupling can lead to transient local heating and structural modification at the nanometre length scale and picosecond time scale. Eventually, the material affected by the passage of ions relaxes into a state that may differ from the original configuration, e.g., in crystallinity or chemical bonding. Such a narrow trail of modified material, created by the passage of an energetic ion, is known as an ion track. Between these extreme energy regimes lie ions with MeV or a few hundred keV energy, where both inelastic electronic excitations and elastic nuclear collisions can play a significant role in energy transfer.

The energy deposition can also be tuned by ion properties such as mass and charge. By understanding these energy-transfer processes and their complex interplay, a high degree of control can be achieved over the type, position, and extent of ion-induced material modification. For example, depth selectivity can be achieved by adjusting the ion energy, while areal selectivity can be controlled by using a mask or reducing the scan area of the ion beam. Thus, ion beam-based methods offer reliable, highly reproducible and efficient ways to produce nanostructures and tailor material properties, including structural, electronic, and optical properties.

In addition to ion energies, the energy transfer processes and resulting modifications depend on intrinsic material properties such as density, composition, thermal conductivity and crystallinity. For example, an ion entering a high-density material will interact more frequently, resulting in greater energy loss over a shorter distance compared to a lower-density material. Therefore, investigating how ions interact and modify across different material systems can provide insights into the key parameters that govern energy transfer and ion-induced modifications.

This thesis investigates how the energy deposition by energetic ions leads to modifications in the structural and functional properties across different material systems. Ions with both MeV and keV energies are used, targeting distinct effects: MeV ions for nanoscale structural modifications and keV ions for modification of functional properties. By combining these studies, this thesis aims to correlate the fundamental ion-matter interactions to observable structural and functional modifications.

1.1. Material systems investigated

In the thesis, ion beam-induced modifications are systematically studied in three distinct material systems: single crystals, polymers and amorphous metal oxide thin films.

Single crystals: Single-crystal calcium fluoride (CaF_2), cleaved along the (111) plane, was used to investigate surface nanostructures induced by MeV ions in this thesis. Single-crystal CaF_2 is regarded as a model system for studying ion-induced modifications and nanostructuring in a class of solids known as non-amorphisable insulators [12]. Non-amorphizable refers to crystalline materials of very high ionicity that are not subject to amorphisation under irradiation, e.g., LiF_2 , CaF_2 , UO_2 and ThO_2 . CaF_2 is also isostructural to materials relevant for the nuclear industry, such as UO_2 and ThO_2 , and is considered a good surrogate material for understanding radiation-induced modifications in nuclear fuel components [13]. Figure 1.1(a) shows a typical (10×10) mm^2 cross-section CaF_2 sample used for investigation in this thesis and appended papers.

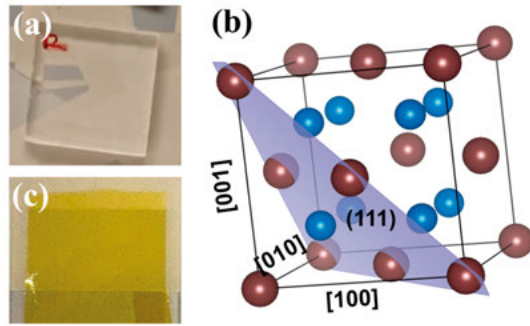


Figure 1.1 (a) CaF_2 single crystals with (10×10) mm² cross-section; (b) schematic of a unit cell of CaF_2 with the (111) plane highlighted (based on Fig. 3.3 in Paper I); (c) Kapton 30EN polyimide foil.

Polymers: Polyimide (PI) foils are used in this thesis to investigate track formation in polymeric systems using MeV ions. Nanoporous polymer membranes are widely investigated as next-generation solid-state sensors with a wide range of applications, e.g., DNA/RNA sequencing, protein profiling, water desalination, filtration and selective drug delivery [14–17]. PI has excellent mechanical strength, heat stability over a wide temperature range (-269 to 400°C) and strong chemical resistance [18], making it a promising candidate for practical nanoporous membranes and a model system for investigating ion-induced modifications. Figure 1.1(c) shows a typical Kapton 30EN PI foil used in this thesis and appended papers.

Amorphous metal oxide films: Amorphous metal oxides such as TiO_2 are of great interest for applications in high-performance and flexible electronics, transparent conductors, gas sensors, memristors, photocatalysis, optical coatings, memory devices and energy storage [19–23]. In this thesis, amorphous titanium dioxide ($\alpha\text{-TiO}_2$) films are investigated as a model system for studying ion-induced modification by both MeV and keV ions. MeV ions are used to investigate the effects of energy deposition on the ‘amorphous’ structure, and keV ions are used to investigate the effect of nuclear collision cascades and stoichiometric modification due to ion implantation on the functional properties of the films. Specifically, how keV ions influence resistive switching behaviour in Pd/ TiO_2 /Pd memristor structure is investigated in this thesis.

1.2. Scope and organisation of the thesis

The thesis starts by investigating the formation of MeV ion-induced surface nanostructures in CaF_2 single crystals and bulk nanostructures in PI foils. As discussed above, ions in the intermediate energy regime (MeV or a few hundred keV) can be used to study the complex interplay between electronic and nuclear energy losses and their coupled effects on material modification.

Additionally, MeV ions have penetration depths on the order of micrometres and, thereby, are not limited to surface or near-surface modification. These characteristics make these ‘lesser explored’ MeV ions interesting and promising candidates for both surface and bulk nanostructures. A systematic study was conducted to investigate how energy deposition in these two distinct materials and, as a result, nanostructure formation are affected by varying parameters, such as ion species and energy, in the MeV energy regime. The results for surface nanostructures are presented in **Paper I**, and for bulk nanostructures in PI foils are presented in **Paper II**. In **Paper III**, the effect of the evolution of the charge state of the ions on energy deposition in PI foils, and thereby on nanostructure formation, was studied. The experimental results were compared with simple theoretical models on charge equilibration processes.

Based on this foundation, the investigation was extended to study both the separate and sequential effects of two different energetic charged particles, *viz.*, MeV ions and keV electrons, on the third material system, *i.e.*, a-TiO₂ thin films. Although both electrons and MeV ions can induce similar modifications in a material, the energy loss processes are fundamentally different. Electrons primarily interact by electronic processes, whereas MeV ions can transfer energy by both electronic excitations and nuclear collisions. Studying the separate and sequential effects of electron and MeV ion irradiation can provide insights into the energy loss processes induced by these two charged particles, which can subsequently be used to tune material properties. The results are presented in **Paper IV**.

In addition to studying energy transfer processes and nanostructure formation with MeV ions in a-TiO₂ films, the films were also used to study ion-induced modification of memristor properties. The memristor structure consists of multiple layers, and to confine structural modifications to the nanometre-thin TiO₂ layer without affecting other layers, keV ions were used. For ions with a few keV energy, the penetration depth is on the order of nanometres, and nuclear collision-dominated energy transfer processes primarily induce localised stoichiometric changes and create defects. These localised structural changes can significantly modify both local and macroscopic material properties such as electrical conductivity. **Paper V** demonstrates how controlled keV ion implantation can be used to tune switching properties and introduce different switching modes in TiO₂-based memristors, providing insights into the relationship between structural modifications and memristor properties. Building on this, **Paper VI** investigates the underlying switching mechanism in these ion-modified memristors. ¹⁸O isotope tracking using nuclear reaction analysis (NRA) was employed to probe atomic migration in different resistance states, examining how ion-induced structural changes can influence microscopic atomic migration and thus the mechanisms governing resistive switching.

The thesis begins with an introduction to basic ion-solid interactions in Chapter 2, which gives a brief background for the results and discussions presented later. It is followed by an overview of the current status of material modification and nanostructure engineering in solids using ion beams, along with theoretical models to understand ion tracks and subsequent ion-induced nanostructure formation in Chapter 3. Chapter 4 introduces sample preparation and ion beam-based methods used for material modification in this thesis and appended papers. Chapter 5 introduces various experimental techniques and methods used for sample characterisation and analysis. All the results are summarised in Chapter 6, followed by concluding remarks and outlook in Chapter 7.

2. Ion-solid interactions

When an energetic ion enters a target material, it interacts with both the electrons and nuclei of the target. These interactions result in continuous transfer of the ion's energy to the target, giving rise to atomic displacements, electronic excitations, ionisation, and in some cases, nuclear reactions. Depending on the energy of the incoming ion, the energy transfer mechanism can be dominated by either nuclear collisions or electronic processes.

2.1. Binary collisions

The interaction between low-energy projectiles and the target nucleus can be approximated as a series of elastic binary collisions, following the laws of conservation of momentum and kinetic energy. A schematic of the binary collision is shown in Figure 2.1. Assuming the target atoms are stationary ($v_t = 0$), the equations for conservation of momentum and kinetic energy are given by:

$$M_p v_p = M_p v'_p + M_t v'_t \quad (2.1)$$

$$M_p (v_p)^2 = M_p (v'_p)^2 + M_t (v'_t)^2 \quad (2.2)$$

where $M_{p,t}$, $v_{p,t}$ and $v'_{p,t}$ are mass, initial velocity and final velocity of the projectile and target. For the projectiles scattered at an angle of θ , the kinematic factor (K_p) is defined as the ratio between the final kinetic energy (E'_p) and the initial kinetic energy (E_p) of the projectile. It is given by:

$$K_p = \frac{E'_p}{E_p} = \left[\frac{\sqrt{M_t^2 - M_p^2 \sin^2 \theta} + M_p \cos \theta}{M_t + M_p} \right]^2 \quad (2.3)$$

The kinematic factor for the recoiled target nuclei (K_t) is defined as the ratio between the final kinetic energy of the recoiled nuclei (E'_t) and initial kinetic energy of the projectile (E_p), and is given by:

$$K_t = \frac{E'_t}{E_p} = \frac{4 M_p M_t}{(M_t + M_p)^2} \cos^2 \varphi \quad (2.4)$$

where φ is the recoil angle. The energy of backscattered ions or recoiled nuclei is given by the kinematic factors, and the probability of an ion backscattering

or target nucleus recoiling at a given angle depends on the differential cross section. The differential cross section is defined as the ratio of the number of particles scattered or recoiled into a given solid angle element, $d\Omega$, to the total number of incident particles per unit area transverse to the projectile trajectories. Assuming that the incoming ion and the target nucleus interact in the Coulomb potential, the differential cross section, also called the Rutherford cross section, for the scattered ion is given by:

$$\frac{d\sigma(\theta)}{d\Omega} = \left(\frac{e^2 Z_p Z_t}{8\pi\epsilon_0 E_p}\right)^2 \frac{1}{\sin^4\theta} \frac{\left(\sqrt{M_t^2 - M_p^2 \sin^2\theta} + M_t \cos\theta\right)^2}{\sqrt{M_t^2 - M_p^2 \sin^2\theta}} \quad (2.5)$$

for the recoiled nucleus:

$$\frac{d\sigma(\varphi)}{d\Omega} = \left(\frac{e^2 Z_p Z_t}{8\pi\epsilon_0 E_p}\right)^2 \frac{(M_t + M_p)^2}{M_t^2 \cos^3\varphi} \quad (2.6)$$

where Z_p and Z_t are the atomic numbers of the projectile and target atom, respectively, e is the elementary charge, and ϵ_0 is the vacuum permittivity.

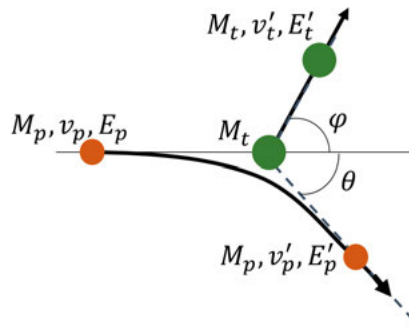


Figure 2.1 Schematic for binary collision between a projectile ion (orange) of mass M_p and initial energy E_p and a stationary target (green) of mass M_t . The projectile ion is scattered at an angle θ with energy (E'_p) and the target atom recoils with an angle φ with energy (E'_t).

The projectile ions can also lose energy by interacting with the electronic system of the target atoms through ionisation or excitation, and this is the dominant mechanism of energy loss for ions with energies higher than a few tens of keV/u. The ejected electrons can further ionise or excite other atoms before losing their energy. The inner shell vacancy, created by ionisation or excitation, is filled by an outer shell electron, resulting in the de-excitation of the target atoms and the release of energy equal to the difference between the energies of the excited and de-excited state. The energy is either released in the form of a photon (characteristic X-rays) or transferred to another electron, which is then ejected from the atom (Auger electron).

2.2. Mean equilibrium charge

The traversing ions may both lose electrons to or capture electrons from atoms in a target material. When the ion enters the target, the mean equilibrium charge state (q_{eq}) of the ion-target system is reached when an equilibrium between average electron loss and capture is achieved. The probability of electron loss by the projectile ion increases with ion velocity (v_p), and thus the equilibrium between electron loss and capture occurs at a higher charge for higher velocity projectile ions, giving a scaling of q_{eq} with v_p . Thereby, electron capture by the projectile ion is the dominant process if the current charge state is above q_{eq} , and electron loss by collision is the dominant process if the current charge state is below q_{eq} . The distance over which q_{eq} is achieved depends on the ion energy, ranging from a few monolayers for ions with thermal to keV energies, to a few nanometres for MeV ions, and up to several microns for GeV ions [24]. The evolution of the non-equilibrium charge state can be studied by a simple model proposed by Bohr and Lindhard [25], where the charge at a distance x is given by :

$$q = q_{eq} + (q_{in} - q_{eq})e^{-x/d} \quad (2.7)$$

q_{in} is the initial charge at $x=0$, and d is the equilibrium distance over which the difference between q and q_{in} has reduced by a factor of $1/e$.

Electron loss is efficient only if v_p is greater than the orbital speeds of the electrons. Under the hydrogenic model, the orbital speed of an electron in the outermost shell with atomic number Z_p is given by $v_B Z_p^{2/3}$, where v_B is the Bohr velocity ($v_B = 2.18 \times 10^6$ m/s). Bohr estimated the effective equilibrium charge of the ions as [25]:

$$q_{eq} \approx Z_p \frac{v_p \frac{Z_p}{2}}{v_B Z_p^3} = Z_p^{\frac{1}{3}} \frac{v_p}{v_B} \quad (2.8)$$

Because q_{eq} cannot be greater than Z , the equation was modified as follows to make sure that $q_{eq} \leq Z$:

$$q_{eq} \approx Z_p \left(1 - \exp\left(-\frac{v_p \frac{Z_p}{2}}{v_B Z_p^3}\right) \right) \quad (2.9)$$

Several semi-empirical formulae were developed to calculate the q_{eq} of the given projectile-target system [26–29]. In 1968, Nikolaev and Dmitriev derived a semi-empirical formula for the mean charge state for $Z_p \leq 20$, at energies 5-200 MeV, mainly for carbon targets [26]. Schiwietz and Grande developed a semi-empirical formula for the mean equilibrium charge state in both gas and solid targets [28]. A multi-parameter least-square fit was applied to about 850 experimental data points for solid targets. The q_{eq} from the fit is:

$$q_{eq} = Z_p \frac{12x + x^4}{0.07x^{-1} + 6 + 0.3x^{0.5} + 10.37x + x^4} \quad (2.10)$$

where

$$x = \left(\frac{v_p}{v_B} \frac{Z_p^{-0.52} Z_t^{-0.019} Z_p^{-0.52} \frac{v_p}{v_B}}{1.68} \right)^{1+1.8/Z_p} \quad (2.11)$$

The absolute mean square deviation of q_{eq} from experimental q_{eq} was reported as 0.54 for the fitted q_{eq} in equation (2.10). The above formula was further improved to a mean square deviation of 0.28 by considering asymptotic dependencies, resonance and shell-structure effects [29]. The improved q_{eq} fitted by an iterative procedure is:

$$q_{eq} = Z_p \frac{8.29x + x^4}{0.06x^{-1} + 4 + 7.4x + x^4} \quad (2.12)$$

where,

$$x = c_1 \left(\frac{v_p}{v_B} \frac{Z_p^{-0.543}}{c_2 1.54} \right)^{1+1.83/Z_p} \quad (2.13)$$

and the two correction terms are given by:

$$c_1 = 1 - 0.26 e^{-\frac{Z_t}{11} e^{-\frac{(Z_t - Z_p)^2}{9}}} \quad (2.14)$$

$$c_2 = 1 + 0.03 \frac{v_p}{v_B} Z_p^{-0.543} \ln(Z_t) \quad (2.15)$$

The correction term c_1 accounts for the resonant (non-dissociative) electron capture, while the correction term c_2 accounts for target-dependent deformation of the charge state at the high velocities.

2.3. Stopping power and range

The stopping power of a target is the amount of energy lost by a projectile ion traversing the target per unit length. The energy lost by the ions via collisions with electrons per unit length traversed is called electronic stopping power (S_e), while the energy lost by the ions via collisions with the target nuclei per unit length traversed is called nuclear stopping power (S_n). The total stopping power (S_t) is the sum of the individual stopping powers.

$$S_t = S_e + S_n = - \left(\frac{dE}{dx} \right)_e - \left(\frac{dE}{dx} \right)_n \quad (2.16)$$

The energy lost by the ions can also be expressed in terms of the stopping cross section ($\varepsilon = S_t/N$, where N is the atomic density of the target), which is defined as the energy lost by ions per atom per unit area, avoiding dependence on the potentially unknown mass density of the material. Stopping and Range of Ions in Matter (SRIM) is a software used to predict stopping power values for a given target-ion combination by parameterising approximately 28,100 experimental data on stopping power [30]. In 1905, Bragg and Kleeman [31] gave a simple approximation for calculating stopping power in compounds, known as ‘‘Bragg’s rule’’. According to Bragg’s rule, the stopping

cross-section of the compound (ε_c), with atomic fractions w_i , such $\sum_i w_i = 1$, is the weighted sum of the stopping cross-sections of the constituent elements (ε_i):

$$\varepsilon_c = \sum_i w_i \varepsilon_i = \sum_i - \frac{w_i}{N_i} \left(\frac{dE}{dx} \right)_i \quad (2.17)$$

where N_i is the atomic density of a pure target of element i . This model neglects all chemical interactions between the elements. For compounds such as oxides and hydrocarbons, stopping power values can deviate up to 20% [32]. SRIM uses Bragg's rule to calculate the stopping power for the compounds. But SRIM also includes what is referred to as 'Compound Correction' for many commonly known compounds based on the 'Core and Bond' approximation [30]. In the Core and Bond approach, the stopping contributions from binding electrons (bond) and inner-shell electrons (core) are treated separately. The stopping contribution from the core would follow Bragg's rule for the atoms in a compound, and the stopping contribution from the bond depends on the chemical nature of the compound. The final stopping power of the compound is the sum of these two contributions.

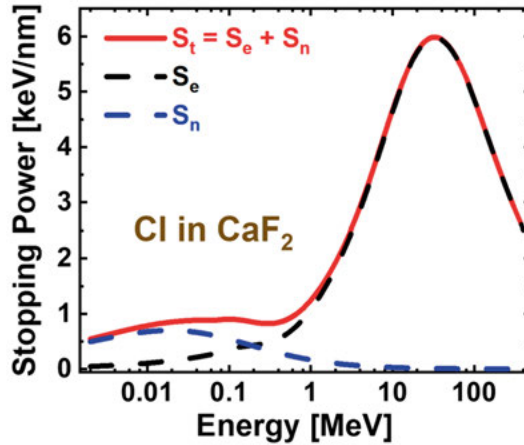


Figure 2.2 Plot of stopping powers for chlorine (Cl) ions penetrating through calcium fluoride (CaF_2) calculated using SRIM-2013 [30]. There is no compound correction for stopping power for CaF_2 available in SRIM-2013.

Figure 2.2 shows the plot of stopping powers for a chlorine (Cl) ion on a calcium fluoride (CaF_2) target, calculated using SRIM-2013. S_n is dominant at low velocities and approaches zero at higher velocities because the cross section for elastic collisions between the ion and the target nuclei decreases with the ion velocity (as discussed in Section 2.1). The free electron gas (FEG) model, a simple model where the electron system of a target is described as a free electron gas, has been used to predict S_e with high accuracy [33]. Lindhard and Scharff used the FEG model to show that S_e increases proportionally with ion velocity for low-velocity ions [34]. For $v_p \gg v_B$, as the ion velocity

increases, the cross section for electron scattering decreases, resulting in a reduced probability for electron scattering and thereby a decrease in S_e . The overlapping of these models leads to a maximum in S_e , referred to as the Bragg peak [31]. Similarly, for S_n , the energy transfer to nuclei is lower for low-energy ions, while the cross section of interaction decreases for higher energies, resulting in a maximum at an intermediate energy. The maximum for S_n is observed at an energy approximately three orders of magnitude lower than the energy for maximum S_e , which is similar to the mass ratio of a nucleon and an electron. This difference in the maxima of the two peaks is due to the dependence of the cross-section of interaction on the masses of the projectile and target.

SRIM calculates stopping powers at q_{eq} . However, for ions with $q \neq q_{eq}$, the stopping power of a target depends on the given charge, q , and is related to equilibrium stopping power as follows [24]:

$$\left(\frac{dE}{dx}\right)_q = \left(\frac{dE}{dx}\right)_{eq} \left(\frac{q}{q_{eq}}\right)^k \quad (2.18)$$

where $k=2$, considering the Rutherford scattering cross section. Using the expression for q in equation (2.7) with $k=2$, equation (2.18) becomes:

$$\left(\frac{dE}{dx}\right)_q = \left(1 + 2\left(\frac{q_{in}}{q_{eq}} - 1\right)e^{-x/d} + \left(\frac{q_{in}}{q_{eq}} - 1\right)^2 e^{-2x/d}\right) \left(\frac{dE}{dx}\right)_{eq} \quad (2.19)$$

Equation (2.19) gives an expression, based on a simple theoretical framework, for the evolution of stopping power in the target as the ion charge evolves towards the q_{eq} (as given in equation (2.7)).

In addition to SRIM, two other software are used for calculating S_e : Convolution approximation for swift Particles (CasP) [35] and Electronic Stopping Power Neural Network (ESPNN) [36]. CasP is based on ab initio calculations and uses a set of approximations to calculate S_e , referred to as the perturbative convolution approximation (PCA), the unitary convolution approximation (UCA) or the induced density approximation (IDA). ESPNN uses machine learning algorithms on the International Atomic Energy Agency (IAEA) stopping power database to predict electronic stopping power for any ion-target combination. The IAEA data is first cleansed using the density-based spatial clustering of applications with noise (DBSCAN) algorithm, an unsupervised machine learning method, to select the most reliable values. 95% of this cleansed data is used as a training set for a deep neural network, and the remaining 5% is used as a test set. While SRIM and ESPNN give stopping power only at the equilibrium charge $(dE/dx)_{eq}$, CasP can provide stopping power at any given charge. CasP uses the formulae in equations (2.12) to (2.15) to calculate the q_{eq} for any given projectile-target combination and thus, calculate the S_e at a given charge.

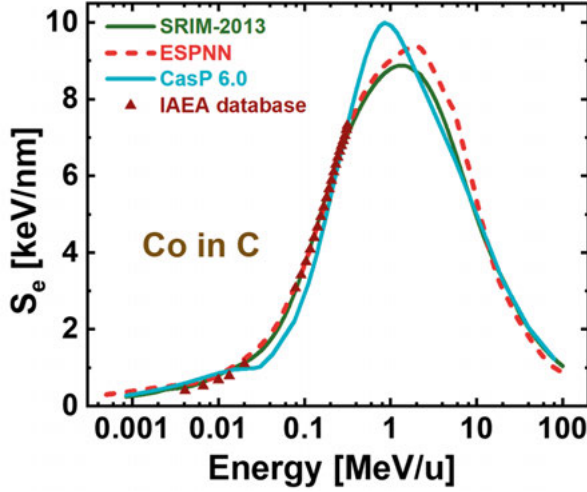


Figure 2.3 S_e at equilibrium charge for a Co projectile on a C target calculated using three software, *viz.* SRIM-2013, CasP 6.0 and ESPNN. Experimental data for stopping power from the IAEA database are also plotted.

Figure 2.3 compares the S_e calculated at equilibrium charge for a Co projectile in a C target using three software, *viz.* SRIM-2013, CasP 6.0 and ESPNN. Experimental data from the IAEA database is also plotted for comparison [37]. CasP numerical calculations were performed using UCA for energies greater than 0.1 MeV/u, and TCS for lower energies and a screening function for the charge-state scan. Stopping power values from all three software are similar at ion energies greater than 10 MeV/u. Predictions from SRIM and ESPNN are also comparable to experimental data for ion energies less than 1 MeV/u. Both SRIM and ESPNN depend on the quantity and quality of available experimental data, and slight differences in S_e values (observed in Figure 2.3) could be due to different datasets and fitting techniques used. CasP, on the other hand, uses numerical calculations based on our understanding of ion-solid interactions and gives comparatively worse values for S_e in the energy regime where our approximations for the theoretical models fail. Currently, SRIM is the widely used software with 85% experimental data within 10% of the calculated stopping power value. However, with recent developments in machine learning-based techniques, ESPNN might become a better method for predicting stopping power for the given ion-target combinations.

A projectile ion continues to slow down in a target by losing energy until its kinetic energy becomes comparable to the thermal energy of the target, where it is stuck in thermal equilibrium, *i.e.*, implanted in the target. The mean total path length of (\overline{R}_t) an ion with incident energy E can be calculated as:

$$\overline{R}_t = \int_E^0 \frac{dE'}{(dE'/dx)_t} \quad (2.20)$$

Due to the stochastic nature of energy deposition and possible deflection of ions from their straight path by scattering from a target nucleus, the individual ions follow different paths in the target, giving rise to a distribution of ion ranges with a mean projected range (R_p). The second moment of the ion range distribution gives the straggling. Longitudinal straggling is the deviation in R_p , parallel to the direction of the incident ion, while lateral straggling is the deviation in the position of the implanted ion, perpendicular to the direction of the incident ion. These values can be predicted using the Transport of Ions in Matter (TRIM) program, which is part of the SRIM software. TRIM uses a Monte Carlo-based code to simulate ion trajectories, using the binary collision approximation and straight-line free flight, with stopping power taken from SRIM tables. Figure 2.4 shows the total ion path (R_t), R_p and straggling for 10 MeV ^{59}Co ions in a 7.5 μm -thick polyimide foil. The deviation from the original path of the ion is higher towards the end of the ion path because, as the ion energy decreases, the cross section for nuclear scattering increases, thus increasing the probability for large-angle nuclear scattering.

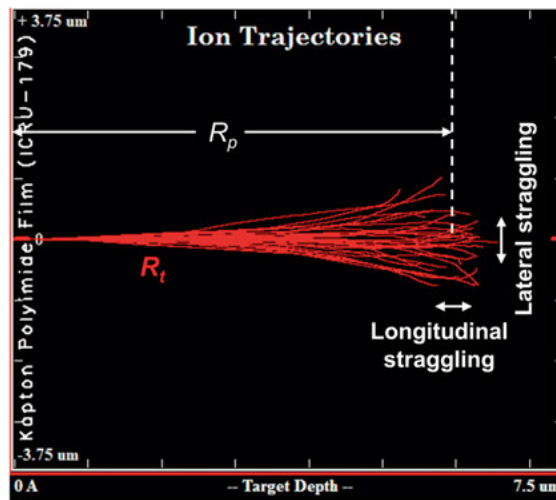


Figure 2.4 Path of 10 MeV ^{59}Co ions in a 7.5 μm thick polyimide foil, simulated using SRIM-2013. The projected range (R_p) of this ion-target combination is 6 μm with longitudinal straggling of 0.3 μm and lateral straggling of 0.4 μm .

3. Ion beam materials modification

At the nanoscale, reduced dimensionality and increased surface-to-volume ratio can give rise to unique physical, optical, electrical and magnetic properties. These properties can also be tuned by changing the size and morphology of the nanoscale features. For example, nonmagnetic bulk materials like gold become magnetic at the nanoscale [38], the melting point of metallic nanomaterials is lower than the corresponding bulk materials and also becomes particle size dependent [39], carbon nanotubes can be made either semiconductors or conductors depending on their nanostructure [40] and peak position of localised surface plasmon resonance (LSPR) of gold nanoparticles can be shifted from near-infrared to the ultraviolet region by changing the size of the nanoparticles [41].

Ion beam-based methods offer reliable, highly reproducible and efficient ways not only for producing nanostructures but also for tailoring the properties, such as structural, electronic, and optical, of nanomaterials. The nanoscale modifications depend on the properties of the ions (e.g., energy, mass, charge), target material (e.g., composition, density, crystallinity), and irradiation conditions (e.g., temperature, irradiation angle, ion fluence). Depending on the choice of ions and the final application of the nanomaterials, this method can be very cost-effective. Present-day commercially available ion implanters can deliver highly stable ion beams of energies ranging from 100 eV to a few MeV with currents ranging from a few μA to a few tens of mA [42]. Henceforth, ion beam-based methods provide versatile and cost-effective approaches for developing high-quality nanomaterials on a large scale.

3.1. Nanostructure engineering

Irradiation of solid targets with ions of energies ranging from eV to GeV has been extensively investigated. Two classes of ions, *viz.*, slow highly charged ions (HCI) [43–46] and swift heavy ions (SHI) [47–49], are widely studied for nanoscale surface modification with applications in, for example, magnetic storage, nanoelectronics, catalysis and nanosensors [50–52]. Slow HCI are characterised by high potential energy due to a relatively large number of vacant electron states and low velocities with kinetic energies on the order of a few tens to hundreds of keV [53]. The potential energy is given by the sum of

the binding energies of all the missing electrons, e.g., potential energies for Xe^{30+} and I^{25+} ions are 15.4 and 8.1 keV, respectively. For SHI, the velocity is higher than v_B , and transfer of energy to matter is dominated by electronic stopping. The kinetic energy of SHI is commonly on the order of tens of MeV to GeV. Although the damage mechanisms of HCI and SHI irradiation are different, they can produce similar surface structures in the same material. For example, irradiation of LiF surface with Xe ions at a given kinetic energy of 100 keV leads to the formation of pits for $q = (15-18)$, calderas for $q = (22-30)$ and hillocks for $q = (33-36)$; showing that for a given kinetic energy surface, structures can be tuned by the potential energy of HCI [54]. For irradiation with swift Xe ions of energy 1.4 MeV/u, hillocks are reported on a LiF surface [55].

A notable example of ion-induced nanostructures in which crystallinity of the target material plays an important role is surface nanoscale patterning. Some crystalline materials with low ionicity, e.g., Si and quartz, get amorphised under ion irradiation. Irradiation with ions of a few keV energy leads to the formation of ripples and nanodots on the surfaces of some of these materials, e.g., Si, Ge, InP and SiC [8,56,57]. These nanopatterns can be tuned by changing the irradiation angle. Irradiation of nonamorphizable insulators, e.g., ionic fluoride materials (e.g., LiF, KBr, CaF_2 , BaF_2) and some oxides (e.g., UO_2 , SnO_2) results in different surface nanostructures, such as pits, craters, calderas or nanohillocks [49–51,53,58–60]. Irradiation of KBr with HCI forms a pit structure on the surface, and the formation of these structures depends on both the kinetic and potential energy of the projectile ion [49]. Apart from surface structures, phase transformation is also observed in nonamorphizable insulators. Y_2O_3 transforms from a cubic to a monoclinic structure, while pure ZrO_2 undergoes a monoclinic-to-tetragonal transformation under ion irradiation.

High-energy ions (such as SHI and MeV ions) that penetrate deeper into the material can modify surface and bulk properties. Ion tracks formed in various materials, such as SiO_2 , SiN, graphene and polymer films, can be selectively etched to form nanopores. The number of pores per unit area is related to the ion fluence, and pore size and shape are related to ion properties and etching conditions. In addition to their applications as solid-state sensors, these nanopores embedded in solid material can also serve as templates for growing other nanomaterials, such as nanowires and nanotubes. Furthermore, ion beam irradiation can be used to shape or align the nanomaterials. For example, irradiation of Si, Ge, ZnO and TiO_2 nanowires by ions of a few keV energy leads to the bending of these nanowires from 20° to 60° with respect to their original direction [61,62], and irradiation of nanoparticles such as Au, embedded in an insulating matrix, by SHI leads to the reshaping of the embedded nanoparticles [63].

3.2. Modification of material properties

Ion-induced structural modification can result in changes in local as well as macroscopic material properties. Controlled and reproducible modifications with ion irradiation and implantation have established these methods as powerful tools for tuning material properties, e.g., electrical, optical, magnetic, chemical and mechanical characteristics.

Ion beams are widely used to tailor electrical and optical properties, enhancing the performance of functional devices for applications in fields such as data storage, sensing, communication and energy storage. Ion implantation has been reported to increase electrical conductivity in materials such as polymers, metal oxide films, single crystals, semiconductors and nanowires [64–66] and modify electronic band structures in, for example, metal-organic frameworks [67]. Irradiation with MeV energy He ions improves the energy storage density and energy release efficiencies in ferroelectric thin films [68]. In the case of PbTiO_2 ferroelectric thin films, MeV energy He ions enhance resistivity and reduce the leakage current by 5 orders of magnitude [69]. The switching properties of memristors, such as retention, electroforming processes and resistance ratio, can be modified by ions [70–72]. Implanting TiO_2 -based memristors with Co ions improves the resistance retention and resistance ratio [73]. The resistive switching behaviour and synaptic plasticity of single-crystalline LiNbO_3 thin films are reportedly improved by Ar ion irradiation [71]. Optical properties, such as optical energy gap, optical absorption, refractive index and photoluminescence, have also been reported to be tuned by ion irradiation. Co-doping of rare-earth ions such as Ce with Ag enables tuning of photoluminescence properties in glass matrices for optical telecommunications and fibre lasers [74]. In wide-bandgap semiconductors, such as V_2O_5 [75] and indium zinc magnesium (IZMO) oxide [76], the optical band gap is modified by ion implantation.

Magnetic properties of materials can also be modified by introducing different ions or defects. Ar ion irradiation of magnetic tunnel junction (MTJ) stacks modifies magnetic anisotropy, saturation magnetisation, tunnel magnetoresistance and exchange bias, and can be modulated by ion fluence [77]. Implantation with Ar ions in $\text{Co}_{20}\text{Fe}_{60}\text{B}_{20}/\text{SmCo}_5$ bilayers results in almost a tenfold increase in coercivity [78]. Irradiation of Pt/Co/Pt tri-layers with He ions decreases the perpendicular magnetic anisotropy and coercivity as a function of ion fluence and temperature, followed by a ferromagnetic-paramagnetic transition [79]. Ions are used for magnetic micro- and nano-patterning in thin films, where magnetic properties such as anisotropy, saturation magnetisation, coercivity and Curie temperature can be modified locally, and have been investigated over the last few decades for applications in, e.g., spintronics, data storage and magnetic metamaterials [80–82].

In addition to influencing electrical, optical and magnetic properties, ion beam-based methods have also been reported to improve mechanical

properties. For example, an increase in hardness, stability and wear resistance of high-energy alloys and polymers by introducing light ions such as H and He ions [83,84], and an increase in elastic modulus of silica-based thin film with MeV energy Cu ion irradiation [85].

3.3. Theoretical models

Different theoretical models like the Coulomb explosion (CE) model [86], bond weakening (BW) model [87,88], exciton self-trapping (STX) model [89], Ionization-Diffusion-Explosion-Amorphization (IDEA) model [90] and thermal spike (TS) model [91–96] have been developed to describe the formation of ion tracks in different materials for SHI irradiation. The CE model assumes that ion-electron collisions lead to a cylindrical region of highly ionised matter along the ion path. Repulsive Coulomb forces act before restoration of neutrality (time scale of less than 10^{-13} s) and are sufficient to break lattice-bonding forces. The BW model is based on the idea that crystal structure depends on electronic structure and electronic excitations affect interatomic forces, leading to material modification. The STX model assumes that the presence of self-trapped excitons in the material (e.g., LiF, SiO₂) reduces the critical energy required to form ion tracks because of the strong localisation of electronic energy along ion tracks in such materials. In both IDEA and TS models, it is assumed that energy deposition in the lattice, leading to material modification, can be described by a transient thermal process in the electronic and lattice subsystems. The formation of ion tracks is still not fully understood, and various models are actively discussed.

Among all these models, the TS model is the most widely studied theoretical model for ion track formation. The heat diffusion in the electronic (e) and lattice (a) subsystems is mathematically described by two time-dependent coupled differential equations in cylindrical symmetry [92]:

$$C_e(T_e) \frac{\partial T_e}{\partial t} = \frac{1}{r} \frac{\partial}{\partial r} \left[r K_e(T_e) \frac{\partial T_e}{\partial r} \right] - g(T_e - T_a) + A(r[v], t) \quad (3.1)$$

$$C_a(T_a) \frac{\partial T_a}{\partial t} = \frac{1}{r} \frac{\partial}{\partial r} \left[r K_a(T_a) \frac{\partial T_a}{\partial r} \right] + g(T_e - T_a) + B(r[v], t) \quad (3.2)$$

where $C_{e,a}$, $T_{e,a}$ and $K_{e,a}$ are the specific heats, temperatures and thermal conductivities of the electronic (e) and lattice (a) subsystems, respectively, at a given time (t) and distance from the axis (r). $A(r[v], t)$ and $B(r[v], t)$ are the energy densities deposited per unit time in the electronic and lattice subsystems, respectively, for specific ion velocity (v). The electron-phonon coupling strength (g) is the only free parameter in these equations.

The energy transferred to electrons is diffused within the electronic subsystem and then transferred to the lattice system via electron-phonon coupling.

Different approaches are used to solve equations (3.1) and (3.2) for describing track formation in the solids using the TS model. The analytical thermal spike model (a-TS) [96,97], developed by Szenes, ignores the process of energy transfer from electrons to atoms and provides an analytical solution to the heat diffusion equations. In this analysis, an increase in temperature due to ion irradiation is approximated by a Gaussian distribution. The TS model, used to get a complete numerical solution of the diffusion equation, is classified into three categories depending on the energy of the projectile ion:

- 1) inelastic thermal spike (i-TS) model
- 2) elastic thermal spike (e-TS) model
- 3) unified thermal spike (u-TS) model

The i-TS model treats high-energy ions, for which $S_n \sim 0$, and most incoming ions transfer their energy to the electronic subsystem. Thus, $B(r[v], t)$ is neglected in comparison to $A(r[v], t)$ in equations (3.1) and (3.2). Monte Carlo simulations are used to calculate the energy distribution in an electronic system, $A(r[v], t)$ [98]. Based on the Monte Carlo calculations, an analytical expression for $D_0(r)$, the dose deposited at the radial distance (r) from the ion path, was proposed by Zhang et al. [99]. Waligorski et al. [100] added a correction factor, $(1+K(r))$, to $D_0(r)$ to account for the dose at small radial distances (~ 1 nm). Incorporating time-dependence, $A(r[v], t)$ is expressed as [101]:

$$A(r[v], t) = a D_0(r) (1 + K(r)) S_e e^{-\left(\frac{(t-t_0)^2}{2\sigma_t^2}\right)} = \frac{a}{r} \left(1 - \left(\frac{r+r_0}{r_m+r_0}\right)^{\frac{1}{\alpha}} \left(\frac{1}{r+r_0}\right)\right) (1 + K(r)) S_e e^{-\left(\frac{(t-t_0)^2}{2\sigma_t^2}\right)} \quad (3.3)$$

r_0 is the range of electrons with energy equal to the ionisation energy of the target, r_m is the maximum projected range of electrons in the target, α is a constant depending on the ion velocity, and t_0 is the mean flight time of δ electrons. The normalisation constant a ensures that the integral over $A(r[v], t)$ results in the S_e .

$$\int_{t=0}^{\infty} \int_{r=0}^{\infty} A(r[v], t) 2\pi r dr dt = S_e \quad (3.4)$$

The excited electrons, then, relax via electron-electron and electron-atom collisions and are dependent on the electron-phonon coupling strength (g). This model has been used to quantitatively describe track formation and predict track radii in the electronic regime in various materials, including metals, semiconductors and insulators.

The e-TS model treats low-energy ions, for which $S_e \sim 0$, and most incoming ions transfer their energy directly to the lattice via elastic collisions. Thus, $A(r[v], t)$ is neglected in comparison to $B(r[v], t)$ in equations (3.1) and (3.2). The expression for $B(r[v], t)$ is given by [102,103]:

$$B(r[v], t) = \frac{b_n}{r} S_n e^{-\frac{t}{\tau}} e^{-\frac{r}{r_1}} \quad (3.5)$$

where τ is the deposition time, r_1 is the cylindrical radius in which nuclear energy is deposited, and b_n is the normalisation constant ensuring integral over $B(r[v], t)$ results in the S_n .

$$\int_{t=0}^{\infty} \int_{r=0}^{\infty} B(r[v], t) 2\pi r dr dt = S_n \quad (3.6)$$

For medium-energy ions, where neither S_e nor S_n is negligible and both elastic collisions and electronic excitation (inelastic collisions) should be considered, the u-TS model is used. It was developed by Toulemonde et al.[104] to study the effect of Au ion irradiation on vitreous SiO₂ in the energy regime of 0.3-15 MeV. The heat diffusion equations (3.1) and (3.2) are solved with both $A(r[v], t)$ and $B(r[v], t)$ terms included.

4. Sample preparation

Two material systems investigated, *viz.*, CaF₂ single crystals (Paper I) and Kapton polyimide foils (Papers II and III), were commercially obtained from Alineason and Dupont, respectively. The multi-layered thin films (Papers IV-VI) were prepared using magnetron sputtering on Si <100> wafers. The ion beam-induced nanostructure formation and material modification were performed using a 5 MV pelletron accelerator and a 350 kV implanter at Tandem Laboratory, Uppsala University [105].

4.1. Ion irradiation and implantation

All the irradiation experiments with ion energies greater than 1 MeV were performed using a 5 MV pelletron accelerator at the Tandem Laboratory, Uppsala University [105]. The positive ions with energies from slightly less than 1 to approximately 50 MeV can be delivered using this accelerator. The facility has four ion sources: one duoplasmatron gas ion source without charge-exchange channels for p, d and ¹⁵N ions; one duoplasmatron gas ion source with charge-exchange channels for He ions; two cesium sputter ion sources for ions of elements from Li to Au. Depending on the energy, ions with charge states from 1+ to 12+ (depending on the ion) can typically be delivered in standard operation. Higher charge states for heavier elements can be obtained using an additional stripping foil.

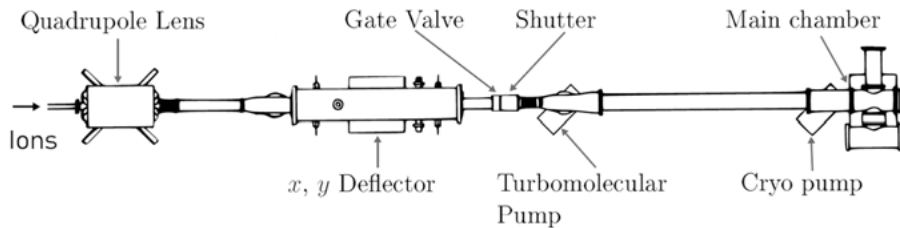


Figure 4.1 The outline for the ion irradiation beamline (T5) at Tandem Laboratory, Uppsala University, reproduced from [106] based on the original design presented in [107].

A dedicated beamline is used for MeV ion irradiation [107], which was upgraded in 2023. In the older setup, samples were mounted on 10 cm × 10 cm sample holder frames and inserted into a magazine that fits up to 20 such

frames. The magazine was placed in the load-lock chamber, and each sample holder frame was transferred to a position in front of the ion beam using a shuttle system. The shuttle system was controlled from a graphical user interface (GUI), developed in-house using LabVIEW. In the upgraded setup, the transfer system was replaced with a vertical moving system, comprising five sample holders with a 4" diameter. A fluorescent surface is used to position the beam spot and determine the scan area. A raster scan system with a deflection voltage of ± 10 kV and frequencies of 64 and 517 Hz in the horizontal and vertical direction, respectively, is used to obtain homogeneous ion fluence over an area up to 10×10 cm². A Faraday cup positioned at the end of the beamline, in front of the sample holder, is used to measure the beam current. The Faraday cup has an area of 1 cm² and can be moved vertically, and thus, can be used to monitor the beam current density during irradiation by over-scanning the beam. A working pressure below 1×10^{-6} mbar can be maintained during irradiation. Further improvements to the upgraded irradiation beamline are ongoing, including irradiation at higher temperatures via a heating sample holder and improved beam-scanning performance.

All the ion implantation experiments were performed using a 350 kV implanter at the Tandem Laboratory, Uppsala University [105]. Both singly and doubly charged ions can be delivered, allowing the ion energies up to 700 keV for doubly charged ions. Lower ion energies of less than 10 keV can also be achieved by either decreasing the extraction potential or using a deceleration unit. High currents of several mA can be achieved at the implanter, allowing implantations at very high doses in a reasonable time (for example, fluxes of the order of 10^{14} ions/(cm² s¹) with an ion beam current of more than 100 μ A).

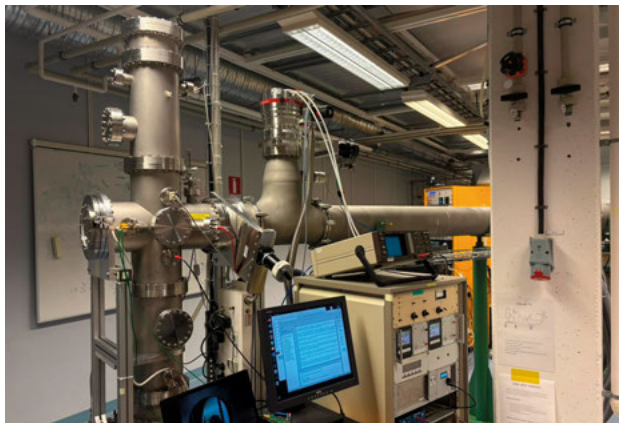


Figure 4.2 The upgraded end station for ion irradiation at the Tandem Laboratory, Uppsala University

4.2. Wet chemical processing

Wet chemical processing is used to remove materials with liquid chemicals, to obtain clean substrates for thin film deposition (Papers IV-VI) and to produce nanoporous foils (Papers II and III).

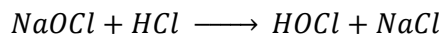
Commercially bought 4" silicon wafers were cleaned using the standard RCA cleaning process [108]. In this process, the wafers are first cleaned with a solution of ammonium hydroxide (NH_4OH), hydrogen peroxide (H_2O_2) and de-ionised water (DIW) to remove particles and organic contaminants; followed by a solution of hydrochloric acid (HCl), H_2O_2 and DIW to remove metallic impurities and inorganic residues. H_2O_2 breaks very rapidly at elevated temperatures; thus, H_2O_2 is poured just before using the solution for cleaning. Both steps are performed at temperatures of 60-65°C for 10 minutes, followed by rinsing in DIW at room temperature. Finally, to remove the native oxide layer, the wafers were dipped in 2% hydrofluoric acid (HF) solution. The silicon wafer was then thermally oxidised to grow a layer of SiO_2 , followed by dicing it into $(10 \times 10) \text{ mm}^2$. Ultrasonic cleaning [109] of the diced substrates, using acetone, isopropyl alcohol (IPA) and DIW, was performed to remove any residual contaminants before depositing the films using magnetron sputtering.

Ion-irradiated materials can be chemically etched to preferentially remove ion tracks relative to the undamaged area, forming nanopores. The rate of removal of unirradiated or undamaged material (called bulk etch rate, V_B) should be lower than the rate of removal of ion-damaged material within the ion track (called track etch rate, V_T) to etch out nanopores in the irradiated samples. The shape of the etched-out nanopore depends on the ratio of V_B and V_T , with half opening angle, α , given by [110]:

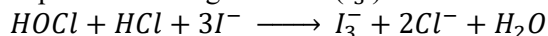
$$\alpha = \arcsin\left(\frac{V_B}{V_T}\right) \quad (4.1)$$

The ion tracks formed in polyimide foils (Papers II and III) were etched using sodium hypochlorite (NaOCl) solution. V_B depends on factors such as the temperature (T) and pH of the solution [110,111]. It increases with both temperature and pH, resulting in a larger opening angle. To produce mostly cylindrical nanopores, etching conditions of $\text{pH} = 10$ and $T = 50^\circ\text{C}$ were maintained for all experiments in this thesis and appended papers. The pH of the as-purchased NaOCl solution was 12 ± 0.2 and adjusted to 10 using 10% (v/v) hydrochloric acid (HCl). The chlorine concentration of the solution was determined indirectly by a standard iodine/thiosulfate titration, including four steps [112]:

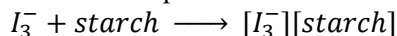
- 1) Sodium hypochlorite reacts with hydrochloric acid to form hypochlorous acid:



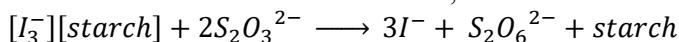
- 2) Hypochlorous acid reacts with iodide, in an acidic environment, to give a dark red complex containing triiodide (I_3^-):



- 3) The dark red complex containing triiodide combines with starch to give a dark blue starch-triiodide complex:



- 4) The dark blue starch-triiodide complex is titrated with sodium thiosulphate to form a colourless solution of iodide, dithionate and starch:



Based on the stoichiometry of the above reactions, two moles of thiosulfate ions react with one mole of NaOCl. The number of moles of thiosulfate is calculated from the known molarity and volume of the thiosulfate solution used in the titration. Using the number of moles and the molar density, the mass of NaOCl is calculated. Finally, the *w/v* chlorine concentration is determined from the ratio of the mass of NaOCl (calculated from the titration experiment) to the volume of the original bleach solution.

4.3. Magnetron Sputtering

Magnetron sputtering is a physical deposition technique widely used in thin film coating [113,114]. A vacuum chamber is filled with inert gas such as Argon (Ar). When a high voltage is applied across the chamber, the Ar atoms ionise, generating plasma. Under the influence of the applied electric field, the positively charged Ar ions accelerate towards the target element at the cathode, ejecting or sputtering atoms from the target material due to momentum transfer. The presence of a magnetic field due to magnetrons traps electrons near the cathode, creating a confined, denser plasma near the cathode and thus increasing sputtering efficiency. The sputtered atoms, emitted with high kinetic energy, travel across the vacuum chamber and get deposited on the substrate. The properties of the deposited film depend on various parameters, such as base pressure of the chamber, working gas pressure, gas flow rates, discharge power, power supply mode, target material, substrate temperature and target-substrate distance [115–117].

A magnetron sputtering system, custom-designed by PreVac, at the Tandem Laboratory was used to prepare multi-layer thin film structures (Papers IV-VI) [118]. The system is equipped with four MS2 63C1 magnetron sources compatible with targets with 2" (50.8 mm) diameter and 1-6 mm thickness. All four magnetrons can be operated simultaneously for co-deposition, with two magnetrons operating in direct current (DC) mode and the other two in radio frequency (RF) mode. DC mode is used for conducting or semiconducting targets (e.g., Ti, Pd), whereas RF mode can be used for both conductive

and insulating targets but gives a lower deposition rate than DC mode for otherwise similar deposition conditions [117]. The sample stage has a 2" diameter and is positioned about 15 cm from the sputtering targets during deposition. The sample stage is rotated continuously to ensure uniform film deposition. A quartz crystal microbalance (QCM) is installed inside the sputtering chamber to estimate the deposition rate. A base pressure of 5×10^{-8} mbar or lower is maintained in the sputtering chamber. The system has three gas inlets with mass flow controllers (MFCs): one is used for the working gas (Ar), and the other two can be used for reactive sputtering with one or a mixture of reactive gases, such as oxygen and nitrogen.

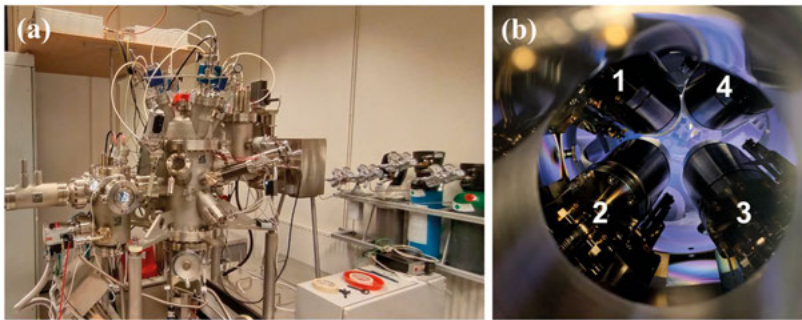


Figure 4.3 (a) Magnetron sputter system at the Tandem Laboratory, Uppsala University; (b) Top view of the four magnetrons (marked by numbers 1-4)

Figure 4.4 shows the schematics and electrical measurement configuration of the multi-layered structure, deposited using magnetron sputtering, used to investigate ion-induced tuning of the memristor properties. An adhesion layer of Ti was deposited on SiO₂/Si substrate, followed by a bottom electrode (BE) of Pd, an amorphous TiO₂ layer and finally a top electrode (TE) of Pd. The films were deposited in DC mode with Ar as the working gas. The TiO₂ layer was deposited by reactive sputtering.

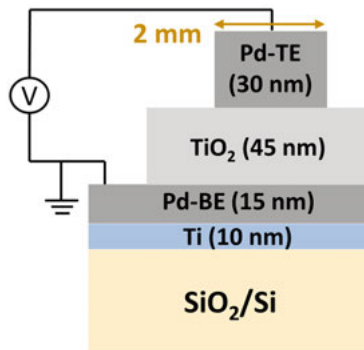


Figure 4.4 Schematic illustration and electrical measurement configuration of multi-layered memristor structure (based on Figure 1 in Paper V)

5. Characterisation and analysis

Ion beam material modification for the different systems of interest was characterised and analysed using a wide range of methods. Atomic force microscopy (AFM) and scanning electron microscopy (SEM) were used to characterise the surface topography, and transmission electron microscopy (TEM) was used to image and characterise along the sample cross-section. Several different ion beam analysis (IBA) methods were employed to determine material composition and elemental depth profiling. Different X-ray-based methods, such as X-ray diffraction (XRD) and X-ray photoelectron spectroscopy (XPS), were used to analyse material structure and composition. The electrical characterisation was performed by applying a voltage across the sample using two probes. All the characterisation methods used in this thesis and the appended papers are discussed in this chapter.

5.1. Ion Beam Analysis (IBA)

Ion beam analysis (IBA) utilises the fundamental interactions between ions and target atoms to investigate material properties, including elemental composition of thin films, depth profiling, impurity analysis, and isotopic profiling. Depending on the properties of the incoming projectile ions and target atoms, various interactions lead to different measurable signals. Some common IBA techniques include Rutherford Backscattering Spectrometry (RBS), Elastic Backscattering Spectrometry (EBS), Elastic Recoil Detection Analysis (ERDA), Particle-induced X-ray Emission (PIXE) and Nuclear Reaction Analysis (NRA) [105,119–121]. These techniques are mostly non-destructive, reliable, highly sensitive and quantitative. Figure 5.1 shows the end stations used for IBA measurements with MeV ions at the Tandem Laboratory.

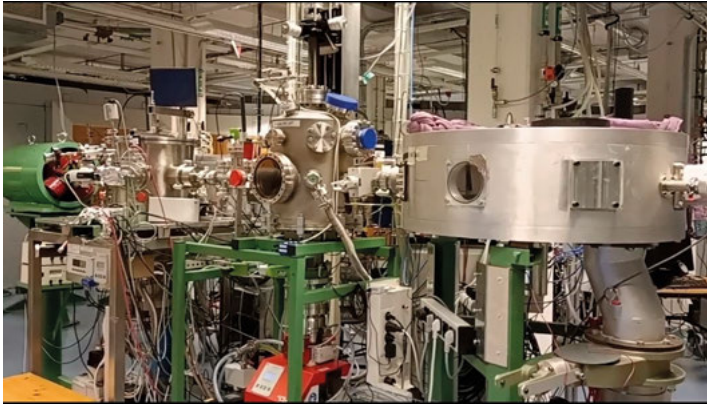


Figure 5.1 End stations for IBA measurements at the Tandem Laboratory, Uppsala University. This beamline is used to perform RBS, EBS, ERDA and PIXE measurements on samples using ions with MeV energies.

5.1.1. Rutherford Backscattering Spectrometry (RBS)

In RBS and EBS, a beam of light ions, such as ^1H and ^4He , is focused on the sample, and backscattered ions are commonly detected at angles between 160° and slightly less than 180° with respect to the incoming beam. The elastic collision between the incoming ion and the target nucleus is explained in Section 2.1, where the energy of the backscattered ion (E'_p) can be calculated from equation (2.3) as $E'_p = K_p E_p$. The energy spectra of these backscattered ions contain information on the sample composition and thickness. EBS offers an advantage over RBS in analysing lighter elements (for example, ^{16}O and ^{12}C) because of the enhanced scattering cross sections, in particular, light elements of interest at specific energies and backscattering angles resulting from nuclear resonance effects [120,122]. The difference between RBS and EBS lies in the relevant scattering cross-section [122]. The Rutherford cross section for the projectile (equation 2.5) is calculated under the assumptions that interactions between the ion and target are only Coulombic and the projectile and scattering partner are point particles (i.e., point masses and charges). These assumptions are valid only for the ions within a certain energy range (a few MeV). For low-energy projectiles charge screening by electron shells cannot be neglected. Conversely, for high-energy projectiles, nuclear forces become significant, and the interaction is no longer purely Coulombic. Consequently, in these cases, the scattering cross sections cannot be accurately described by Rutherford cross sections.

SIMNRA 7.03, a software developed at Max-Planck-Institut für Plasmaphysik in Garching, Germany, is used to retrieve information about the sample composition and thickness from RBS/EBS spectra [32]. SIMNRA can be used to calculate the energy spectra for the given ion-target combination and experimental conditions. The ion-target cross-sections for the relevant energy range

are available from the Ion Beam Analysis Nuclear Data Library (IBANDL) [123], a database of experimental cross-sections for both Rutherford and non-Rutherford backscattering. The latest version of the software also includes the cross-section calculator SigmaCalc [124], which uses nuclear model-based interpolation and extrapolation from existing experimental data to estimate cross-sections for non-Rutherford scattering and nuclear reactions.

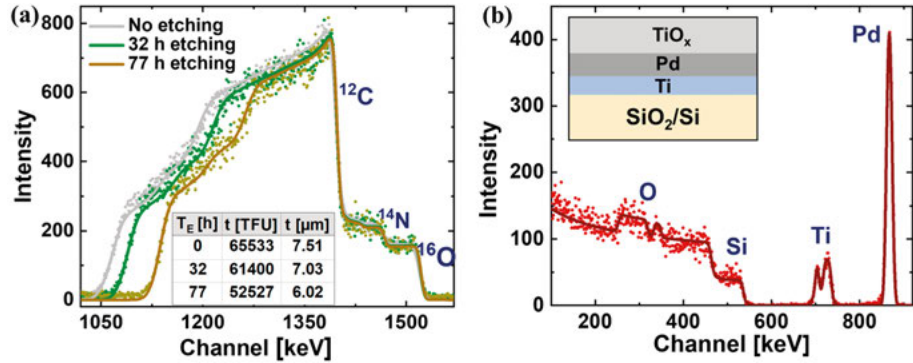


Figure 5.2 (a) EBS spectra, obtained using a 2 MeV proton beam, for the PI foils symmetrically etched for 0, 32 and 77 hours on both sides in NaOCl solution kept at 50°C and pH = 10. This figure is based on Figure 8 of Paper II. (b) RBS spectrum, obtained using a 2 MeV $^4\text{He}^{1+}$ beam, for the multi-layered films (shown in the inset) investigated for resistive switching properties. [In both subfigures, dots represent experimental spectra, and solid lines represent spectra simulated using SIMNRA.]

RBS was used to analyse the structure of multi-layered films prepared using magnetron sputtering (Papers IV-VI) and calculate the areal density of the TiO_2 layer (Paper IV). Proton EBS was used to measure the thickness and, subsequently, the bulk etch rate (v_B) of polyimide foils (Paper II) in NaOCl solution. Figure 5.2(a) shows the EBS spectra for the pristine polyimide foil and foils etched symmetrically on both sides for 32 and 77 hours. In SIMNRA, the thickness is calculated in terms of thin film units ($1 \text{ TFU} = 1 \times 10^{15} \text{ atoms/cm}^2$), which can be converted into length units using the formula given below:

$$t[\text{cm}] = \frac{t[\text{TFU}] * 10^{15} * M[\frac{\text{g}}{\text{mol}}]}{\rho[\frac{\text{g}}{\text{cm}^3}] * N_A[\frac{\text{atoms}}{\text{mol}}]} \quad (5.1)$$

where ρ is the mass density, N_A is Avogadro's number, and M is the average molar mass. In this case, the $\rho = 1.42 \text{ g/cm}^3$ and $M = 9.8 \text{ g/mol}$ are used to calculate the thickness. Similarly, using Equation (5.1) in Paper IV, the ρ of TiO_2 in the multi-layered structure was calculated. Using $M \sim (79.89/3) \text{ g/mol}$, the thickness of the TiO_2 layer from TEM images and $t[\text{TFU}]$ from the RBS spectra, the mass density of as-prepared and ion-irradiated TiO_2 films was calculated and compared. Figure 5(b) shows the RBS spectrum for the multi-layered films (structure in the inset), deposited using magnetron sputtering.

5.1.2. Elastic Recoil Detection Analysis (ERDA)

For ERDA measurements, a beam of heavy ions such as ^{127}I and ^{197}Au is focused on the sample, and the recoil ions ejected from the target are analysed with detectors placed at angles less than 90° with respect to the incoming beam. Material characterisation can be performed using the kinematic relation in equation (2.4), the recoil cross section in equation (2.6), and the stopping powers of the projectile and the recoil ion. ERDA is a widely used IBA method for depth profiling and analysing lighter elements such as carbon and oxygen. A recoil angle (φ) of 0° gives the maximum value of the recoil energy (equation (2.4)), whereas φ approaching 90° gives the maximum value of the recoil cross section (equation (2.6)). A $\varphi = 45^\circ$ provides a good trade-off between these two values. Thus, for the ERDA measurements in this thesis and appended papers, both the incident and detection angles were kept at 67.5° with respect to the sample surface normal, resulting in a detector angle of 45° with respect to the forward direction of the incoming projectile.

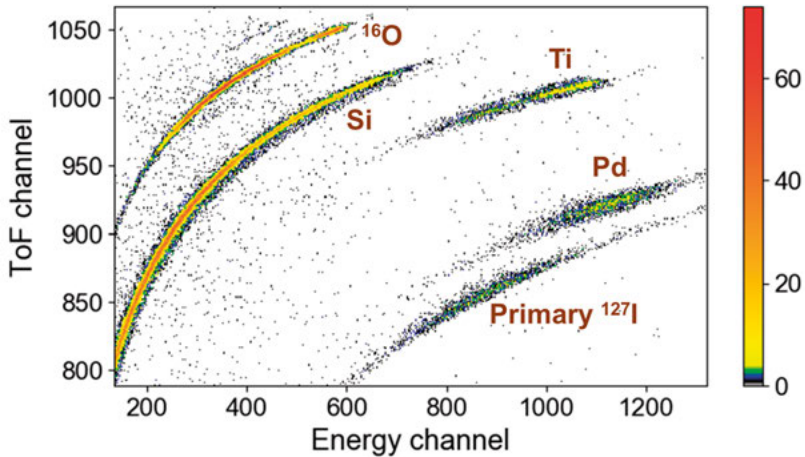


Figure 5.3 ToF-ERDA spectrum for the multi-layered films shown in Figure 1.2 (corresponding RBS spectrum in Figure 5.2(b)). In addition to recoil ions, primary ^{127}I ions scattered towards the detector are also plotted. This figure is based on Figure S1(a) in Paper V.

At the Tandem Laboratory, two time-of-flight ERDA (ToF-ERDA) systems are used for material characterisation. In the ToF-ERDA setup, two time detectors are placed over a fixed distance to measure ToF, followed by an energy detector that measures the energy (E) of the recoil ion. The coincidence measurement of ToF and E is used to plot the E-ToF histogram, where each ion with a different mass is observed as a separate banana-shaped region. Figure 5.3 shows the ToF-ERDA spectrum obtained with a 36 MeV I^{8+} beam and the setup discussed above for the multi-layered structures grown for investigating memristor properties. The ToF-ERDA spectra were analysed using Potku

[125] for elemental depth profiling. Potku is an open-source analysis software developed by the University of Jyväskylä, Finland.

5.1.3. Nuclear Reaction Analysis (NRA)

NRA uses short-range nuclear reactions under resonance conditions between ion and target nuclei for elemental composition, depth profiling and isotopic tracing. One of the beamlines at the 5 MeV pelletron accelerator is designed for hydrogen profiling using the resonant nuclear reaction $^{15}\text{N}(\text{H},\alpha\gamma)^{12}\text{C}$ with a narrow resonance in its cross section at an energy of (6.385 ± 0.005) MeV [126]. A beamline is designed for the 350 keV implanter for depth profiling of ^{11}B and ^{18}O using the resonant nuclear reactions $^{11}\text{B}(\text{p},\alpha)^8\text{Be}$ and $^{18}\text{O}(\text{p},\alpha)^{15}\text{N}$, respectively [127,128]. ^{18}O tracing is a powerful technique that uses stable isotope ^{18}O to track processes and atomic movements. ^{18}O isotope tracing was performed using NRA to investigate the switching mechanism in oxygen-implanted memristors by studying changes in oxygen profile as a function of switching cycles (Paper VI). $^{18}\text{O}(\text{p},\alpha)^{15}\text{N}$ has a narrow resonance in its cross-section at an energy of (151.0 ± 0.1) keV [129].

A proton beam with energies ranging from 149 to 175 keV was employed to depth profile the ^{18}O concentration in the memristor (Paper VI). The depth, d , at which the protons of incident energy, E , reach the resonant energy, E_{Res} , can be calculated as:

$$d[nm] = \frac{(E - E_{Res}) [keV]}{S_t \left[\frac{keV}{nm} \right]} \cos(\theta_{tilt}) \quad (5.2)$$

where S_t is the total stopping power of the proton beam in the sample, and θ_{tilt} is the tilt angle. The concentration of ^{18}O in the given sample (N_S) can be calculated by comparing the number of α particles detected over a period of time or for a given integrated charge delivered to the sample with that of a reference sample with a known concentration of ^{18}O , as given below:

$$N_S \left[\frac{atoms}{cm^3} \right] = \frac{n_S}{n_{Ref}} \frac{(S_t)_S}{(S_t)_{Ref}} N_{Ref} \quad (5.3)$$

In the above equation, $n_{Ref,S}$ is the number of α particles detected over a period of time in the reference and the given sample, and was normalised by integrated charge delivered to the sample to account for differences in the number of detected α particles due to changes in beam current with time; $(S_t)_{Ref,S}$ is the total stopping power of the proton beam in the reference and given sample; and $N_{Ref,S}$ is the atomic concentration of ^{18}O in the reference and given sample.

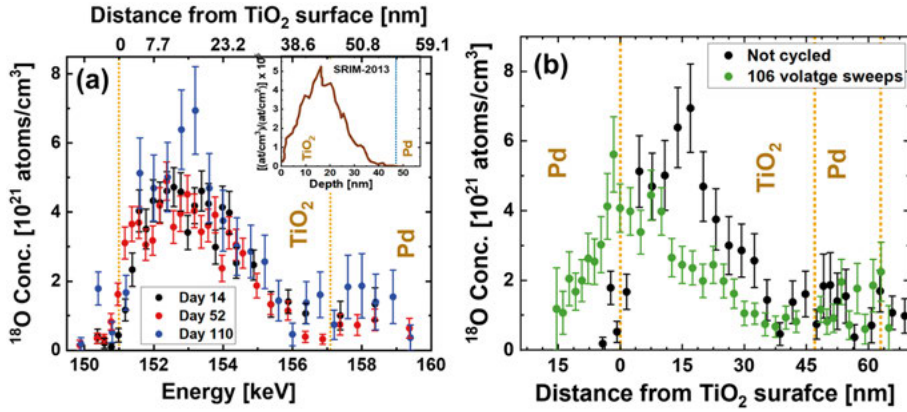


Figure 5.4 (a) ^{18}O concentration profile for TiO_2 film implanted with 8 keV ^{18}O ions at a fluence of 2.93×10^{16} ions/cm 2 , measured 14, 52 and 110 days after implantation. Inset: The expected concentration profile for 8 keV ^{18}O in TiO_2 , simulated using SRIM-2013; (b) Comparison of the ^{18}O concentration profile of a sample after 106 voltage sweeps (with alternating polarity) with a non-cycled sample. The x-axis plots the distance in reference to the top Pd- TiO_2 interface. Subfigures (a) and (b) are extracted from Figures 2 and 3(a) in Paper VI.

Figure 5.4(a) shows the ^{18}O concentration profile in TiO_2 (the complete multi-layered memristor structure in Figure 4.4) implanted with 8 keV ^{18}O ions at a fluence of 2.93×10^{16} ions/cm 2 . The implantation was performed before the top Pd layer was deposited. The concentration profiles were measured 14, 52 and 110 days after implantation. The sample was kept under vacuum between the measurements. The experimental concentration profile matches well with the expected concentration profile simulated using SRIM-2013 (inset of Figure 5.4(a)), and no significant change over time is observed. However, when voltage sweeps (0 V \rightarrow ± 8 V \rightarrow 0 V) with alternating polarity are applied, a shift in ^{18}O concentration is observed. Figure 5.4(b) compares the ^{18}O concentration profile of the sample after 106 voltage sweeps with a non-cycled sample.

5.2. Microscopy

Microscopy is a fundamental analytical tool, widely used to visualise and characterise materials at micro- and nano-scales. Commonly used microscopes use light or photons (e.g., optical microscopes), electrons (e.g., electron microscopes) or a physical probe (e.g., scanning probe microscopes) to characterise the materials. In this thesis and appended papers, the surface topography and nanostructures were investigated using AFM (for single-crystal CaF_2) and SEM (for polyimide foil), and the cross-sections of all the samples were analysed using TEM.

5.2.1. Scanning Electron Microscopy (SEM)

SEM is a widely used method for collecting information about the shape, crystallography, composition, and topography of samples at the microscopic scale. A focused beam of energetic electrons (energies ranging from 1 to 30 keV) is produced using emission from an electron source and accelerated to an anode [130]. It further passes through a series of apertures and electromagnetic lenses that shape, focus, and raster-scan the electron beam onto the sample. The incoming electron affects a certain volume of the sample called the interaction volume. The spatial resolution in SEM is of the order of a few nanometres and depends on the interaction volume. A higher electron beam energy produces a smaller spot size (which gives better resolution) but increases the interaction volume (which reduces spatial resolution). Figure 5.5 shows different signals emitted from the interaction volume in the sample, which are detected to analyse the samples. The most commonly used outgoing signals are backscattered electrons (BSE), secondary electrons (SE) and characteristic X-rays.

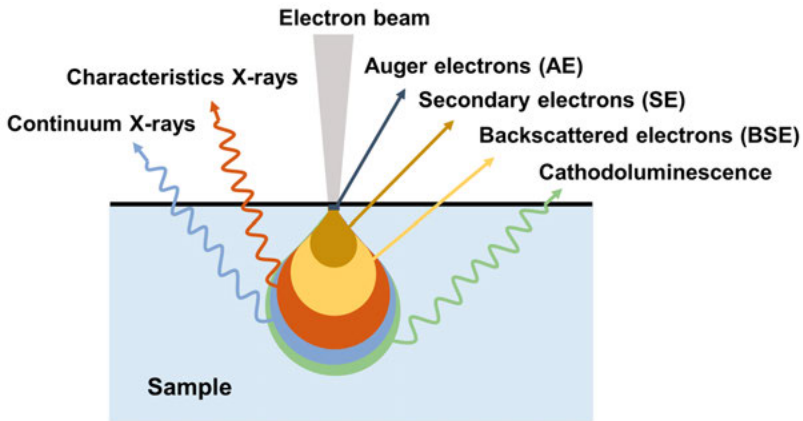


Figure 5.5 Electron-matter interaction volume with various signals generated

BSE are the primary electrons that are elastically scattered and deflected back from the sample with little or no energy loss. BSE may come from a great depth of the sample and contain elemental information. A semiconductor (most commonly: silicon) detector, placed directly above the sample, is used to detect BSE intensity and make a map of atomic number (Z) variation in the scanned sample. The distinction between elements in the BSE detector depends on the difference in cross-section for electron scattering. The heavier elements in the sample are stronger scatterers of electrons than lighter elements and thus appear brighter in BSE images. SE are emitted as a result of interactions between primary electrons and atoms near the sample surface. They have energies less than 50 eV and contain information about the sample surface. Figure 5.6 shows the SEM image of polyimide foil, irradiated with 42

MeV $^{197}\text{Au}^{9+}$ ions, (a) before and (b) after etching with NaOCl solution at 50°C for four hours. The composition of the sample surface can be analysed by studying the characteristic X-rays produced by electron-matter interaction. First, incoming electrons excite the target atom by removing inner shell electrons. Then, electrons from the outer shell move into the vacancies in the inner shell, deexciting the atom and emitting X-ray photons. This process forms the basis of Energy Dispersive X-ray Spectroscopy (EDS).

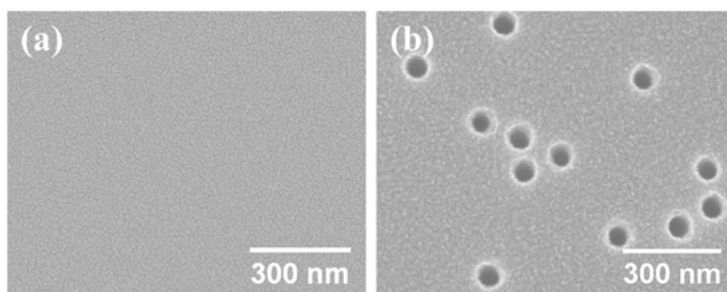


Figure 5.6 SEM image of polyimide foil, irradiated with 42 MeV Au ions, (a) before and (b) after etching with NaOCl solution at 50°C for four hours (both SEM images are based on Figure 2 in Paper II).

For a non-conducting sample, if the number of incident electrons is higher than the number of electrons escaping the sample, the sample surface becomes negatively charged. This build-up of negative charge on the surface is known as the charging effect and can result in image distortion. The amount of charging depends on the energy and number of electrons, and thus, can be reduced by either decreasing the extraction voltage or the beam current. Alternatively, a non-conducting sample (polyimide foils in our case) is coated with a thin layer of conductive material, such as Au/Pd, to avoid charging of the sample surface. The SEM images displayed in this thesis and appended papers were acquired using a Zeiss LEO 1550 and a Zeiss LEO 1530 SEM at an acceleration voltage of 10 kV.

5.2.2. Transmission Electron Microscopy (TEM)

TEM is another microscopy technique that uses an electron beam focused with a set of apertures and electromagnetic lenses. However, unlike SEM, where signals from the interaction volume are analysed, primary electrons transmitted through the thin samples are analysed in TEM. Commonly, electron beams of energies 30-300 keV are used in TEM. It is possible to achieve sub-Ångström spatial resolution with TEM [131]. In addition to real-space imaging, selected area electron diffraction (SAED) can be performed within TEM to obtain crystallographic information about the selected region of a sample.

Scanning TEM (STEM) is an operating mode of TEM in which a focused electron beam is raster scanned across the sample for high-resolution imaging.

An ultrathin lamella of 100 nm or less is extracted from the samples for TEM imaging. Different methods, such as cross-sectional preparation, focused ion beam (FIB), ultramicrotomy, resin embedding and polishing, are used to extract lamella depending on the sample to be analysed [132,133]. FIB was used to extract a lamella from the samples studied in this thesis and the appended papers. A protective platinum (Pt) layer was deposited over the entire region of interest to protect the underlying layers from damage during milling. Initially, a thin Pt layer was deposited using electron-beam-assisted deposition, followed by Ga ion-beam-assisted deposition. A high-current ion beam is used to mill the area around the cross-section to be lifted out. The lamella is then lifted out using a micromanipulator. Further polishing of the cross-section is done with a low-current ion beam. The lamella is then positioned on the TEM grid to be analysed. Figure 5.7(a) shows the lamella prepared from polyimide foil (Paper II) and fixed to the TEM grid.

In TEM, a viewing screen coated with a fluorescent material such as ZnS is placed below the sample, to directly observe, focus and align the image in real time before recording it. The image is typically recorded using a complementary metal-oxide semiconductor (CMOS) based camera. A FEI Titan Themis 200 system at an acceleration voltage of 200 kV was used for TEM imaging of the samples in this work and the appended papers. Figure 5.7(b) shows a TEM image of the multi-layered thin films, deposited using magnetron sputtering, to investigate memristor properties.

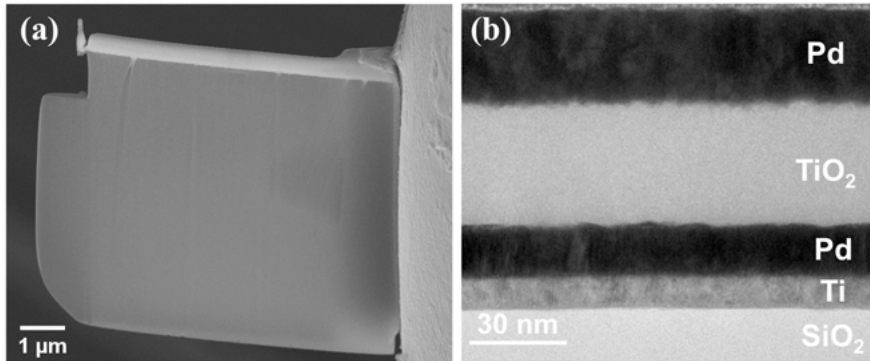


Figure 5.7 (a) SEM image of a lamella lifted from a polyimide foil and connected to the TEM grid. (b) TEM image of the multi-layered thin films, distinguished by the contrast.

5.2.3. Atomic Force Microscopy (AFM)

AFM is a non-destructive surface imaging technique with atomic-level resolution. It is a high-resolution scanning probe microscopy (SPM), widely used

for imaging surface properties of a wide range of materials, irrespective of their electrical conductivity [134]. A sharp probe tip, supported by a flexible cantilever, is raster-scanned over a sample surface, and the interaction force between the tip and the sample is recorded [135]. The force can either be attractive or repulsive, depending on the tip-sample distance, causing deflection or bending of the cantilever. Therefore, AFM can operate in three imaging modes: contact mode, tapping/intermittent mode and non-contact mode. Figure 5.8(a) shows the interatomic force diagram for the operating region for three modes. In contact mode, the tip is constantly kept in ‘contact’ with the sample (at a distance of a few Å), resulting in a repulsive force between the tip and surface. In contrast, the probe tip oscillates at or near the resonance frequency in both tapping mode and non-contact modes. In non-contact mode, the tip is kept a few nanometres above the surface so that there is always an attractive interatomic force between the tip and sample; however, in tapping mode, the tip periodically vibrates between regions of attractive and repulsive interatomic forces. Contact mode is the most common choice for imaging hard surfaces. However, in some cases, such as surfaces that can damage the probe tip or are soft, the tapping or no-contact mode is preferred. The AFM images presented in this thesis and appended papers were acquired in contact mode using a PSIA XE150 AFM. Figure 5.8(b) shows the AFM image of a single crystal of CaF₂ along the (111) plane.

A schematic of AFM is shown in Figure 5.8(c). The key components of an AFM include a probe tip and a scanner to position the sample with respect to the tip. A sharp probe tip, usually made of Si or Si₃N₄, is fixed to a cantilever. A laser beam is fixed on the upper side of the cantilever and is reflected onto a photodiode. When the scanner moves the probe closer to the surface, the tip interacts with the sample, deflecting the cantilever. This results in displacement of the reflected laser on the position-sensitive photodiode, producing a detector signal (Z_{in}), which is sent to a feedback control system and compared to a pre-set setpoint signal (Z_{set}). The difference between Z_{in} and Z_{set} is called the error signal (Z_{err}). The error signal is then sent to a proportional-integral-derivative (PID) controller [135]. P, I and D values are optimised, and the output signal (Z_{out}) is sent to the scanner to adjust the tip-sample distance to minimise Z_{err} . The probe is raster-scanned to create an array of data points (x, y, Z_{out}) containing information about the surface topography, and is decoded by computer software into an image.

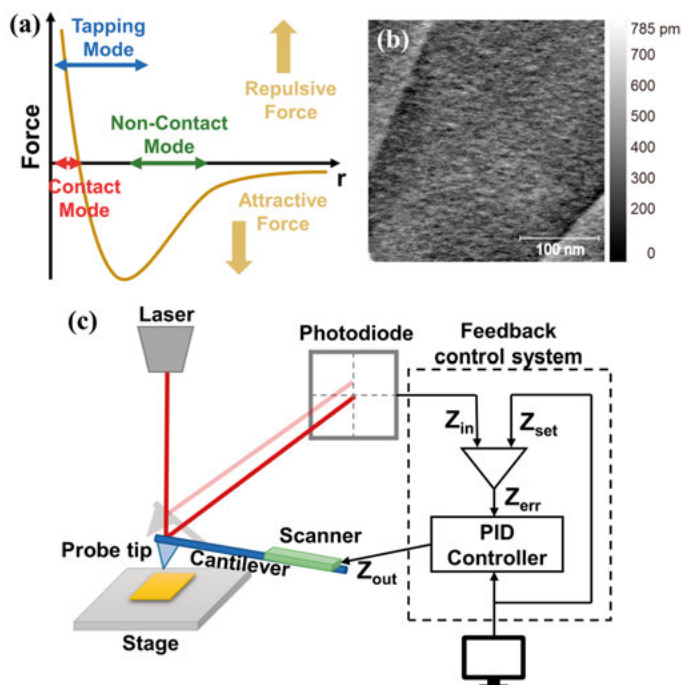


Figure 5.8 (a) Interatomic force between probe tip and surface as a function of distance between tip and surface (r), along with regions for different imaging modes of AFM; (b) AFM image of a single crystal of CaF_2 along the (111) plane (extracted from Fig. 3.3 in Paper I); (c) Schematic of AFM

5.3. X-ray characterisation

X-rays are widely used to analyse the bulk structural and chemical properties of materials. Based on the interaction of X-rays with matter, these methods provide information on both the atomic arrangement and chemistry of the materials. In the present work, two X-ray characterisation techniques were used, *viz.*, X-ray total scattering with pair distribution analysis to study the effect of ion irradiation on short-range ordering (Paper IV) and X-ray photoelectron spectroscopy (XPS) to study the impact of ion implantation on elemental oxidation states (Paper V).

5.3.1. Total X-ray scattering

The total scattering method is a technique to investigate both long-range (Bragg scattering) and short-range (diffuse scattering) ordering in materials. The Fourier transform of the total scattering data gives the weighted probability distribution function, which measures the probability of finding pairs of atoms separated by a given distance, known as the pair distribution function

(PDF), $g(r)$ [136–138]. PDF analysis is used to study local structures in materials with local modifications (e.g., defects) within long-range order, limited long-range order (e.g., nanocrystals and gels) and no long-range order (e.g., amorphous solids and liquids).

The maximum scattering wavevector (Q_{max}) is the upper limit of integration used in the Fourier transform of total scattering data into PDF, and thereby determines the resolution in real space [139]. This makes Q_{max} the most critical factor to obtain a high-quality $g(r)$. For X-rays of wavelength λ , the scattering wavevector is given by:

$$Q = \frac{4\pi \sin(\theta)}{\lambda} \quad (5.4)$$

where 2θ is the scattering angle. Thus, high-energy or short-wavelength X-ray sources are used to obtain good real-space resolution. But this presents challenges for analysing samples with dimensions in the nanometre range, such as thin films, as the penetration depth increases with energy. In recent years, thin film PDF analysis has been explored using various approaches [137,140,141]. One of these methods is to extract a PDF from grazing-incidence (GI) total scattering data, which was used in Paper IV to investigate the impact of MeV ion irradiation on the local structure of amorphous TiO₂ films.

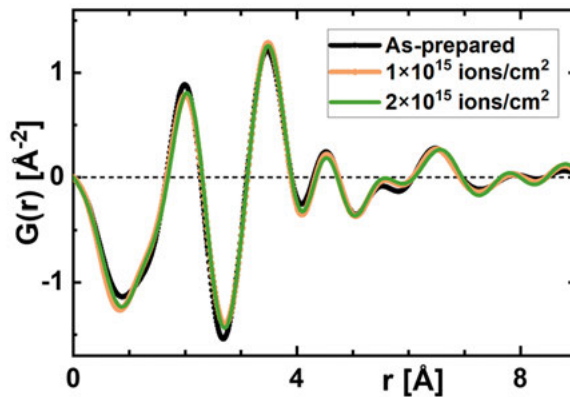


Figure 5.9 Reduced PDF, $G(r)$, for as-prepared amorphous TiO₂ films and after irradiation with 10 MeV Cu³⁺ ions at fluences of 1×10^{15} and 2×10^{15} ions/cm² (based on Figure 2 in Paper IV).

A Malvern Panalytical instrument with a Mo K α source was used for scattering measurements [141]. The films were deposited on a crystalline Si substrate and oriented in such a manner to avoid any Bragg reflection from the substrate. This eliminates the need to collect GI data for the substrate and substrate reduction steps. Figure 5.9 shows the reduced PDFs, $G(r)$, for a 300 nm thick amorphous TiO₂ film before and after irradiation with 10 MeV Cu³⁺ ions at fluences of 1×10^{15} and 2×10^{15} ions/cm². $G(r)$ represents the deviation of local atomic density from the average density (ρ_0), and is given as:

$$G(r) = 4\pi\rho_0[g(r) - 1] \quad (5.5)$$

The first and second peaks in Figure 5.7 correspond to the average interatomic spacing between Ti-O and Ti-Ti bonds. The width of a peak gives the root-mean-square (rms) scattering from the distance between two atoms. The area under the peak at a distance (r) gives the total number of atoms at r from the central atom, and is known as the coordination number. Although the film remains amorphous after irradiation at a fluence of 1×10^{15} ions/cm², modifications in the local structure of the film are observed and can be quantified using PDF analysis. The Ti-O average bond length increased from 1.99 Å to 2.07 Å, and the average coordination number increased from 5.05 to 5.67 (measured from the first peak) with MeV ion irradiation at a fluence of 1×10^{15} ions/cm². No significant changes in the bond length or coordination number were observed when the fluence was further increased to 2×10^{15} ions/cm².

5.3.2. X-ray Photoelectron Spectroscopy (XPS)

XPS is a surface-sensitive technique, based on the photoelectric effect, for quantitative analysis of composition, chemical state and electronic structure of a material [142,143]. When a beam of X-rays with energy (E_{ph}) is focused on a target, electrons are emitted from the target surface if E_{ph} exceeds the target work function (Φ_T). In core-level photoemission, electron binding energy (E_B) also needs to be considered for calculating the kinetic energy of the emitted photoelectrons (KE_T), given by:

$$KE_T = E_{ph} - E_B - \Phi_T \quad (5.6)$$

The KE_T is measured with an analyser, which has a different Fermi level and work function (Φ_A). The sample and analyser are electrically connected, so their Fermi levels align, resulting in an offset in vacuum levels that gives the contact potential (Δ).

$$\Delta = \Phi_T - \Phi_A \quad (5.7)$$

As a result, the kinetic energy measured by the analyser (KE_A) and thus binding energies are independent of Φ_T :

$$KE_A = KE_T + \Delta = E_{ph} - E_B - \Phi_A \quad (5.8)$$

From the XPS spectra (intensity vs E_B), all elements (except hydrogen and helium) can be identified by the position of photoelectron peaks. Small shifts in the peaks can provide information about the chemical state of the elements in the sample. The relative intensities of the peaks can give the relative composition of elements in the part of the sample analysed under XPS, assuming that that part of the sample is homogeneous.

In XPS, low-energy X-rays with energies up to 2 keV, such as Al K α (1487 eV) or Mg K α (1253.6 eV) sources, are used. Information depth can be

estimated from the inelastic mean free path (IMFP) in solids. It depends on the kinetic energy of the electron and the material's composition, and is 1-5 nm in XPS measurements. To probe deeper, X-rays of energies (2-10) keV are used, and the technique is known as Hard X-ray Photoelectron Spectroscopy (HAXPES) [144,145] with an information depth of a few tens of nanometres. HAXPES has emerged as a powerful tool for investigating bulk, subsurface and buried interface properties of materials. The higher photon energy of the hard X-rays allows the excitation of deeper core electrons. On the other hand, the photoionisation cross-section decreases with photon energy, requiring a more intense X-ray source [146].

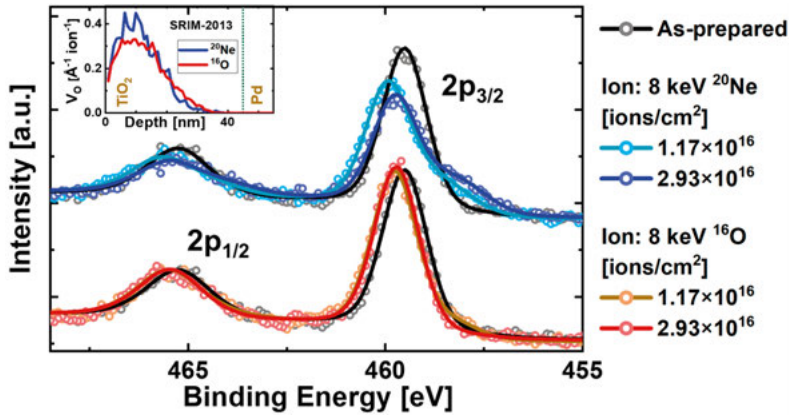


Figure 5.10 HAXPES spectra (hollow circles) and curve fits (solid lines) for as-prepared and ion-implanted amorphous TiO₂ films for Ti 2p core shell. Inset: The expected oxygen vacancy concentration profiles for ²⁰Ne and ¹⁶O ions, simulated using SRIM-2013, for comparison with the HAXPES measurements. This image is extracted from Figure 2(c) in Paper V.

XPS and HAXPES measurements in this thesis and appended papers were performed at the Kai Siegbahn laboratory, Uppsala University, using a Scienta Omicron HAXPES lab equipped with an EW4000 electron analyser. An Al K α (1487 eV) and liquid Ga K α (9250 eV) X-ray source was used for XPS and HAXPES measurement, respectively. Figure 5.10 shows the HAXPES spectra for amorphous TiO₂ film before and after implantation with 8 keV Ne and O ions for Ti 2p core shell. The peaks at 459.5 eV and 465 eV correspond well to Ti 2p_{3/2} and Ti 2p_{1/2} for the Ti⁴⁺ oxidation state. A small shoulder on the Ti 2p_{3/2} peak of the implanted sample indicates the presence of the Ti³⁺ oxidation state, as the E_B of Ti³⁺ is \sim 1.5 eV lower [147]. This change in oxidation state is due to the creation of oxygen vacancies by ion implantation. As simulated using SRIM-2013 [30] and shown in the inset of Figure 5.10, ion implantation would create a reservoir of oxygen vacancies with a maximum at depths of 6-13 nm in the TiO₂ layer. The curve fits were performed using pseudo-voigt functions and a Shirley-type background [148] to calculate the

relative percentage of Ti^{3+} and Ti^{4+} oxidation states in the film. For as-prepared films, 3% Ti^{3+} is calculated, increasing to 28% and 31% with Ne ion implantation at fluences of 1.17×10^{16} and 2.93×10^{16} ions/cm², respectively. However, for O-implanted films, 3-10% Ti^{3+} is calculated, which can be considered similar to that for as-prepared TiO_2 films.

5.4. Electrical characterisation

The electrical properties, e.g., resistance and current-voltage curves of the multi-layered films (Papers IV and VI), were investigated using a Keysight B1500A Semiconductor Device Parameter Analyser. Two tungsten probes were used to apply a voltage to the top electrode (TE) and the bottom electrode (BE), grounding the BE, and measuring across the memristor structure. Figure 5.11(a) shows the stage where the samples for electrical measurements are positioned, and the four available tungsten probes. During all electrical measurements, a maximum allowed current, referred to as compliance current (I_{cc}), was specified to prevent damage to the memristors. When the current (I) reaches or increases above I_{cc} , the instrument limits the voltage across the sample such that $I = I_{cc}$. For the IV characterisation, the voltage was swept from 0 to a few volts with steps of tens of mV. In this thesis and appended papers, one switching cycle refers to two voltage sweeps: one with positive voltage and the other with negative voltage. Resistance is calculated from the slope of the IV curves around 0 V, where Ohm's law is valid. This resistance value is further verified by applying a constant 5 mV voltage and measuring the current across the sample. The retention or stability of the resistance state over time was studied by measuring current across the sample at 5 mV for an extended period.

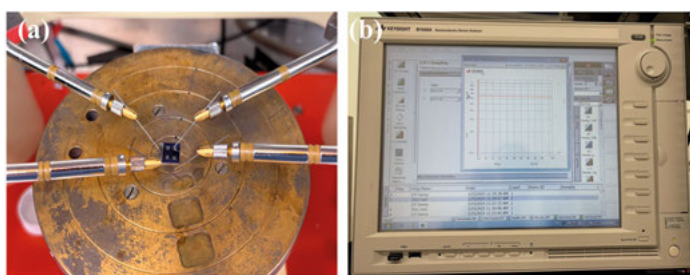


Figure 5.11 (a) Stage for the probe station with the memristor sample. The setup has four tungsten probes, but only two were used at a time, for the measurements; (b) Data collection setup for the Keysight B1500A Semiconductor Device Parameter Analyser.

6. Results and discussion

6.1. Nanostructure engineering using MeV ions

6.1.1. Surface nanostructures

The surfaces of single-crystal CaF_2 irradiated with MeV ions were analysed using AFM in contact mode. The irradiated surfaces exhibit one of the following features:

- I. No nanostructures are observed; the surface is comparable to that of an unirradiated CaF_2 crystal (Figure 5.8(b)), i.e., dominated by flat terraces with steps of height 0.32 nm or an integer multiple of 0.32 nm.
- II. Irregular structures of vertical variations less than 2 nm are observed over the terraces (Figure 6.1(a))
- III. Distinct triangular structures of a few nanometres high are observed as the dominant feature over the terraces (Figure 6.1(b))

The relation between the three categories of surface morphology and ion properties is investigated. When all projectile ions (ranging from ^{35}Cl to ^{197}Au with energies from 2.5 to 48 MeV) are plotted on a map of S_e versus specific energy (E_S), as shown in Figure 6.1(c), the three distinct features described above are identified as three separate regions on the map. No surface nanostructures are observed for projectiles with $E_S < \sim 0.04$ MeV/u (referred to as region I in Figure 6.1(c)). For ions with $E_S > 0.04$ MeV/u, surface nanostructures are observed for the investigated projectile ions (Table 2.1 in Paper I for details of all the investigated projectile ions). At a given E_S , the formation of irregular nanostructures or distinct triangles on the surface depends on the S_e . A higher S_e is required to form triangular nanostructures on the surface. A threshold electronic stopping power (S_{et}) is defined as the S_e below which no distinct triangular nanostructures are observed on the CaF_2 surface. The S_{et} divides regions II (irregular structures) and III (distinct triangular structures) in Figure 6.1(c) and is observed to increase with E_S .

For SHI irradiation-induced damage in single-crystal CaF_2 , two thresholds are reported in terms of S_e [12]: (a) quenching of a molten phase, accompanied by swelling and surface nanohillock formation, and (b) quenching of a boiling phase leading to visible ion tracks. These observations indicate that distinct

triangular nanostructures observed under MeV ion irradiation may originate from the rapid quenching of a localised molten region created by electronic energy transfer along the ion path. This molten region swells and solidifies at the nanoscale, producing the observed distinct surface nanostructures.

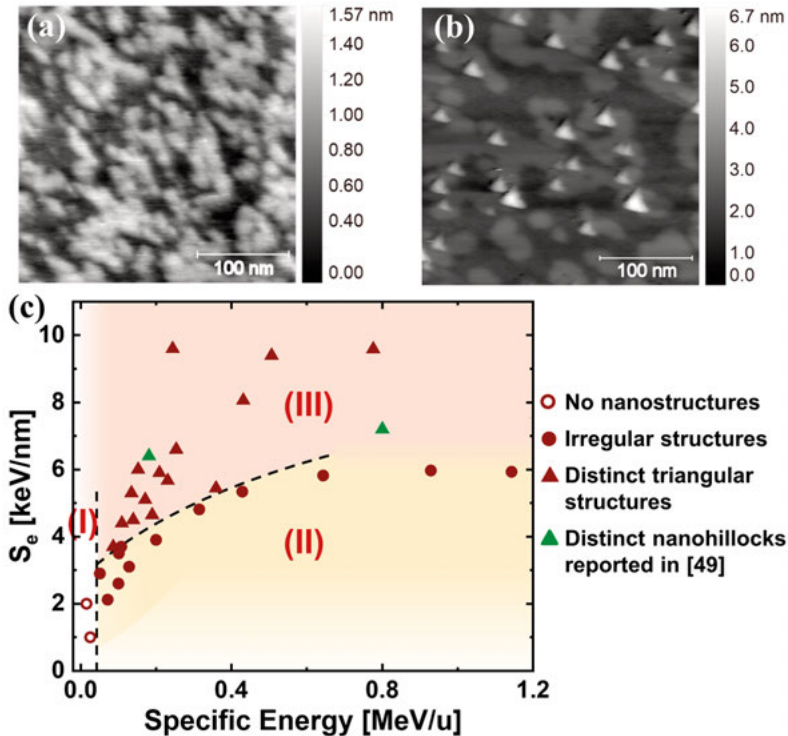


Figure 6.1 AFM images of the CaF_2 surface irradiated with (a) 7 MeV Cl^{3+} and (b) 48 MeV Au^{11+} ; (c) A map of specific energy and S_e for the ions used to irradiate CaF_2 , showing three distinct regions of ion-induced damage. Subfigures (a) and (b) are extracted from Fig. 3.3 in Paper I, and subfigure (c) is based on Fig. 3.2 in Paper I.

6.1.2. Bulk nanostructures

The surface of polyimide (PI) foils irradiated with MeV ions was analysed using SEM. After etching the irradiated PI foils for four hours, the PI surfaces exhibit one of the following features:

- I. No openings are observed, indicating that the projectile ion did not cause enough damage to form etchable ion tracks.
- II. Nanopits with a wide distribution of opening diameter with a standard deviation > 6 nm are observed. The areal density of the surface openings is less than 70% of the incident ion fluence (i.e., less than 70% of all ion impacts result in etchable structures near the PI

surface). Figure 6.2(a) shows an SEM image of nanopits observed after irradiation with 6.5 MeV O^{3+} , and Figure 6.2(c) shows the corresponding opening diameter distribution.

- III. Nanopores with a comparatively narrow distribution of opening diameters with a standard deviation ≤ 6 nm are observed. The areal density of the surface openings is within 30% of the incident ion fluence. Figure 6.2(b) shows an SEM image of nanopores observed after irradiation with 11 MeV Si^{3+} , and Figure 6.2(d) shows the corresponding opening diameter distribution.

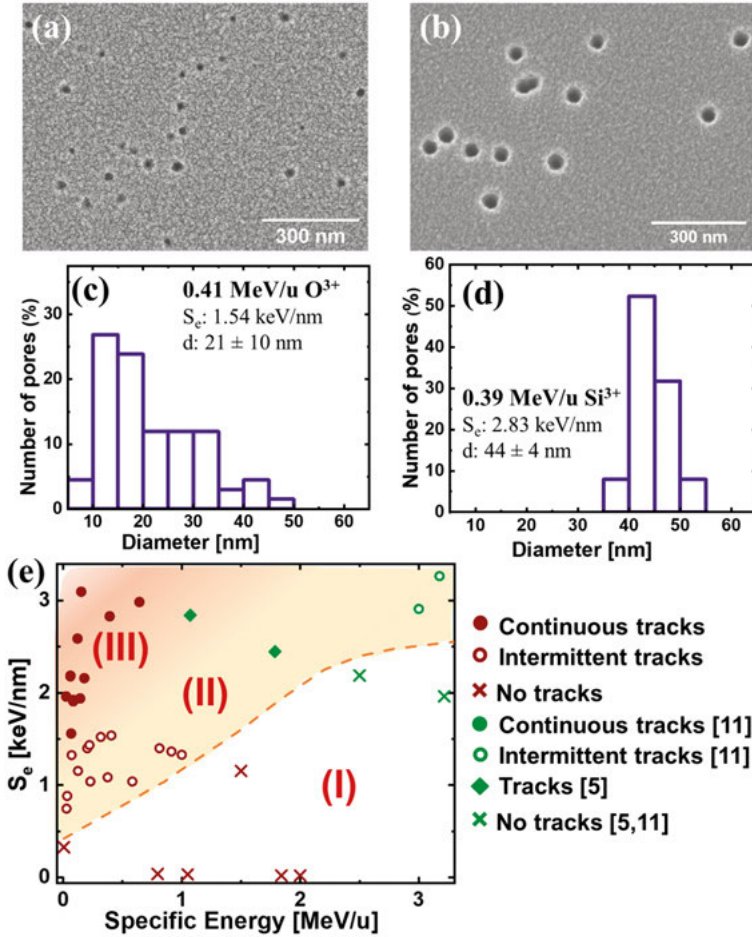


Figure 6.2 (a, b) SEM images of the surfaces of PI foils and (c, d) corresponding opening diameter distribution after irradiating with (a) 6.5 MeV O^{3+} and (b) 11 MeV Si^{3+} and etching in NaOCl solution for four hours at 50°C; (e) A map of specific energy and S_e for the projectile ions, showing three distinct regions of ion-induced modification. Reference [5] does not specify whether the tracks were intermittent or continuous and are represented by solid rhombi. Subfigures (a) and (b) are extracted from Figure 2 in Paper II, and subfigure (e) is based on Figure 4 in Paper II.

The mechanism for chemical etching of ion tracks, proposed in Paper II, relates the variation in opening diameter distribution to the formation of intermittent and continuous tracks in the second and third categories, respectively (as illustrated in Figure 3 of Paper II). The formation of intermittent tracks is attributed to the stochastic nature of damage along the ion path.

To investigate the relationship between the three categories of surface morphology and ion properties, a map of S_e versus E_S , similar to one for surface nanostructures in CaF_2 , is plotted. Figure 6.2(e) shows the map of S_e versus E_S for the projectile ions used to irradiate PI foils. Three distinct regions are identified on the map corresponding to the three categories described above for the surfaces of ion-irradiated PI foils. At a given E_S , with an increase in S_e , the irradiated and etched PI foil transitions from no nanopores to nanopits with a wide range of opening diameters (region II in Figure 6.2(e)) and to nanopores with a narrow range of opening diameters (region III in Figure 6.2(e)). Thus, in the case of PI foils, two distinct thresholds in terms of S_e are defined: S_{et} above which nanopits are observed, and S_{et}^c above which nanopores with a narrow range of opening diameters are observed. Both thresholds are dependent on the E_S , as observed in Figure 6.2(e).

6.1.3. Dependence of nanostructures on properties of MeV ions

As observed above, MeV ions can produce both surface and bulk nanostructures, similar to those by slow HCI (surface nanostructures) and SHI (both surface and bulk nanostructures). Similar to SHI, the threshold for producing both surface and bulk nanostructures with MeV ions is observed in S_e . However, there are two differences: the threshold S_e for MeV ion irradiation is lower than that for SHI irradiation and has a velocity dependence ($E_S \propto v^2$). In the case of CaF_2 , SHI are reported to produce surface nanohillocks above a S_{et} of 4.8 ± 1.1 keV/nm [49]; whereas for MeV ions, a $S_{et} = 3.6 \pm 0.1$ keV/nm is observed for ions with $E_S = 0.1$ MeV/u. The S_{et} increases to 5.3 ± 0.1 keV/nm as the E_S (and thus ion velocity) increases to 0.36 MeV/u. A similar trend is observed for ion tracks or etched nanopores in PI foils. SHI are reported to have $S_{et} = 1.85$ for intermittent tracks and $S_{et}^c = 5$ keV/nm for continuous tracks [11]; on the other hand, a S_{et} as low as 0.5 ± 0.2 keV/nm for intermittent tracks and a S_{et}^c as low as 1.4 ± 0.1 keV/nm for continuous tracks is observed for MeV ion irradiation. Analogous to surface structures in CaF_2 , the thresholds for ion tracks in the PI foils are observed to be velocity (or specific energy) dependent.

The dependence of the S_e threshold on velocity and a lower threshold for MeV ions can be explained by a phenomenon widely known as the velocity effect [149]. The radius of the electron cascade perpendicular to the ion path is directly proportional to ion velocity. As shown in the schematic in Figure 6.3(a), if we consider two ions with the same mass (m) and S_e but different energies (or velocities), the ion with a higher energy (or velocity) will have a

larger radius of the energy cascade, and energy is spread within a bigger volume. Consequently, the deposited energy density will be lower, resulting in lower damage to the material. Hence, a higher S_e is required to cause the same kind of damage when irradiating with a higher velocity ion.

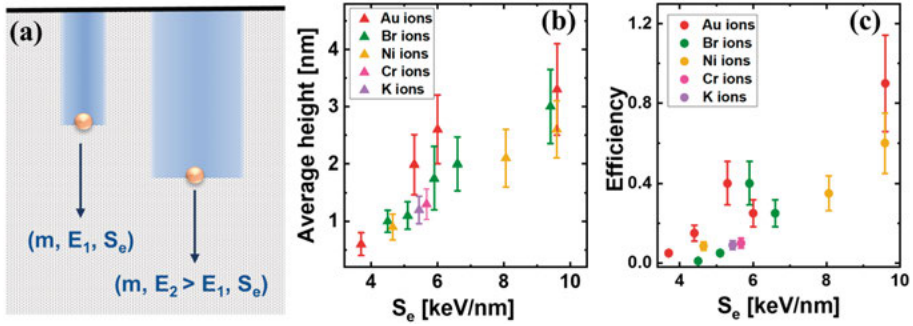


Figure 6.3 (a) Dependence of radius of the ion track (depicted by blue colour) for two ions with the same m and S_e , but different energy (E) or velocity (v); (b) The average height and (c) the mean efficiency of formation of distinct triangular structures on the surface of CaF_2 as a function of S_e . Subfigures (b) and (c) are extracted from Fig. 3.4 in Paper I.

Furthermore, the threshold S_e is not a strict line dividing the different damage regions defined for both material systems. In fact, there is a gradual transition from one damage region to another. Energy deposition is a stochastic process causing local fluctuations in the deposited energy. As S_e or energy deposited in the material increases, more damage is induced, and the probability of fluctuations in S_e surpassing the threshold increases. This results in more well-defined nanostructures as S_e increases without an abrupt transition. For instance, in the case of CaF_2 , S_{et} is defined as the value below which no distinct triangular structure is observed. As the S_e increases above S_{et} , the surface is gradually dominated by distinct triangular structures compared to irregular structures. The height and efficiency of formation of distinct triangular structures (defined as the ratio of the areal density of distinct triangular structures to the ion fluence) of the distinct triangular nanostructures in region III increase with S_e . Figure 6.3 shows (b) the average height and (c) the mean efficiency of these triangular nanostructures as a function of S_e . Similarly, for PI foils, the conditions on the standard deviation of the opening diameter and areal density are defined to obtain numerical thresholds that differentiate these distinct regions. But there is no abrupt transition; the distribution of opening diameter and the efficiency of nano-scale openings on the surface of PI foils change gradually as S_e increases, at a given E_s .

Overall, the MeV ion-induced nanostructures in a given material system can be engineered using two ion properties: the electronic stopping power (which depends on ion type and energy) and the ion velocity (or specific

energy). As the energy density deposited in the materials depends on ion velocity, the threshold S_e in the MeV energy regime is velocity-dependent.

6.1.4. Charge equilibration

In the section above, the MeV ion-induced damage threshold is defined in terms of S_e . As discussed in Section 2.3, S_e depends on ion charge state (q) and for projectile ions with initial charge (q_{in}) different from the equilibrium charge state (q_{eq}), the damage in the near-surface region will vary. To provide insight into how such a modified damage region can be intentionally introduced, and thereby enable the use of charge-state variation as a parameter to control the properties of nanostructures, the impact of charge-state evolution on nanopore formation was studied in Paper III.

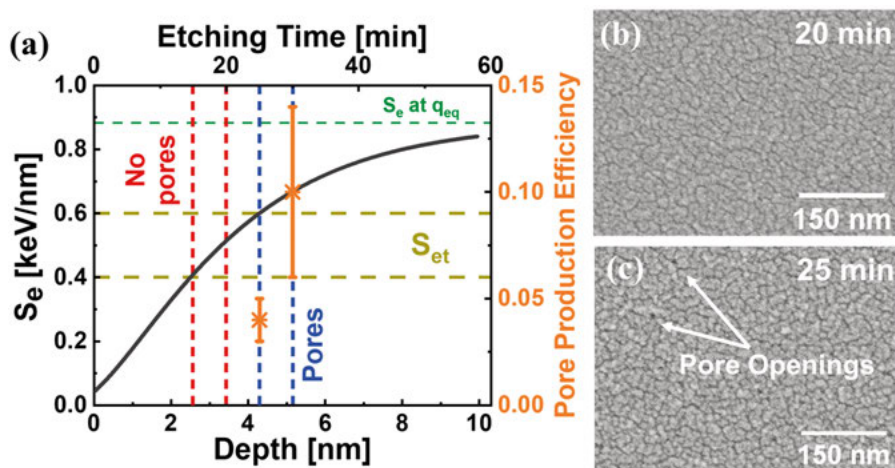


Figure 6.4 (a) Evolution of S_e for 2 MeV Co^{1+} in PI foil. The dashed vertical lines correspond to the etching times after which the PI foils were analysed using SEM: red lines indicate depths (or etching times) where no pore openings were observed, and blue lines indicate depths (or etching times) where pore openings were observed. The orange points present the pore production efficiency on the surface of the foil; SEM images of PI foils irradiated with 2 MeV Co^{1+} ions and etched for (b) 20 and (c) 25 minutes in NaOCl solution at 50°C . Subfigure (a) is extracted from Fig. 2, and subfigures (b) and (c) are extracted from Fig. 1 in Paper III.

One example discussed here is for PI foils irradiated with 2 MeV Co ions with $q_{in} = 1+$. 2 MeV Co ions have $q_{eq} = 4.6+$ in PI foils, and at this energy, the S_{et} for intermittent tracks is 0.5 ± 0.1 keV/nm. Figure 6.4(a) shows the evolution of S_e for 2 MeV Co^{1+} ions based on equation (2.19), and ions are expected to cross the S_{et} at a depth of (2.5 – 4.3) nm. Figure 6.4 shows the SEM images of the PI films irradiated with 2 MeV Co^{1+} ions and etched for (b) 20 and (c) 25 minutes in NaOCl solution at 50°C . No pore openings are observed after 20 minutes of etching, but after etching for 25 minutes, some pore openings begin

to appear. This indicates that etchable ion tracks begin to form at a depth of (3.4 – 4.3) nm for these ions, which is comparable to the theoretically predicted value. The etching times are converted to depth using the bulk etching rate of 10.3 nm/h for PI foils (discussed in Section 5.1.1). The pore production efficiency is only 0.04 ± 0.01 after 25 minutes of etching, but it increases with etching time. When ions with the same energy and mass but different charge states are used, e.g., 17 MeV Co ions, distinct etching times were observed. Nanoscale openings were observed after only 5 minutes of etching for $q_{in} = 6+$, whereas reducing q_{in} to $2+$ required at least 10 minutes of etching before any nanoscale openings were observed.

These results show that q_{in} and charge equilibration processes significantly influence the near-surface nanostructures. As the threshold and radius of ion tracks or ion-induced damage depend on S_e , the q dependence of S_e provides a useful parameter for controlled engineering of nanostructures. Moreover, the simple theoretical methods used here offer a practical framework for analysing and predicting the charge effects.

6.2. Sequential effects of MeV ion and keV electron irradiation

After exploring MeV ion-induced nanostructures on single crystals and polymers, crystallisation of the next material system, i.e., amorphous TiO₂ (a-TiO₂), under MeV ions was investigated. Figure 6.5 shows a bright-field-STEM (BF-STEM) image, with the SAED image in the inset, of (a) the as-prepared TiO₂ film and after irradiation with 10 MeV Cu ions at fluences of (b) 1×10^{15} and (c) 2×10^{15} ions/cm². The film remains amorphous up to a fluence of 1×10^{15} ions/cm², but nanocrystals are observed at a fluence of 2×10^{15} ions/cm². In addition to a change in crystallinity of the film, two changes in the film properties are observed:

- Mass density increases from 3.54 ± 0.15 g/cm³ for the as-prepared film to 3.81 ± 0.16 g/cm³ after irradiation at a fluence of 1×10^{15} ions/cm²; but further increase in fluence do not result in any change in the mass density.
- Local atomic ordering: From reduced PDF analysis (refer to Figure 5.9), the average coordination number for Ti increases from 5.05 for the as-prepared film to 5.6 after irradiation at a fluence of 1×10^{15} ions/cm², and the Ti–O bond length increases from 1.99 to 2.03 Å. Further increase in ion fluence to 2×10^{15} ions/cm² do not result in any significant change in local atomic ordering.

For 10 MeV Cu ions, S_e and S_n are calculated to be 5.3 and 0.14 keV/nm, respectively, from SRIM-2013. Thus, although $S_e > S_n$, nuclear energy deposition is not negligible. Combining this information along with the observations above suggests that when irradiated with ions, the ions might initially displace atoms into voids, densifying and relaxing the film into a lower-energy amorphous state, which is preferred over crystallisation. As the mass density saturates, further irradiation leads to the rearrangement of atoms towards a lower-energy, ordered structure, resulting in nanocrystallites.

Similar to MeV ions, electrons also crystallise the a-TiO₂ film. Figure 6.5(d) shows the BF-STEM image of as-prepared TiO₂ film (with the corresponding FFT in the inset), after irradiation with 200 keV electrons at a fluence of $3.2 \times 10^8 \text{ e}^-/\text{nm}^2$. In this case, radiolysis and potential atomic displacements contribute to crystallisation, although atomic displacement by electrons is not prominent as by MeV ions. As observed from PDF analysis and mass density calculations, the as-prepared films are slightly stressed, under-dense and under-coordinated. When such films are irradiated with electrons, they may relax and release the stored defect energy, which can serve as an additional driving force for crystallisation.

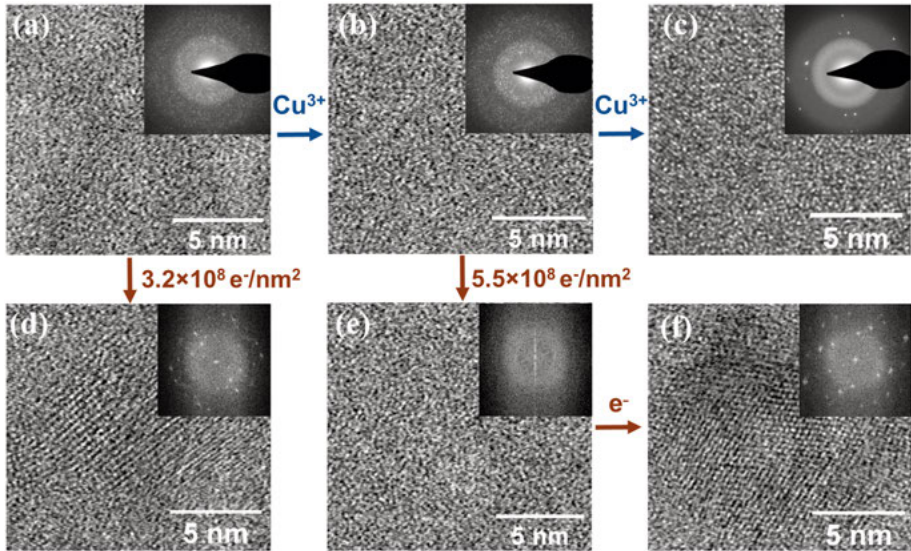


Figure 6.5 BF-STEM images, with the SAED image in the inset, of (a) the as-prepared TiO₂ film and after irradiation with 10 MeV Cu³⁺ ions at fluences of (b) 1×10^{15} and (c) 2×10^{15} ions/cm²; (d) BF-STEM image of as-prepared TiO₂ film, with the corresponding FFT in the inset, after electron irradiation at a fluence of $3.2 \times 10^8 \text{ e}^-/\text{nm}^2$; BF-STEM images of 10 MeV Cu ion-irradiated TiO₂ film (fluence: 1×10^{15} ions/cm²), with the corresponding FFT in the inset, after electron irradiation at fluences of (e) 5.5×10^8 and (f) $1.8 \times 10^9 \text{ e}^-/\text{nm}^2$. All the images are extracted from Paper IV.

However, when sequential irradiation with MeV ions and keV electrons is performed, an antagonistic effect on the crystallisation of a-TiO₂ is observed. Figure 6.5 shows the BF-STEM image of 10 MeV Cu ion-irradiated TiO₂ film (fluence: 1×10^{15} ions/cm²), with the corresponding FFT in the inset, after irradiation with 200 keV electrons at fluences of (e) 5.5×10^8 and (f) 1.8×10^9 e⁻/nm². For films pre-irradiated with MeV ions, the threshold electron fluence for crystallisation increases. As discussed above, MeV ion irradiation leads to densification and improved coordination number, and as a result, relaxes films into a lower-energy amorphous state. This relaxation makes it difficult to rearrange the atomic configuration in MeV irradiated films, i.e., higher energy is required to rearrange the atoms into a crystalline state under an electron beam. Compared to a threshold fluence of $(3.2 \pm 0.9) \times 10^8$ e⁻/nm² for crystallisation in the as-prepared TiO₂ film, a higher threshold electron fluence of $(1.7 \pm 0.15) \times 10^9$ e⁻/nm² is required for crystallisation in TiO₂ films pre-irradiated with MeV ions at a fluence of 1×10^{15} ions/cm². These results highlight the complex and antagonistic effects of sequential irradiation of two charged particles, viz., MeV ions and keV electrons, in amorphous oxides.

6.3. Tuning of resistive switching properties

TiO₂ thin films sandwiched between inert metals such as Pt and Pd exhibit resistive switching or memristor behaviour after an initialisation step referred to as electroforming [150]. In this step, a high voltage is applied across the sample, abruptly decreasing resistance by orders of magnitude, and the voltage at which this abrupt reduction in resistance occurs is called the electroforming voltage (V_{Ef}). This abrupt reduction in sample resistance is attributed to the formation of conducting paths of oxygen vacancies, called conductive filaments (CFs), between the two metal electrodes. Figure 6.6 shows the change in resistance when voltage sweeps are applied before and after electroforming in a typical as-prepared Pd/a-TiO₂/Pd memristor (schematic of the memristor structure in Figure 4.4 and TEM image in Figure 5.7(b)). Each switching cycle refers to two voltage sweeps: one along positive and the other along negative voltage. The sample has an initial resistance of 2.8×10^6 Ω, and after applying voltage sweeps with a maximum voltage (V_{max}) of 7 V, no significant decrease in resistance or consistent switching behaviour is observed. The resistance measured before and after the voltage sweep is referred to as resistance state 1 (RS1) and resistance state 2 (RS2), respectively, in Figure 6.6. At a voltage of 8.2 V, the sample is electroformed (shown by the green arrow in Figure 6.6), stable CFs connect the two electrodes, and the sample resistance decreases to 4.4×10^3 Ω. After electroforming, the sample can be switched between two resistance states by applying voltage sweeps of alternating polarity. This resistive switching is attributed to the rupturing and reformation of CFs formed during the electroforming step. The distinct

resistance states after electroforming are referred to as the high-resistance state (HRS) and low-resistance state (LRS).

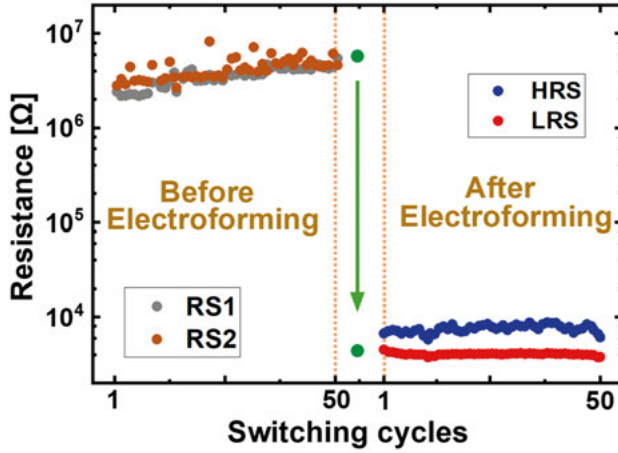


Figure 6.6 Resistance states for a typical as-prepared Pd/TiO₂/Pd sample. The green arrow indicates the electroforming step, corresponding to a decrease in sample resistance by a factor of $\sim 10^3 \Omega$.

To explore ion-induced tuning of switching properties of these memristors, the TiO₂ layer was implanted with two light ions of similar mass and collision cascades but different reactivity: oxygen (¹⁶O) and neon (²⁰Ne) ions. Ion implantation was performed without depositing Pd-TE to allow controlled introduction of defects in the TiO₂ layer. The RMS roughness of the TiO₂ surface, and thus, the Pd(TE)-TiO₂ interface roughness, decreases from $(730 \pm 57) \text{ pm}$ to 150-300 pm for all implantation conditions. Figure 6.7 shows the BF-STEM image for the cross-section of the samples implanted with 8 keV (a) ²⁰Ne and (b) ¹⁶O ions at a fluence of $2.93 \times 10^{16} \text{ ions/cm}^2$, with yellow lines showing the SRIM-2013 simulated concentration profiles for the corresponding ions. Compared to the as-prepared samples (Figure 5.7(b)), bright spots are observed in the BF-STEM images of the implanted samples. In the Ne-implanted samples, a bright-coloured sublayer, at a depth of (5-20) nm in the TiO₂ layer, corresponds to Ne atoms implanted in the TiO₂ layer (EDS colour map in Figure S2(d-e) in Paper V), which matches well with the SRIM-simulated implantation profile. In O-implanted samples, bright-coloured spots are observed in the STEM image, beginning at a depth of $(15 \pm 2) \text{ nm}$ in the TiO₂ layer. EDS measurements show no measurable change in oxygen profile across the TiO₂ layer after ¹⁶O implantation; therefore, these bright spots indicate the presence of local under-dense regions, suggesting local structural modifications.

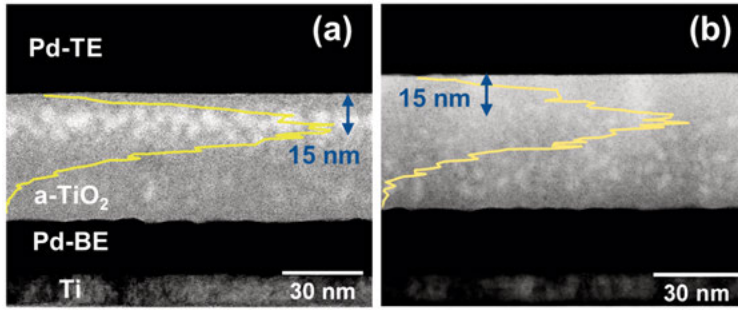


Figure 6.7 STEM images for the cross-sections of samples implanted with 8 keV (a) ^{20}Ne and (b) ^{16}O ions at a fluence of 2.93×10^{16} ions/cm². The yellow lines indicate the SRIM-2013 simulated concentration profiles for the corresponding 8 keV ions in the TiO₂/Pd layer. The image is extracted from Figure 2 in Paper V.

Figure 6.8 shows (a) the initial resistance and (b) V_{Ef} as a function of ion fluence. In Ne-implanted samples, the following changes are observed compared to as-prepared samples :

- a decrease in initial resistance of the sample (Figure 6.8(a))
- a decrease in V_{Ef} (Figure 6.8(b))
- the introduction of electroforming-free resistive switching (refer to Figure 6.8(c))

These modifications can be attributed to the generation of oxygen vacancies in Ne-implanted samples, as observed in the HAXPES spectra (Figure 5.10). The generation of oxygen vacancies affects the sample resistance and facilitates the formation of CFs (and thus, reduces V_{Ef}). The changes in oxygen vacancy profile at voltages below V_{Ef} result in switching without electroforming. The mechanism for electroforming-free resistive switching in Ne-implanted samples is discussed in Paper V. For ^{16}O -implanted samples, the following changes are observed compared to as-prepared samples:

- a slight decrease in initial resistance of the sample (Figure 6.8(a))
- a non-linear change in V_{Ef} , first increasing and then decreasing with ion fluence (Figure 6.8(b))
- the introduction of electroforming-free resistive switching at a fluence of 2.93×10^{16} ions/cm² (refer to Figure 6.8(c))

HAXPES spectra for ^{16}O -implanted samples show no significant introduction of oxygen vacancies in the TiO₂ layer. However, local structural modifications in the TiO₂ layer are observed in Figure 6.7(b), which can affect sample resistance and vacancy formation and migration under applied voltage. As a result, compared to the Ne-implanted samples, the reduction in initial resistance is lower, and electroforming-free resistive switching occurs between two

higher-resistance states and at higher voltages in ^{16}O -implanted samples. Figure 6.8(c) shows the resistance of samples over multiple cycles switched with voltage sweeps with $|V_{max}| < V_{Ef}$ (switched at $I_{cc} = 0.1$ mA). Figure 6.8(d) shows the retentivity, or stability, of the distinct resistance states at a constant voltage of 5 mV. The resistance states are unstable over time, indicating volatile or short-term memory in the samples exhibiting electroforming-free resistive switching.

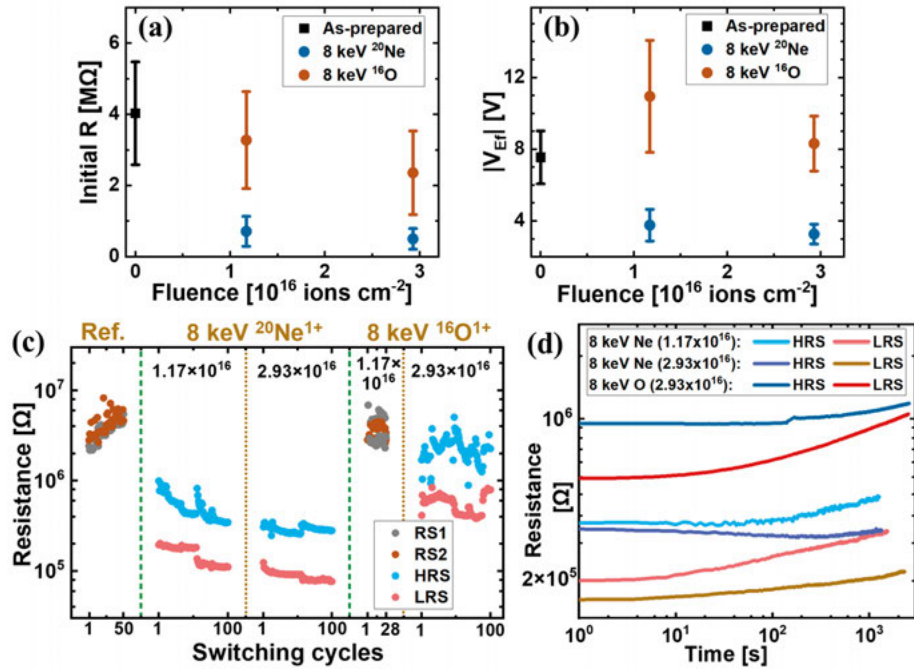


Figure 6.8 (a) Initial resistance and (b) V_{Ef} as a function of ion fluence; (c) Reproducibility or endurance of electroforming-free RS (at $I_{cc} = 0.1$ mA). As-prepared (or ‘Ref.’ in the figure) and the sample implanted with ^{16}O ions at a fluence of 1.17×10^{16} ions/cm² do not show electroforming-free resistive switching; (d) Retentivity of HRS and LRS for samples that exhibit electroforming-free resistive switching. The fluences mentioned in the subfigures (c) and (d) are in the units of ions/cm². Subfigures (a) and (b) are extracted from Figure 3, and subfigures (c) and (d) are extracted from Figure 4 in Paper V.

Post-electroforming, the rupturing and reformation of CFs contribute to switching in all samples. Both as-prepared and implanted samples show bipolar resistive switching with non-volatile memory. Figure 6.9 shows the (a) reproducibility or endurance (switched at $I_{cc} = 1$ mA) and (b) retentivity of resistance states after electroforming. The resistance states are stable over time, indicating non-volatile or long-term memory in the samples exhibiting resistive switching after electroforming. In Ne-implanted samples, the LRS decreases in the initial switching cycles. It can be attributed to an increase in

oxygen vacancy concentration and electroforming at a higher I_{cc} of 1 mA (compared to 0.1 mA in as-prepared samples), both of which may promote thicker CFs, resulting in a lower LRS [151,152]. The ^{16}O -implanted samples show an increase in HRS with ion fluence that reduces with each switching cycle. As a result, the resistance ratio ($R_{Ratio} = HRS/LRS$) degrades over switching cycles in ^{16}O -implanted samples. Both the HRS in the first switching cycle and the rate of decay of HRS with switching cycles increase with ^{16}O ion fluence. For samples with higher ^{16}O ion fluence (i.e., 2.93×10^{16} ions/cm 2), the HRS can be recovered by increasing the current, as shown in Figure 6.9(a), indicating that the HRS is recoverable. The green arrows correspond to the voltage sweep at $I_{cc} = 4$ mA (compared to $I_{cc} = 1$ mA), which resets the sample to a higher value of HRS.

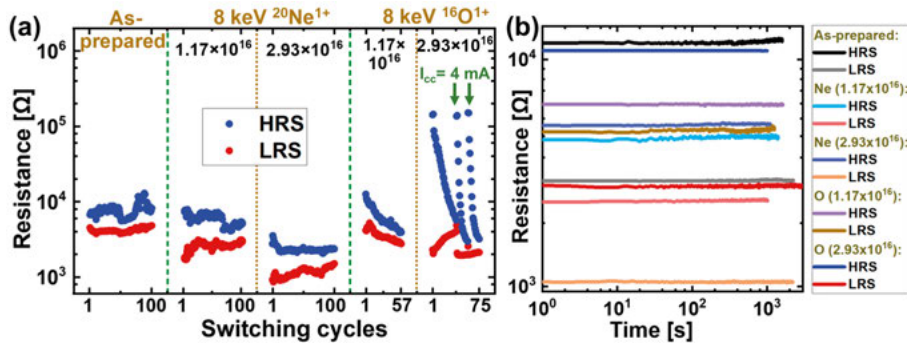


Figure 6.9 (a) Reproducibility or endurance and (b) retentivity of HRS and LRS observed for switching after electroforming. $I_{cc} = 1$ mA for all switching cycles in (a) except those marked by green arrows, where the sample was reset to HRS at $I_{cc} = 4$ mA. The fluences mentioned in the figures are in the units of ions/cm 2 . The image is based on Figure 6 in Paper V.

To investigate further the underlying mechanisms of different switching modes observed in samples implanted with ^{16}O ions at a 2.93×10^{16} ions/cm 2 , ^{18}O isotope tracing with NRA was employed. For samples implanted with ^{18}O ions and kept under vacuum, the ^{18}O concentration profile does not change significantly over time, as shown in Figure 5.4(a). The stability of the ^{18}O profile indicates that in the absence of external driving forces such as voltage, there is no significant oxygen diffusion or isotopic-exchange hopping. Thus, any major changes in ^{18}O concentration profiles observed after switching can be attributed to voltage sweeps applied across the memristor sample. When one of the ^{18}O -implanted samples undergoes electroforming-free resistive switching for 53 cycles (i.e., 106 voltage sweeps with alternating polarity), the ^{18}O concentration profile shifts toward the Pd-TE, with a significant amount of ^{18}O present in the Pd-TE, as shown in Figure 5.4(b). As the last voltage sweep was along the positive voltage, migration of $^{18}\text{O}^{2-}$ ions, and thus a shift in the profile towards Pd-TE can be expected. The $^{18}\text{O}^{2-}$ ions are reduced at

the top Pd-TiO₂ interface and can either form interfacial PdO_x or segregate to grain boundaries or other defect sites in the polycrystalline Pd layer [152,153], which explains the presence of ¹⁸O concentration in Pd-TE.

Figure 6.10(a) shows the ¹⁸O concentration profiles for two samples switched for 200 and 500 cycles, respectively, after electroforming with a non-cycled sample. ¹⁸O concentration is present in the Pd-TE for both switched samples, resulting from the reduction of ¹⁸O²⁻ ions at the Pd-TiO₂ interface. However, the ¹⁸O concentration in the Pd-TE is lower for the sample switched for 500 cycles. In the TiO₂ layer, the ¹⁸O concentration decreases in the first half of the film with increasing switching cycle, while no significant difference is observed in the second half of the film. The evolution of ¹⁸O concentration with increasing switching cycles can be attributed to the cumulative effect of multiple voltage sweeps applied across the sample.

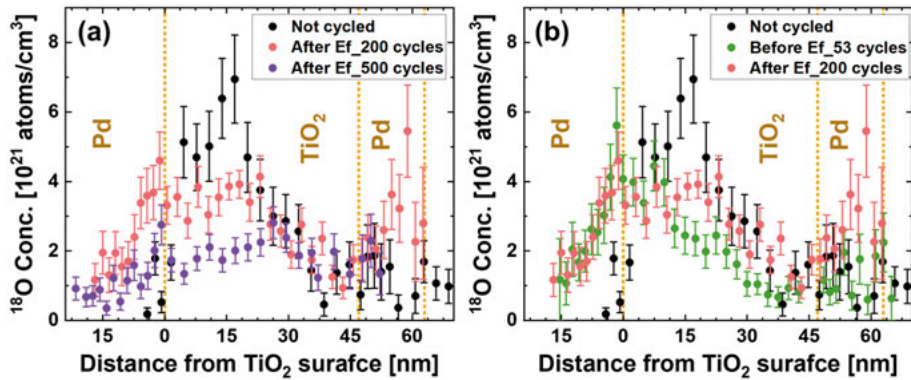


Figure 6.10 Comparison of the ¹⁸O concentration profile between (a) two samples switched for 200 and 500 cycles, respectively, after electroforming; and (b) one sample with 53 electroforming-free switching cycles and one sample with 200 cycles after electroforming. The x-axis plots the distance in reference to the top Pd-TiO₂ interface. Subfigures (a) and (b) are extracted from Figures 4 and 3(b) in Paper VI.

Figure 6.10(b) compares the ¹⁸O concentration profile of a sample with 53 electroforming-free switching cycles with a sample switched for 200 cycles after electroforming. The two samples show similar concentration profiles. It is important to note that the 53 electroforming-free switching cycles were performed along voltage sweeps with $V_{max} = \pm 8$ V, whereas after electroforming, the sample was switched at a lower voltage ($V_{max} = \pm 2$ V). As both oxygen reduction at the Pd interface and drift velocity depend on applied voltage [154], the cumulative effect of 53 switching cycles at high voltage and 200 cycles at low voltage can result in a similar average concentration profile.

Overall, these results demonstrate that defect engineering by ion implantation can be used to tune switching properties, such as the initial electroforming process and to introduce different switching modes (electroforming-free resistive switching with volatile memory, and weighted resistive switching with

recoverable resistance states and non-volatile memory). In Ne-implanted samples, observed modifications in switching properties are primarily dominated by the introduction of a reservoir of oxygen vacancies. In contrast, implantation with ^{16}O ions at identical energy and fluence predominantly introduces local structural modifications within the sample, leading to distinctly different switching properties, while still governed by vacancy migration, as indicated by complementary ^{18}O isotopic tracing. ^{18}O isotope tracing with NRA shows that under the applied voltage, the ^{18}O concentration profile evolves, indicating oxygen (or oxygen vacancy) migration during resistive switching in O-implanted memristor structures.

7. Conclusions and outlook

In this thesis, energy deposition by energetic ions and its correlation to observable changes in structural and material properties in three different material systems, *viz.*, single-crystal CaF_2 , polyimide (PI) foils and amorphous TiO_2 films, was investigated, exploring ions as potential candidates for forming nanostructures and tuning material properties. Ions with kinetic energies in both MeV and keV regimes were studied, targeting distinct modifications: MeV ions for nanoscale structural modifications and keV ions for tuning of material properties.

MeV ion irradiation of single-crystal CaF_2 , a non-amorphizable insulator, leads to the formation of surface nanostructures above a certain threshold in electronic stopping power (S_e). Similarly, in PI foils, MeV ion irradiation leads to the formation of ion tracks above a certain threshold S_e . This threshold S_e increases with the ion velocity, because at the given S_e , the energy density and thereby the damage induced by ions depends on ion velocity. As a result, the velocity-dependent threshold S_e for nanostructure formation by MeV ions is lower than that reported for similar nanostructure formation by swift heavy ions. However, if the materials are irradiated with ions with an initial charge (q_{in}) below the equilibrium charge state (q_{eq}), the energy deposited in the initial layers of the material is lower, and the threshold S_e is achieved at a certain depth in the material (on the length scales of nanometres for MeV ions). This charge dependence was experimentally observed in PI foils, where the ion tracks started at a certain depth and not on the surface when the foils were irradiated with ions with $q_{in} < q_{eq}$. The experimental results match well with theoretical models of charge equilibration discussed in Chapter 2, offering a practical framework for analysing and predicting charge evolution and its effects on ion track formation.

Extending on this approach, the modification of amorphous TiO_2 films under MeV ion irradiation was studied. From PDF analysis and mass density calculations, sputter-deposited a- TiO_2 films were slightly stressed, underdense and under-coordinated. Irradiation with 10 MeV Cu ions densifies the film, increases the coordination number and thus, relaxes the film. Initial irradiation relaxes the film into a lower-energy amorphous state by displacing the atoms into voids, and further irradiation leads to the rearrangement of atoms towards an even lower-energy state, resulting in nanocrystallites. In the case of irradiation with 200 keV electrons, radiolysis and potential atomic

displacements lead to crystallisation of a-TiO₂ films. However, as MeV ion irradiation relaxes the films into a lower-energy amorphous state, it becomes difficult to rearrange the atoms under keV electron irradiation in films pre-irradiated with MeV ions. This observation shows that MeV ions and keV electrons have an antagonistic influence on the crystallisation of a-TiO₂ films.

Implantation with keV ions induces local structural modifications in a-TiO₂ films, leading to changes in resistive switching properties of Pd/TiO₂/Pd memristor structures. ¹⁶O-implantation induces local under-dense regions in the film, whereas the overall stoichiometry and oxygen concentration across the film remain primarily unchanged. As a result, a slight change in sample resistance and electroforming voltage (V_{Ef}) is observed. At a fluence of 2.93×10^{16} ions/cm², electroforming-free resistive switching with volatile memory in addition to resistive switching with weighted and recoverable resistance states and non-volatile memory is observed in O-implanted samples. Although no significant increase in oxygen vacancies is observed from XPS and HAX-PES measurements, ¹⁸O isotope tracing with NRA shows that switching is governed by vacancy motion, as the evolution of ¹⁸O concentration profile with resistive switching (both before and after electroforming) is observed. Ne-implantation introduces a reservoir of oxygen vacancies (observed in HAXPES measurements) in addition to local structural modifications, leading to distinctly different switching properties. In Ne-implanted samples, the sample resistance and V_{Ef} reduce, and electroforming-free resistive switching occurs at a lower voltage (voltage sweeps with a maximum voltage of ± 2 V, compared to ± 6 V for ¹⁶O-implanted samples). These results show that ion implantation can be used to tune switching properties and modes by controlled introduction of defects, such as oxygen vacancies, and by modifying atomic migration through changes in local structures.

The results presented in this thesis demonstrate that energetic ions provide a versatile tool for tailoring structural and functional properties. At the same time, the thesis opens promising directions for future research, both on fundamental ion-matter interactions and application-oriented nanoscale engineering. This work verifies and quantifies the velocity dependence of thresholds in S_e for nanostructure formation in the MeV regime. Experiments with varying ion velocity at a given S_e , combined with theoretical modelling, can provide insights into ion track formation and surface nanostructure formation in the MeV regime. Coupling simulations with experiments on the evolution of nanoscale modifications with the ion charge state could provide a predictive framework for nanostructure engineering using MeV ions.

To further improve our understanding of the switching mechanism in TiO₂ memristors, NRA can be employed for operando measurements to track compositional changes in real time and overcome the challenges arising from device-to-device and cycle-to-cycle variability after electroforming. Comparing samples with the identical switching histories but different resistance states, or the same resistance state reached through different numbers of cycles, can

provide deeper insights into the switching mechanism. From an application perspective, tuning of switching properties in TiO₂-based memristors demonstrates the strong potential of ions as a tool for defect engineering. Since device-to-device variability in memristors is often linked to the electroforming process, introducing a pre-defined path for filament formation may help to localise filament growth and thereby improve reproducibility. In this context, MeV ions offer a possibility of deliberately creating ion tracks as a preferential pathway for filament formation. Such controlled defect engineering could guide filament formation, potentially reducing device-to-device variability.

In conclusion, this thesis investigates the fundamental interactions between energetic ions and matter across diverse material systems, ranging from single crystals, amorphous oxides and polymer foils. These results provide insights into non-equilibrium processes, atomic-scale energy transfer, and the relation between fundamental ion-matter interactions and observable material modifications. By understanding these energy-transfer processes and their dependence on ion and material properties, ions can be used as precision tools for nanoscale engineering, ranging from the formation of nanoscale structures to tuning material properties for improved devices.

8. Sammanfattning

Växelverkan mellan energirika joner och material utgör ett grundläggande forskningsområde inom fasta tillståndets fysik. När en energirik jon träder in i ett målmaterial växelverkar den med både elektronerna och atomkärnorna i materialet. Sådan växelverkan leder till en kontinuerlig överföring av jonens energi till målmaterialiet, vilket i sin tur ger upphov till förflyttning av atomer, elektroniska excitationer, jonisering och i vissa fall kärnreaktioner. Dessa energiöverföringsprocesser driver materialet bort från termodynamisk jämvikt och resulterar i förändringar av strukturella, elektriska, optiska samt mekaniska egenskaper. Eftersom joners energideponering sker på mycket kortare tids-skalar än termisk och strukturell jämviktsinställning kan joner föra materialet in i transienta tillstånd som inte är tillgängliga under jämviktsförhållanden.

Nanostrukturering och modifiering av materialegenskaper med joner har studerats i stor utsträckning för joner vars kinetiska energi som sträcker sig från ett fåtal eV till flera GeV. Vid energier från eV till ett fåtal keV sker energiöverföring främst genom elastiska kollisioner med målatomernas kärnor, vilket skapar förskjutningskaskader och ger upphov till vakanser, interstitiella atomer och defektkluster, samt lokal uppvärmning i materialet. Vid GeV-energies, som ligger i den andra änden av det energiintervall som studeras för materialmodifiering, dominerar energiförlusten av snabba elektroniska excitationer och jonisering. Detta resulterar i starkt lokaliserad elektronisk energideponering längs jonens bana, vilket ger upphov till så kallade jonspår. Mellan dessa ytterlighetsregimer finns joner med energier mellan några hundra keV och tiotals MeV, där både inelastiska elektroniska excitationer och elastiska nukleära kollisioner kan bidra signifikant till energiöverföringen. Energideponeringen kan också styras genom jonens egenskaper, t.ex., massa och laddning. Genom att förstå dessa relevanta energiöverföringsprocesser och deras komplexa samspel kan en hög grad av kontroll uppnås över typen, positionen och omfattningen av joninducerad materialmodifiering. Därmed erbjuder jonstrålebaserade metoder tillförlitliga, mycket reproducerbara och effektiva sätt att framställa nanostrukturer och skräddarsy materialegenskaper.

Denna avhandling undersöker hur energideponering från energirika joner leder till förändringar i de strukturella och funktionella egenskaperna hos olika materialsystem, nämligen enkristallint CaF_2 , folier av polyimid och amorfa TiO_2 -filmer. Olika materialsystem studeras eftersom energiöverföringsprocesser och resulterade modifiering beror på materialegenskaper såsom

densitet, sammansättning, värmeledningsförmåga och kristallinitet. Joner med både keV- och MeV-energies används med olika syften: MeV-joner för strukturell modifiering på nanoskala och keV-joner för modifiering av funktionella egenskaper. Genom att kombinera dessa studier syftar avhandlingen till att koppla de grundläggande växelverkningsarna mellan joner och materia till observerbara strukturella och funktionella förändringar.

MeV-jonbestrålning av enkristallin CaF_2 , en icke-amorfiserbar isolator, leder till bildning av ytnanostrukturer över ett visst tröskelvärde i den elektroniska stoppkraften (S_e), det vill säga den energi som deponeras i det elektroniska delsystemet per längdenhet som jonen färdas. På liknande sätt leder MeV-jonbestrålning av polyimidfolier till bildning av jonspår över ett visst tröskelvärde för S_e . Detta tröskelvärde i S_e för nanostrukturbildning med MeV joner beror på jonhastigheten och är lägre än det som rapporterats för liknande nanostrukturbildning med snabba tunga joner med GeV energier.

Om materialen däremot bestrålas med joner med initial laddning (q_{in}) under jämviktsladdningstillståndet (q_{eq}), är energin som deponeras i materialets inledande skikt reducerat, och tröskelvärde för S_e uppnås först på ett visst djup. Detta observerades experimentellt i polyimidfolier, där jonspåren började under ytan snarare än vid densamma när folierna bestrålades med joner med $q_{in} < q_{eq}$. De experimentella resultaten överensstämde väl med teoretiska modeller för laddningsutjämning och erbjuder ett praktiskt ramverk för att analysera och förutsäga laddningsutveckling och dess effekter på jonspårsbildning.

Med utgångspunkt i detta angreppssätt studeras modifieringen av amorfa TiO_2 (a- TiO_2) filmer under MeV-jonbestrålning. Utifrån analys av parfordelningsfunktioner (Pair Distribution Function, PDF) och massdensitet visade sig sputterdeponerade a- TiO_2 -filmer vara svagt spända, underdensifierade och underkoordinerade. Bestrålning med MeV-joner förtätar filmen, ökar koordinationsantalet och relaxerar därmed filmen. Initial bestrålning relaxerade filmen till ett amorft tillstånd med längre energi genom att atomer försköts in i hålrum, och fortsatt bestrålning ledde till omordning av atomer mot en ännu lägre energinivå och mer ordnad struktur, vilket resulterade i nanokristaller. Vid elektronbestrålning leder radiolys och möjliga atomära förskjutningar till kristallisering av a- TiO_2 -filmer, även om atomförskjutningar orsakade av elektroner inte är lika framträdande som för MeV-joner. Eftersom MeV-jonbestrålning relaxerar filmerna till ett amorft tillstånd med lägre energi blir det svårare att omordna atomer under elektronbestrålning. Detta visar att MeV joner och elektroner har en antagonistisk inverkan på kristalliseringen av a- TiO_2 -filmer.

Implantering med keV-joner inducerar lokala strukturella modifieringar i a- TiO_2 -filmer, vilket leder till förändringar i de resistiva omkopplingssegenskaperna (Resistive Switching, RS) hos Pd/ TiO_2 /Pd memristorstrukturer. Denna avhandling visar att defektbildning genom jonimplantering kan användas för att styra omkopplingssegenskaperna, t.ex., elektroformingsprocessen, samt för att introducera olika omkopplingssegenskaper (elektroformingsfri

RS med kortvarigt minne samt viktad RS med återställningsbara resistansnivåer och långvarigt minne). I Ne-implanterade prover dominerar de observerade förändringarna i RS-egenskaper främst av införandet av en reservoar av syrevakanser. Däremot leder implantation med ^{16}O joner vid identisk energi och totalflöde huvudsakligen till strukturella förändringar i provet, vilket resulterar i tydligt annorlunda omkopplingsegenskaper, även om de fortfarande styrs av vakansmigration, vilket indikeras av kompletterande isotopspårning med ^{18}O . Isotopspårningen med ^{18}O med hjälp av kärnreaktionsanalys (Nuclear Reaction Analysis, NRA) visar att ^{18}O koncentrationsprofilen utvecklas under applicerad spänning i samband med RS, vilket påvisar migration av syre (eller syrevakanser) under applicerad spänning i O-implanterade memristorsturukturer.

Sammanfattningsvis undersöker denna avhandling den grundläggande växelverkan mellan energirika joner och materia i olika materialsystem, från enkristaller och amorfa oxider till polymerfolier, med fokus på att framkalla materialförändringar. Resultaten ger insikter i förståelsen av icke-jämviktsprocesser, energiöverföring på atomär skala samt sambandet mellan grundläggande jon-materialinteraktion och observerbar materialmodifiering. Genom att förstå energiöverföringsprocesser och deras beroende av jon- och materialegenskaper kan joner användas som precisionsverktyg på nanoskala, från bildning av nanostrukturer till justering av materialegenskaper för förbättrade elektroniska enheter.

Acknowledgements

I want to express my heartfelt gratitude to everyone who has supported and encouraged me throughout my journey towards this doctoral thesis. While this work carries my name, it is truly the result of the guidance, generosity, laughter, and kindness of many remarkable people who have shaped both my research and my experience along the way.

First and foremost, I owe my deepest gratitude to my principal supervisor Petter Ström. Thank you for your invaluable mentorship, steady encouragement and unwavering belief in my abilities, even on days when the experiments seemed determined not to cooperate. Your calm and optimistic perspective, combined with your thoughtful guidance, has shaped not only this thesis but also my approach to scientific challenges and life. I am truly grateful for your patience and trust throughout the journey.

I would also like to warmly thank my co-supervisor, Daniel Primetzhofer, for always being ready to discuss ideas, provide guidance, and offer encouragement. Your patience in answering questions, your challenges that inspired me to think critically, and your consistent support pushed me to do better. The insightful discussions we had not only sharpened my thinking but also made the journey more engaging and inspiring. I am truly grateful for your mentorship and for always being there whenever I needed guidance.

My sincere appreciation also goes to my co-supervisor, Tuan Thien Tran, for the enriching scientific discussions, steady support, and invaluable assistance with the TEM measurements. Your expertise and guidance were essential to the progress of this work, and our discussions have greatly shaped my understanding and approach to research.

I also want to express my sincere appreciation to Dr Katharina Lorenz for agreeing to be my opponent at the thesis defence. Additionally, I would like to thank Prof. Maria-Eugenia Toimil-Molares, Dr Hermann Rothard, Dr Mariana Dalarsson, and Dr Germán Salazar Alvares for being part of the examination committee, as well as Prof. Gabriella Andersson for chairing the doctoral defence.

I am deeply grateful to the engineers at Tandem Laboratory, Bart Royeard, Sven Cederberg, Petko Chervnev and Joakim Andersson, for their indispensable assistance in the laboratory. Your technical expertise and practical problem-solving skills saved more than a few experiments. Many thanks to Amit Patel for guiding me through AFM and SEM measurements in the cleanroom;

Yuan Zhu for guidance with electrical measurements and thoughtful discussions on designing a working memristor structure; Zhen Zhang for insightful and valuable discussions on memristors; Rebecka Lindbald and Gunnar K. Pålsson for sharing their expertise on XPS measurements and PDF analysis.

To the entire Tandem Laboratory and Materials Physics division: thank you for creating not only a productive research environment but also a genuinely enjoyable one - Kristina, Jila, Mauricio, Aishee, Aastha, Eleni, Dmitrii, Daniel, Radek, Philip, Robbie, Eduardo, Svenja, Theofanis, Athanasios, Ghada, Kevin, Carolin, Barbara, Gyula, Robert, André, Johan, Melanie, Mona, Christina, Caroline, Sára, Victor, Jonas, Anja and many others whose friendship and support enriched the experience. A special thanks to Kristina for being such a wonderful office buddy, sharing both focused workdays and well-timed laughter. I treasure the shared moments beyond the laboratory: barbecues under the Swedish summer sky (or in Swedish rain), spontaneous after-work, fika breaks that turned into long conversations, playing badminton after work, and celebrations that reminded us there is life beyond experiments and data analysis.

I also extend my appreciation to the administration, whose help with practical matters kept everything running.

To my friends from India, scattered across the globe yet always close at heart: thank you for your encouragement and love. To all my friends I made in Sweden, thank you for becoming my family away from home. Celebrating festivals together, cooking meals, exploring Europe and sharing laughter over everyday moments have made this chapter of life unforgettable.

Finally, I want to thank my parents, who have been my greatest source of strength. Your love, guidance and unwavering belief in me have shaped who I am. Even though we were 6000 km apart, the moments we shared via video calls, messages or pictures made all the difference. Thanks to my brother, who has also been a constant source of light and laughter. Your small jokes and constant reminders of how proud you are of me always bring a smile to my face.

From the bottom of my heart, thank you all for being part of this journey!

Rajdeep Kaur
Uppsala, Sweden

References

- [1] L. Luneville, P. Garcia, D. Simeone, Predicting Nonequilibrium Patterns beyond Thermodynamic Concepts: Application to Radiation-Induced Microstructures, *Phys. Rev. Lett.* 124 (2020) 085701. <https://doi.org/10.1103/PhysRevLett.124.085701>.
- [2] B. Zhao, F. Zeng, F. Pan, Formation of metastable alloy films in the Ni-Mo binary system by ion-beam-assisted deposition, *Appl. Phys. A* 77 (2003) 523–528. <https://doi.org/10.1007/s00339-002-1482-9>.
- [3] R.G. Musket, Applications of Ion Track Lithography in Vacuum Microelectronics, *MRS Proc.* 621 (2000) R1.2.1. <https://doi.org/10.1557/PROC-621-R1.2.1>.
- [4] D. Kaya, K. Keçeci, Review—Track-Etched Nanoporous Polymer Membranes as Sensors: A Review, *J. Electrochem. Soc.* 167 (2020) 037543. <https://doi.org/10.1149/1945-7111/ab67a7>.
- [5] T. Yamauchi, K. Matsukawa, Y. Mori, M. Kanasaki, A. Hattori, Y. Matai, T. Kusumoto, A. Tao, K. Oda, S. Kodaira, T. Konishi, H. Kitamura, N. Yasuda, R. Barillon, Applicability of Polyimide Films as Etched-Track Detectors for Ultra-Heavy Cosmic Ray Components, *Appl. Phys. Express* 6 (2013) 046401. <https://doi.org/10.7567/APEX.6.046401>.
- [6] D.K. Avasthi, G.K. Mehta, *Swift Heavy Ions for Materials Engineering and Nanostructuring*, Springer Science+Business Media B.V. Springer e-books, Dordrecht, 2011.
- [7] W. Ensinger, Modification of materials by irradiation of heavy ions with energies from keV to GeV, *Radiat. Meas.* 40 (2005) 712–721. <https://doi.org/10.1016/j.radmeas.2005.06.026>.
- [8] I. Sulania, A. Tripathi, D. Kabiraj, S. Varma, D.K. Avasthi, keV Ion-Induced Effective Surface Modifications on InP, *J. Nanosci. Nanotechnol.* 8 (2008) 4163–4167. <https://doi.org/10.1166/jnn.2008.AN13>.
- [9] P. Ström, S. Ghorai, T.T. Tran, D. Primetzhofer, Synthesis of ferromagnetic thin films and engineering of their magnetic properties by Fe ion implantation in polycrystalline Pd, *J. Magn. Magn. Mater.* 552 (2022) 169207. <https://doi.org/10.1016/j.jmmm.2022.169207>.
- [10] T.T. Tran, H. Bruce, N.H. Pham, D. Primetzhofer, A contactless single-step process for simultaneous nanoscale patterning and cleaning of large-area graphene, *2D Mater.* 10 (2023) 025017. <https://doi.org/10.1088/2053-1583/acc042>.
- [11] C. Trautmann, S. Bouffard, R. Spohr, Etching threshold for ion tracks in polyimide, *Nucl. Instrum. Methods Phys. Res. Sect. B Beam Interact. Mater. At.* 116 (1996) 429–433. [https://doi.org/10.1016/0168-583X\(96\)00083-3](https://doi.org/10.1016/0168-583X(96)00083-3).
- [12] M. Toulemonde, A. Benyagoub, C. Trautmann, N. Khalfaooui, M. Boccanfuso, C. Dufour, F. Gourbilleau, J.J. Grob, J.P. Stoquert, J.M. Costantini, F. Haas, E. Jacquet, K.-O. Voss, A. Meftah, Dense and nanometric electronic excitations induced by swift heavy ions in an ionic CaF₂ crystal: Evidence for two thresholds of damage creation, *Phys. Rev. B* 85 (2012) 054112. <https://doi.org/10.1103/PhysRevB.85.054112>.

- [13] J.R.A. Godinho, S. Piazzolo, M.C. Stennett, N.C. Hyatt, Sintering of CaF₂ pellets as nuclear fuel analog for surface stability experiments, *J. Nucl. Mater.* 419 (2011) 46–51. <https://doi.org/10.1016/j.jnucmat.2011.08.031>.
- [14] W. Yan, V.K.S. Hsiao, Y.B. Zheng, Y.M. Shariff, T. Gao, T.J. Huang, Towards nanoporous polymer thin film-based drug delivery systems, *Thin Solid Films* 517 (2009) 1794–1798. <https://doi.org/10.1016/j.tsf.2008.09.080>.
- [15] D. Cohen-Tanugi, J.C. Grossman, Water Desalination across Nanoporous Graphene, *Nano Lett.* 12 (2012) 3602–3608. <https://doi.org/10.1021/nl3012853>.
- [16] A. Mara, Z. Siwy, C. Trautmann, J. Wan, F. Kamme, An Asymmetric Polymer Nanopore for Single Molecule Detection, *Nano Lett.* 4 (2004) 497–501. <https://doi.org/10.1021/nl035141o>.
- [17] O.A. Saleh, L.L. Sohn, An Artificial Nanopore for Molecular Sensing, *Nano Lett.* 3 (2003) 37–38. <https://doi.org/10.1021/nl0255202>.
- [18] T. Yamauchi, S. Kaifu, Y. Mori, M. Kanasaki, K. Oda, S. Kodaira, T. Konishi, N. Yasuda, R. Barillon, Applicability of the polyimide films as an SSNTD material, *Radiat. Meas.* 50 (2013) 16–21. <https://doi.org/10.1016/j.radmeas.2012.04.013>.
- [19] X. Xiang, Z. He, J. Rao, Z. Fan, X. Wang, Y. Chen, Applications of Ion Beam Irradiation in Multifunctional Oxide Thin Films: A Review, *ACS Appl. Electron. Mater.* 3 (2021) 1031–1042. <https://doi.org/10.1021/acsaelm.0c01071>.
- [20] X. Han, G. Wu, J. Du, J. Pi, M. Yan, X. Hong, Metal and metal oxide amorphous nanomaterials towards electrochemical applications, *Chem. Commun.* 58 (2022) 223–237. <https://doi.org/10.1039/D1CC04141J>.
- [21] S. Yan, K.P. Abhilash, L. Tang, M. Yang, Y. Ma, Q. Xia, Q. Guo, H. Xia, Research Advances of Amorphous Metal Oxides in Electrochemical Energy Storage and Conversion, *Small* 15 (2019) 1804371. <https://doi.org/10.1002/sml.201804371>.
- [22] S. Park, M. Naqi, N. Lee, S. Park, S. Hong, B.H. Lee, Recent Advancements in 2D Material-Based Memristor Technology Toward Neuromorphic Computing, *Micromachines* 15 (2024) 1451. <https://doi.org/10.3390/mi15121451>.
- [23] G.U. Kamble, A.P. Patil, R.K. Kamat, J.H. Kim, T.D. Dongale, Promising Materials and Synthesis Methods for Resistive Switching Memory Devices: A Status Review, *ACS Appl. Electron. Mater.* 5 (2023) 2454–2481. <https://doi.org/10.1021/acsaelm.3c00062>.
- [24] P. Ström, D. Primetzhofner, Energy deposition by nonequilibrium charge states of MeV I 127 in Au, *Phys. Rev. A* 103 (2021) 022803. <https://doi.org/10.1103/PhysRevA.103.022803>.
- [25] XXVIII. Electron Capture and Loss by Heavy Ions Penetrating through Matter, in: Niels Bohr Collect. Works, Elsevier, 1987: pp. 593–625. [https://doi.org/10.1016/S1876-0503\(08\)70178-6](https://doi.org/10.1016/S1876-0503(08)70178-6).
- [26] V.S. Nikolaev, I.S. Dmitriev, On the equilibrium charge distribution in heavy element ion beams, *Phys. Lett. A* 28 (1968) 277–278. [https://doi.org/10.1016/0375-9601\(68\)90282-X](https://doi.org/10.1016/0375-9601(68)90282-X).
- [27] K. Shima, T. Ishihara, T. Mikumo, Empirical formula for the average equilibrium charge-state of heavy ions behind various foils, *Nucl. Instrum. Methods Phys. Res.* 200 (1982) 605–608. [https://doi.org/10.1016/0167-5087\(82\)90493-8](https://doi.org/10.1016/0167-5087(82)90493-8).
- [28] G. Schiwietz, P.L. Grande, Improved charge-state formulas, *Nucl. Instrum. Methods Phys. Res. Sect. B Beam Interact. Mater. At.* 175–177 (2001) 125–131. [https://doi.org/10.1016/S0168-583X\(00\)00583-8](https://doi.org/10.1016/S0168-583X(00)00583-8).

- [29] G. Schiwietz, K. Czerski, M. Roth, F. Staufenbiel, P.L. Grande, Femtosecond dynamics – snapshots of the early ion-track evolution, *Nucl. Instrum. Methods Phys. Res. Sect. B Beam Interact. Mater. At.* 226 (2004) 683–704. <https://doi.org/10.1016/j.nimb.2004.05.043>.
- [30] J.F. Ziegler, M.D. Ziegler, J.P. Biersack, SRIM – The stopping and range of ions in matter (2010), *Nucl. Instrum. Methods Phys. Res. Sect. B Beam Interact. Mater. At.* 268 (2010) 1818–1823. <https://doi.org/10.1016/j.nimb.2010.02.091>.
- [31] W.H. Bragg, R. Kleeman, XXXIX. On the α particles of radium, and their loss of range in passing through various atoms and molecules, *Lond. Edinb. Dublin Philos. Mag. J. Sci.* 10 (1905) 318–340. <https://doi.org/10.1080/14786440509463378>.
- [32] M. Mayer, SIMNRA User’s Guide, Rep. IPP 9113 Max Plank-Inst. Plasma-phys. Garch. Ger. (1997).
- [33] E. Fermi, E. Teller, The Capture of Negative Mesotrons in Matter, *Phys. Rev.* 72 (1947) 399–408. <https://doi.org/10.1103/PhysRev.72.399>.
- [34] J. Lindhard, M. Scharff, Energy Dissipation by Ions in the keV Region, *Phys. Rev.* 124 (1961) 128–130. <https://doi.org/10.1103/PhysRev.124.128>.
- [35] F. Matias, R.C. Fadanelli, P.L. Grande, N.R. Arista, N.E. Koval, G. Schiwietz, Stopping power of cluster ions in a free-electron gas from partial-wave analysis, *Phys. Rev. A* 98 (2018) 062716. <https://doi.org/10.1103/PhysRevA.98.062716>.
- [36] F. Bivort Haiek, A.M.P. Mendez, C.C. Montanari, D.M. Mitnik, ESPNN: A novel electronic stopping power neural-network code built on the IAEA stopping power database. I. Atomic targets, *J. Appl. Phys.* 132 (2022) 245103. <https://doi.org/10.1063/5.0130875>.
- [37] International Atomic Energy Agency (IAEA)- Electronic Stopping Power of Matter in Ions, *Int. At. Energy Agency IAEA- Electron. Stopping Power Matter Ions* (n.d.). https://www-nds.iaea.org/stopping/stopping_intr.html (accessed November 7, 2023).
- [38] G.L. Nealon, B. Donnio, R. Greget, J.-P. Kappler, E. Terazzi, J.-L. Gallani, Magnetism in gold nanoparticles, *Nanoscale* 4 (2012) 5244. <https://doi.org/10.1039/c2nr30640a>.
- [39] F. Gao, Z. Gu, Melting Temperature of Metallic Nanoparticles, in: M. Aliofkhaezai (Ed.), *Handb. Nanoparticles*, Springer International Publishing, Cham, 2015: pp. 1–25. https://doi.org/10.1007/978-3-319-13188-7_6-1.
- [40] B. Mekuye, B. Abera, Nanomaterials: An overview of synthesis, classification, characterization, and applications, *Nano Sel.* 4 (2023) 486–501. <https://doi.org/10.1002/nano.202300038>.
- [41] K.-H. Huynh, X.-H. Pham, J. Kim, S.H. Lee, H. Chang, W.-Y. Rho, B.-H. Jun, Synthesis, Properties, and Biological Applications of Metallic Alloy Nanoparticles, *Int. J. Mol. Sci.* 21 (2020) 5174. <https://doi.org/10.3390/ijms21145174>.
- [42] Sumitomo Heavy Industries Group, (n.d.). <https://www.shi.co.jp/english/products/machinery/ion/index.html>.
- [43] T. Peters, C. Haake, J. Hopster, V. Sokolovsky, A. Wucher, M. Schleberger, HICS: Highly charged ion collisions with surfaces, *Nucl. Instrum. Methods Phys. Res. Sect. B Beam Interact. Mater. At.* 267 (2009) 687–690. <https://doi.org/10.1016/j.nimb.2008.11.024>.

- [44] R. Ritter, R.A. Wilhelm, R. Ginzl, G. Kowarik, R. Heller, A.S. El-Said, R.M. Papaléo, W. Rupp, J.R. Crespo López-Urrutia, J. Ullrich, S. Facsko, F. Aumayr, Pit formation on poly(methyl methacrylate) due to ablation induced by individual slow highly charged ion impact, *EPL Europhys. Lett.* 97 (2012) 13001. <https://doi.org/10.1209/0295-5075/97/13001>.
- [45] M. Tona, Y. Fujita, C. Yamada, S. Ohtani, Electronic interaction of individual slow highly charged ions with TiO₂ (110), *Phys. Rev. B* 77 (2008) 155427. <https://doi.org/10.1103/PhysRevB.77.155427>.
- [46] P. Li, H. Zhang, L. Wei, B. Niu, H. Yuan, Z. Cheng, H. Zhang, Z. Yang, Y. Guo, Y. Ma, C. Wan, Y. Cui, M. Li, X. Chen, Surface nanostructures formation induced by highly charged ions: Kinetic and potential energy dependence, *Nucl. Instrum. Methods Phys. Res. Sect. B Beam Interact. Mater. At.* 513 (2022) 14–20. <https://doi.org/10.1016/j.nimb.2021.12.015>.
- [47] N. Ishikawa, T. Taguchi, N. Okubo, Hillocks created for amorphizable and non-amorphizable ceramics irradiated with swift heavy ions: TEM study, *Nanotechnology* 28 (2017) 445708. <https://doi.org/10.1088/1361-6528/aa8778>.
- [48] N. Khalfaoui, C.C. Rotaru, S. Bouffard, E. Jacquet, H. Lebius, M. Toulemonde, Study of swift heavy ion tracks on crystalline quartz surfaces, *Nucl. Instrum. Methods Phys. Res. Sect. B Beam Interact. Mater. At.* 209 (2003) 165–169. [https://doi.org/10.1016/S0168-583X\(02\)02014-1](https://doi.org/10.1016/S0168-583X(02)02014-1).
- [49] N. Khalfaoui, C.C. Rotaru, S. Bouffard, M. Toulemonde, J.P. Stoquert, F. Haas, C. Trautmann, J. Jensen, A. Dunlop, Characterization of swift heavy ion tracks in CaF₂ by scanning force and transmission electron microscopy, *Nucl. Instrum. Methods Phys. Res. Sect. B Beam Interact. Mater. At.* 240 (2005) 819–828. <https://doi.org/10.1016/j.nimb.2005.06.220>.
- [50] W. Li, X. Zhan, X. Song, S. Si, R. Chen, J. Liu, Z. Wang, J. He, X. Xiao, A Review of Recent Applications of Ion Beam Techniques on Nanomaterial Surface Modification: Design of Nanostructures and Energy Harvesting, *Small* 15 (2019) 1901820. <https://doi.org/10.1002/sml.201901820>.
- [51] J. Muñoz-García, L. Vázquez, R. Cuerno, J.A. Sánchez-García, M. Castro, R. Gago, Self-Organized Surface Nanopatterning by Ion Beam Sputtering, in: Z.M. Wang (Ed.), *Funct. Nanomater.*, Springer US, New York, NY, 2009: pp. 323–398. https://doi.org/10.1007/978-0-387-77717-7_10.
- [52] A. Niggas, J. Buck, D. Thima, V. Vojtech, F. Vuković, M. Werl, K. Rossnagel, R.A. Wilhelm, Chirality Switching in 1T-TaS₂ by Highly Charged Ion Irradiation, *Nano Lett.* (2026) acs.nanolett.5c04268. <https://doi.org/10.1021/acs.nanolett.5c04268>.
- [53] F. Aumayr, S. Facsko, A.S. El-Said, C. Trautmann, M. Schleberger, Single ion induced surface nanostructures: a comparison between slow highly charged and swift heavy ions, *J. Phys. Condens. Matter* 23 (2011) 393001. <https://doi.org/10.1088/0953-8984/23/39/393001>.
- [54] A.S. El-Said, R.A. Wilhelm, R. Heller, M. Sorokin, S. Facsko, F. Aumayr, Tuning the Fabrication of Nanostructures by Low-Energy Highly Charged Ions, *Phys. Rev. Lett.* 117 (2016) 126101. <https://doi.org/10.1103/PhysRevLett.117.126101>.
- [55] A. Müller, C. Müller, R. Neumann, F. Ohnesorge, Scanning force microscopy of heavy-ion induced damage in lithium fluoride single-crystals, *Nucl. Instrum. Methods Phys. Res. Sect. B Beam Interact. Mater. At.* 166–167 (2000) 581–585. [https://doi.org/10.1016/S0168-583X\(99\)00791-0](https://doi.org/10.1016/S0168-583X(99)00791-0).

- [56] F. Frost, B. Ziberi, T. Höche, B. Rauschenbach, The shape and ordering of self-organized nanostructures by ion sputtering, *Nucl. Instrum. Methods Phys. Res. Sect. B Beam Interact. Mater. At.* 216 (2004) 9–19. <https://doi.org/10.1016/j.nimb.2003.11.014>.
- [57] I. Sulania, D. Agarwal, M. Husain, D.K. Avasthi, Investigations of ripple pattern formation on Germanium surfaces using 100-keV Ar⁺ ions, *Nanoscale Res. Lett.* 10 (2015) 88. <https://doi.org/10.1186/s11671-015-0751-4>.
- [58] A.S. El-Said, R. Heller, R.A. Wilhelm, S. Facsko, F. Aumayr, Surface modifications of BaF₂ and CaF₂ single crystals by slow highly charged ions, *Appl. Surf. Sci.* 310 (2014) 169–173. <https://doi.org/10.1016/j.apusc.2014.03.083>.
- [59] R. Heller, S. Facsko, R.A. Wilhelm, W. Möller, Defect Mediated Desorption of the KBr(001) Surface Induced by Single Highly Charged Ion Impact, *Phys. Rev. Lett.* 101 (2008) 096102. <https://doi.org/10.1103/PhysRevLett.101.096102>.
- [60] C. Müller, M. Cranney, A. El-Said, N. Ishikawa, A. Iwase, M. Lang, R. Neumann, Ion tracks on LiF and CaF₂ single crystals characterized by scanning force microscopy, *Nucl. Instrum. Methods Phys. Res. Sect. B Beam Interact. Mater. At.* 191 (2002) 246–250. [https://doi.org/10.1016/S0168-583X\(02\)00569-4](https://doi.org/10.1016/S0168-583X(02)00569-4).
- [61] I. Hanif, O. Camara, M.A. Tunes, R.W. Harrison, G. Greaves, S.E. Donnelly, J.A. Hinks, Ion-beam-induced bending of semiconductor nanowires, *Nanotechnology* 29 (2018) 335701. <https://doi.org/10.1088/1361-6528/aac659>.
- [62] Z. Razaghi, D.Y. Xie, M. Lin, G. Zhu, Ion beam-induced bending of TiO₂ nanowires with bead-like and prismatic shapes, *RSC Adv.* 12 (2022) 5577–5586. <https://doi.org/10.1039/D1RA09122K>.
- [63] S. Korkos, V. Jantunen, K. Arstila, T. Sajavaara, A. Leino, K. Nordlund, F. Djurabekova, Nanorod orientation control by swift heavy ion irradiation, *Appl. Phys. Lett.* 120 (2022) 171602. <https://doi.org/10.1063/5.0089028>.
- [64] X.D. Zheng, The influence of ion implantation-induced oxygen vacancy on electrical conductivity of WO₃ thin films, *Vacuum* 165 (2019) 46–50. <https://doi.org/10.1016/j.vacuum.2019.04.004>.
- [65] K. Dworecki, T. Hasegawa, K. Sudlitz, A. Ślęzak, S. Wąsik, Modification of electrical properties of polymer membranes by ion implantation (II), *Nucl. Instrum. Methods Phys. Res. Sect. B Beam Interact. Mater. At.* 185 (2001) 61–65. [https://doi.org/10.1016/S0168-583X\(01\)00779-0](https://doi.org/10.1016/S0168-583X(01)00779-0).
- [66] B. Savoini, M.M. Tardío, R. Ramírez, E. Alves, Surface morphology, thermal and electrical conductivity of α -Al₂O₃ single crystals implanted with Au and Ag ions, *Nucl. Instrum. Methods Phys. Res. Sect. B Beam Interact. Mater. At.* 286 (2012) 184–189. <https://doi.org/10.1016/j.nimb.2011.11.036>.
- [67] M.A. Syzgantseva, C.P. Ireland, F.M. Ebrahim, B. Smit, O.A. Syzgantseva, Metal Substitution as the Method of Modifying Electronic Structure of Metal–Organic Frameworks, *J. Am. Chem. Soc.* 141 (2019) 6271–6278. <https://doi.org/10.1021/jacs.8b13667>.
- [68] J. Kim, S. Saremi, M. Acharya, G. Velarde, E. Parsonnet, P. Donahue, A. Qualls, D. Garcia, L.W. Martin, Ultrahigh capacitive energy density in ion-bombarded relaxor ferroelectric films, *Science* 369 (2020) 81–84. <https://doi.org/10.1126/science.abb0631>.
- [69] S. Saremi, R. Xu, L.R. Dedon, J.A. Mundy, S. Hsu, Z. Chen, A.R. Damodaran, S.P. Chapman, J.T. Evans, L.W. Martin, Enhanced Electrical Resistivity and Properties via Ion Bombardment of Ferroelectric Thin Films, *Adv. Mater.* 28 (2016) 10750–10756. <https://doi.org/10.1002/adma.201603968>.

- [70] A.N. Mikhaylov, A.I. Belov, D.S. Korolev, S.A. Gerasimova, I.N. Antonov, E.V. Okulich, R.A. Shuiskiy, D.I. Tetelbaum, Effect of ion irradiation on resistive switching in metal-oxide memristive nanostructures, *J. Phys. Conf. Ser.* 1410 (2019) 012245. <https://doi.org/10.1088/1742-6596/1410/1/012245>.
- [71] X. Pan, Y. Shuai, C. Wu, L. Zhang, H. Guo, H. Cheng, Y. Peng, S. Qiao, W. Luo, T. Wang, X. Sun, H. Zeng, J. Zhang, W. Zhang, X. Ou, N. Du, H. Schmidt, Ar⁺ ions irradiation induced memristive behavior and neuromorphic computing in monolithic LiNbO₃ thin films, *Appl. Surf. Sci.* 484 (2019) 751–758. <https://doi.org/10.1016/j.apsusc.2019.04.114>.
- [72] E.V. Okulich, V.I. Okulich, D.I. Tetelbaum, Impact of Oxygen Vacancies on the Formation and Structure of Filaments in SiO₂-Based Memristors, *Tech. Phys. Lett.* 46 (2020) 19–22. <https://doi.org/10.1134/S1063785020010083>.
- [73] S. Hirose, A. Nakayama, H. Niimi, K. Kageyama, H. Takagi, Improvement in Resistance Switching and Retention Properties of PtTiO₂ Schottky Junction Devices, *J. Electrochem. Soc.* 158 (2011) H261. <https://doi.org/10.1149/1.3529247>.
- [74] R. Zhou, C. Calahoo, Y. Ding, L. Wondraczek, Role of Ag⁺ Ions in Determining Ce³⁺ Optical Properties in Fluorophosphate and Sulfophosphate Glasses, *ACS Omega* 6 (2021) 30093–30107. <https://doi.org/10.1021/acsomega.1c04933>.
- [75] B. Priya, P. Jasrotia, I. Sulania, V. Singh, R. Kumar, T. Kumar, Structural and Optical Properties of N⁺ Implanted V₂O₅ Thin Film on Glass Substrate, *ECS J. Solid State Sci. Technol.* 12 (2023) 105008. <https://doi.org/10.1149/2162-8777/ad041c>.
- [76] T. Yoneda, D. Eglyna, T. Negami, T. Minemoto, Investigation of the interplay of oxygen presence and Mg addition on InZnO:Al and InZnMgO:Al Thin Films, *Thin Solid Films* 828 (2025) 140793. <https://doi.org/10.1016/j.tsf.2025.140793>.
- [77] B.M.S. Teixeira, A.A. Timopheev, N. Caçoilo, L. Cuchet, J. Mondaud, J.R. Childress, S. Magalhães, E. Alves, N.A. Sobolev, Ar⁺ ion irradiation of magnetic tunnel junction multilayers: impact on the magnetic and electrical properties, *J. Phys. Appl. Phys.* 53 (2020) 455003. <https://doi.org/10.1088/1361-6463/aba38c>.
- [78] K.P. Mondal, S. Bera, A. Gupta, R. Kumar, G. Das, G. Manna, N. Ito, Y. Yamada-Takamura, Tailoring the magnetic properties of Co₂₀Fe₆₀B₂₀/SmCo₅ bilayers: Effects of argon ion implantation, *Mater. Lett.* 316 (2022) 131875. <https://doi.org/10.1016/j.matlet.2022.131875>.
- [79] J. Ferré, T. Devolder, H. Bernas, J.P. Jamet, V. Repain, M. Bauer, N. Vernier, C. Chappert, Magnetic phase diagrams of He ion-irradiated Pt/Co/Pt ultrathin films, *J. Phys. Appl. Phys.* 36 (2003) 3103–3108. <https://doi.org/10.1088/0022-3727/36/24/002>.
- [80] P. Ström, C. Vantaraki, R. Kaur, T.T. Tran, G. Nagy, V. Kapaklis, D. Primetzhofer, Position-Selective Introduction of Ferromagnetism on the Micro- and Nanoscale in a Paramagnetic Thin Palladium Film, *Phys. Status Solidi RRL – Rapid Res. Lett.* 18 (2024) 2400053. <https://doi.org/10.1002/pssr.202400053>.
- [81] J. Fassbender, J. McCord, Magnetic patterning by means of ion irradiation and implantation, *J. Magn. Magn. Mater.* 320 (2008) 579–596. <https://doi.org/10.1016/j.jmmm.2007.07.032>.

- [82] C. Vantaraki, P. Ström, T.T. Tran, M.P. Grassi, G. Fevola, M. Foerster, J.T. Sadowski, D. Primetzhofer, V. Kapaklis, Magnetic metamaterials by ion-implantation, *Appl. Phys. Lett.* 125 (2024) 202403. <https://doi.org/10.1063/5.0239106>.
- [83] R.J. Rodríguez, J.A. García, R. Sánchez, A. Pérez, B. Garrido, J. Morante, Modification of surface mechanical properties of polycarbonate by ion-implantation, *Surf. Coat. Technol.* 158–159 (2002) 636–642. [https://doi.org/10.1016/S0257-8972\(02\)00322-5](https://doi.org/10.1016/S0257-8972(02)00322-5).
- [84] H. Zhang, Q. Wang, C. Li, Z. Zhu, H. Huang, Y. Lu, He-ion Irradiation Effects on the Microstructures and Mechanical Properties of the Ti-Zr-Hf-V-Ta Low-Activation High-Entropy Alloys, *Materials* 16 (2023) 5530. <https://doi.org/10.3390/ma16165530>.
- [85] S.A. Shojaee, Y. Qi, Y.Q. Wang, A. Mehner, D.A. Lucca, Ion irradiation induced structural modifications and increase in elastic modulus of silica based thin films, *Sci. Rep.* 7 (2017) 40100. <https://doi.org/10.1038/srep40100>.
- [86] R.L. Fleisher, P.B. Price, R.M. Walker, Nuclear tracks in solids: Principles and applications, 1975. <https://ui.adsabs.harvard.edu/abs/1975ucb..book.....F> (accessed August 4, 2023).
- [87] J.A. Van Vechten, R. Tsu, F.W. Saris, D. Hoonhout, Reasons to believe pulsed laser annealing of Si does not involve simple thermal melting, *Phys. Lett. A* 74 (1979) 417–421. [https://doi.org/10.1016/0375-9601\(79\)90241-X](https://doi.org/10.1016/0375-9601(79)90241-X).
- [88] P. Stampfli, K.H. Bennemann, Time dependence of the laser-induced femto-second lattice instability of Si and GaAs: Role of longitudinal optical distortions, *Phys. Rev. B* 49 (1994) 7299–7305. <https://doi.org/10.1103/PhysRevB.49.7299>.
- [89] N. Itoh, Self-trapped exciton model of heavy-ion track registration, *Nucl. Instrum. Methods Phys. Res. Sect. B Beam Interact. Mater. At.* 116 (1996) 33–36. [https://doi.org/10.1016/0168-583X\(96\)00006-7](https://doi.org/10.1016/0168-583X(96)00006-7).
- [90] B. Canut, S.M.M. Ramos, The concept of effective electronic stopping power for modelling the damage cross-section in refractory oxides irradiated by GeV ions or MeV clusters, *Radiat. Eff. Defects Solids* 145 (1998) 1–27. <https://doi.org/10.1080/10420159808220019>.
- [91] M. Toulemonde, Ch. Dufour, A. Meftah, E. Paumier, Transient thermal processes in heavy ion irradiation of crystalline inorganic insulators, *Nucl. Instrum. Methods Phys. Res. Sect. B Beam Interact. Mater. At.* 166–167 (2000) 903–912. [https://doi.org/10.1016/S0168-583X\(99\)00799-5](https://doi.org/10.1016/S0168-583X(99)00799-5).
- [92] J.-M. Costantini, S. Miro, G. Gutierrez, K. Yasuda, S. Takaki, N. Ishikawa, M. Toulemonde, Raman spectroscopy study of damage induced in cerium dioxide by swift heavy ion irradiations, *J. Appl. Phys.* 122 (2017) 205901. <https://doi.org/10.1063/1.5011165>.
- [93] G. Szenes, Thermal spike model of amorphous track formation in insulators irradiated by swift heavy ions, *Nucl. Instrum. Methods Phys. Res. Sect. B Beam Interact. Mater. At.* 116 (1996) 141–144. [https://doi.org/10.1016/0168-583X\(96\)00025-0](https://doi.org/10.1016/0168-583X(96)00025-0).
- [94] M. Toulemonde, E. Paumier, C. Dufour, Thermal spike model in the electronic stopping power regime, *Radiat. Eff. Defects Solids* 126 (1993) 201–206. <https://doi.org/10.1080/10420159308219709>.
- [95] P. Sigmund, C. Claussen, Sputtering from elastic-collision spikes in heavy-ion-bombarded metals, *J. Appl. Phys.* 52 (1981) 990–993. <https://doi.org/10.1063/1.328790>.

- [96] G. Szenes, General features of latent track formation in magnetic insulators irradiated with swift heavy ions, *Phys. Rev. B* 51 (1995) 8026–8029. <https://doi.org/10.1103/PhysRevB.51.8026>.
- [97] G. Szenes, Ion-velocity-dependent track formation in yttrium iron garnet: A thermal-spike analysis, *Phys. Rev. B* 52 (1995) 6154–6157. <https://doi.org/10.1103/PhysRevB.52.6154>.
- [98] B. Gervais, S. Bouffard, Simulation of the primary stage of the interaction of swift heavy ions with condensed matter, *Nucl. Instrum. Methods Phys. Res. Sect. B Beam Interact. Mater. At.* 88 (1994) 355–364. [https://doi.org/10.1016/0168-583X\(94\)95384-8](https://doi.org/10.1016/0168-583X(94)95384-8).
- [99] Z. Chunxiang, D.E. Dunn, R. Katz, Radial Distribution of Dose and Cross-Sections for the Inactivation of Dry Enzymes and Viruses, *Radiat. Prot. Dosimetry* 13 (1985) 215–218. <https://doi.org/10.1093/rpd/13.1-4.215>.
- [100] M.P.R. Waligórski, R.N. Hamm, R. Katz, The radial distribution of dose around the path of a heavy ion in liquid water, *Int. J. Radiat. Appl. Instrum. Part Nucl. Tracks Radiat. Meas.* 11 (1986) 309–319. [https://doi.org/10.1016/1359-0189\(86\)90057-9](https://doi.org/10.1016/1359-0189(86)90057-9).
- [101] Z.G. Wang, C. Dufour, E. Paumier, M. Toulemonde, The S_e sensitivity of metals under swift-heavy-ion irradiation: a transient thermal process, *J. Phys. Condens. Matter* 6 (1994) 6733–6750. <https://doi.org/10.1088/0953-8984/6/34/006>.
- [102] M. Toulemonde, W. Assmann, Y. Zhang, M. Backman, W.J. Weber, C. Dufour, Z.G. Wang, Material Transformation: Interaction between Nuclear and Electronic Energy Losses, *Procedia Mater. Sci.* 7 (2014) 272–277. <https://doi.org/10.1016/j.mspro.2014.10.035>.
- [103] P. Patra, S. Shah, M. Toulemonde, I. Sulania, F. Singh, Investigation of radiation damage using thermal spike model for SHI irradiation on Al_2O_3 , *Radiat. Eff. Defects Solids* 177 (2022) 513–530. <https://doi.org/10.1080/10420150.2022.2048658>.
- [104] M. Toulemonde, W.J. Weber, G. Li, V. Shutthanandan, P. Kluth, T. Yang, Y. Wang, Y. Zhang, Synergy of nuclear and electronic energy losses in ion-irradiation processes: The case of vitreous silicon dioxide, *Phys. Rev. B* 83 (2011) 054106. <https://doi.org/10.1103/PhysRevB.83.054106>.
- [105] P. Ström, D. Primetzhöfer, Ion beam tools for nondestructive in-situ and in-operando composition analysis and modification of materials at the Tandem Laboratory in Uppsala, *J. Instrum.* 17 (2022) P04011. <https://doi.org/10.1088/1748-0221/17/04/P04011>.
- [106] F. Sekula, MeV ion irradiation beamline at the Uppsala tandem accelerator: improvements and applications, Brno University of Technology, 2020.
- [107] A. Hallén, P.A. Ingemarsson, P. Håkansson, B.U.R. Sundqvist, G. Possnert, An MeV-ion implanter for large area applications, *Nucl. Instrum. Methods Phys. Res. Sect. B Beam Interact. Mater. At.* 36 (1989) 345–349. [https://doi.org/10.1016/0168-583X\(89\)90679-4](https://doi.org/10.1016/0168-583X(89)90679-4).
- [108] W. Kern, Overview and Evolution of Silicon Wafer Cleaning Technology *, in: *Handb. Silicon Wafer Clean. Technol.*, Elsevier, 2018: pp. 3–85. <https://doi.org/10.1016/B978-0-323-51084-4.00001-0>.
- [109] T.J. Mason, Ultrasonic cleaning: An historical perspective, *Ultrason. Sonochem.* 29 (2016) 519–523. <https://doi.org/10.1016/j.ultsonch.2015.05.004>.
- [110] C. Trautmann, W. Bröchle, R. Spohr, J. Vetter, N. Angert, Pore geometry of etched ion tracks in polyimide, *Nucl. Instrum. Methods Phys. Res. Sect. B Beam Interact. Mater. At.* 111 (1996) 70–74. [https://doi.org/10.1016/0168-583X\(95\)01264-8](https://doi.org/10.1016/0168-583X(95)01264-8).

- [111] S. Metz, C. Trautmann, A. Bertsch, P. Renaud, Polyimide microfluidic devices with integrated nanoporous filtration areas manufactured by micromachining and ion track technology, *J. Micromechanics Microengineering* 14 (2004) 324–331. <https://doi.org/10.1088/0960-1317/14/3/002>.
- [112] I.M. Kolthoff, E.B. Sandell, *Textbook of Quantitative Inorganic Analysis*, 3. ed., Macmillan, 1952.
- [113] P. Borowski, J. Myśliwiec, Recent Advances in Magnetron Sputtering: From Fundamentals to Industrial Applications, *Coatings* 15 (2025) 922. <https://doi.org/10.3390/coatings15080922>.
- [114] J.T. Gudmundsson, Physics and technology of magnetron sputtering discharges, *Plasma Sources Sci. Technol.* 29 (2020) 113001. <https://doi.org/10.1088/1361-6595/abb7bd>.
- [115] S. Liu, X. Li, Y. Hao, X. Li, F. Liu, Effect of magnetron sputtering process parameters on the conductivity of thin metal film, *AIP Adv.* 13 (2023) 095326. <https://doi.org/10.1063/5.0170746>.
- [116] P. Bousoulas, I. Michelakaki, D. Tsoukalas, Influence of oxygen content of room temperature TiO_{2-x} deposited films for enhanced resistive switching memory performance, *J. Appl. Phys.* 115 (2014) 034516. <https://doi.org/10.1063/1.4862797>.
- [117] Z. Qiao, D. Mergel, Comparison of radio-frequency and direct-current magnetron sputtered thin $\text{In}_2\text{O}_3:\text{Sn}$ films, *Thin Solid Films* 484 (2005) 146–153. <https://doi.org/10.1016/j.tsf.2005.02.006>.
- [118] J. Shams-Latifi, E. Pitthan, T.T. Tran, R. Kaur, D. Primetzhofer, Sputter-deposition of ultra-thin film stacks from EUROFER97 and tungsten: characterisation and interaction with low-energy D and He ions, *Mater. Res. Express* 11 (2024) 016518. <https://doi.org/10.1088/2053-1591/ad1f97>.
- [119] C. Jeynes, R.P. Webb, A. Lohstroh, Ion Beam Analysis: A Century of Exploiting the Electronic and Nuclear Structure of the Atom for Materials Characterisation, *Rev. Accel. Sci. Technol.* 04 (2011) 41–82. <https://doi.org/10.1142/S1793626811000483>.
- [120] C. Jeynes, J.L. Colaux, Thin film depth profiling by ion beam analysis, *The Analyst* 141 (2016) 5944–5985. <https://doi.org/10.1039/C6AN01167E>.
- [121] M. Nastasi, J. Mayer, J.K. Hirvonen, *Ion-solid interactions: Fundamentals and Applications*, Cambridge University Press, Cambridge, UK, 1996.
- [122] C.R. Gossett, Non-Rutherford elastic backscattering for light element cross section enhancement, *Nucl. Instrum. Methods Phys. Res. Sect. B Beam Interact. Mater. At.* 40–41 (1989) 813–816. [https://doi.org/10.1016/0168-583X\(89\)90484-9](https://doi.org/10.1016/0168-583X(89)90484-9).
- [123] Ion Beam Analysis Nuclear Data Library (IBANDL), *Ion Beam Anal. Nucl. Data Libr. IBANDL* (n.d.). <http://www-nds.iaea.org/ibandl/> (accessed October 11, 2023).
- [124] A.F. Gurbich, SigmaCalc recent development and present status of the evaluated cross-sections for IBA, *Nucl. Instrum. Methods Phys. Res. Sect. B Beam Interact. Mater. At.* 371 (2016) 27–32. <https://doi.org/10.1016/j.nimb.2015.09.035>.
- [125] K. Arstila, J. Julin, M.I. Laitinen, J. Aalto, T. Konu, S. Kärkkäinen, S. Rahkonen, M. Raunio, J. Itonen, J.-P. Santanen, T. Tuovinen, T. Sajavaara, Potku – New analysis software for heavy ion elastic recoil detection analysis, *Nucl. Instrum. Methods Phys. Res. Sect. B Beam Interact. Mater. At.* 331 (2014) 34–41. <https://doi.org/10.1016/j.nimb.2014.02.016>.

- [126] K. Komander, P. Malinovskis, G.K. Pálsson, M. Wolff, D. Primetzhofer, Accurate measurement of hydrogen concentration in transition metal hydrides utilizing electronic excitations by MeV ions, *Int. J. Hydrog. Energy* 57 (2024) 583–588. <https://doi.org/10.1016/j.ijhydene.2024.01.032>.
- [127] E. Pitthan, M.V. Moro, S.A. Corrêa, D. Primetzhofer, Assessing boron quantification and depth profiling of different boride materials using ion beams, *Surf. Coat. Technol.* 417 (2021) 127188. <https://doi.org/10.1016/j.surfcoat.2021.127188>.
- [128] S.A. Corrêa, E. Pitthan, M.V. Moro, D. Primetzhofer, A multipurpose set-up using keV ions for nuclear reaction analysis, high-resolution backscattering spectrometry, low-energy PIXE and in-situ irradiation experiments, *Nucl. Instrum. Methods Phys. Res. Sect. B Beam Interact. Mater. At.* 478 (2020) 104–110. <https://doi.org/10.1016/j.nimb.2020.05.023>.
- [129] C. Driemeier, L. Miotti, R.P. Pezzi, K.P. Bastos, I.J.R. Baumvol, The use of narrow nuclear resonances in the study of alternative metal-oxide–semiconductor structures, *Nucl. Instrum. Methods Phys. Res. Sect. B Beam Interact. Mater. At.* 249 (2006) 278–285. <https://doi.org/10.1016/j.nimb.2006.04.013>.
- [130] J.I. Goldstein, D.E. Newbury, J.R. Michael, N.W.M. Ritchie, J.H.J. Scott, D.C. Joy, *Scanning Electron Microscopy and X-Ray Microanalysis*, Springer New York, New York, NY, 2018. <https://doi.org/10.1007/978-1-4939-6676-9>.
- [131] P.E. Batson, N. Dellby, O.L. Krivanek, Sub-ångstrom resolution using aberration corrected electron optics, *Nature* 418 (2002) 617–620. <https://doi.org/10.1038/nature00972>.
- [132] P. Tizro, C. Choi, N. Khanlou, Sample Preparation for Transmission Electron Microscopy, in: W.H. Yong (Ed.), *Biobanking*, Springer New York, New York, NY, 2019: pp. 417–424. https://doi.org/10.1007/978-1-4939-8935-5_33.
- [133] H. Wen, Y. Lin, D.N. Seidman, J.M. Schoenung, I.J. Van Rooyen, E.J. Lavernia, An Efficient and Cost-Effective Method for Preparing Transmission Electron Microscopy Samples from Powders, *Microsc. Microanal.* 21 (2015) 1184–1194. <https://doi.org/10.1017/S1431927615014695>.
- [134] M.Z. Baykara, U.D. Schwarz, Atomic Force Microscopy: Methods and Applications, in: *Encycl. Spectrosc. Spectrom.*, Elsevier, 2017: pp. 70–75. <https://doi.org/10.1016/B978-0-12-409547-2.12141-9>.
- [135] V. Karoutsos, Scanning Probe Microscopy: Instrumentation and Applications on Thin Films and Magnetic Multilayers, *J. Nanosci. Nanotechnol.* 9 (2009). <https://doi.org/10.1166/jnn.2009.1474>.
- [136] D.A. Keen, Total scattering and the pair distribution function in crystallography, *Crystallogr. Rev.* 26 (2020) 143–201. <https://doi.org/10.1080/0889311X.2020.1797708>.
- [137] A.-C. Dippel, M. Roelsgaard, U. Boettger, T. Schneller, O. Gutowski, U. Ruett, Local atomic structure of thin and ultrathin films *via* rapid high-energy X-ray total scattering at grazing incidence, *IUCrJ* 6 (2019) 290–298. <https://doi.org/10.1107/S2052252519000514>.
- [138] The Method of Total Scattering and Atomic Pair Distribution Function Analysis, in: *Pergamon Mater. Ser.*, Elsevier, 2012: pp. 55–111. <https://doi.org/10.1016/B978-0-08-097133-9.00003-4>.
- [139] M. Yoshimoto, Y. Shiramata, PDF analysis using X-ray total scattering — Theory and application examples, *Rigaku J.* 36 (2020).

- [140] K.M.Ø. Jensen, A.B. Blichfeld, S.R. Bauers, S.R. Wood, E. Dooryhée, D.C. Johnson, B.B. Iversen, S.J.L. Billinge, Demonstration of thin film pair distribution function analysis (tfPDF) for the study of local structure in amorphous and crystalline thin films, *IUCrJ* 2 (2015) 481–489. <https://doi.org/10.1107/S2052252515012221>.
- [141] J. Bylin, V. Kapaklis, G.K. Pálsson, Determining pair distribution functions of thin films using laboratory-based X-ray sources, *J. Appl. Crystallogr.* 57 (2024) 1373–1383. <https://doi.org/10.1107/S1600576724006368>.
- [142] A.J. Roberts, C.E. Moffitt, Trends in XPS instrumentation for industrial surface analysis and materials characterisation, *J. Electron Spectrosc. Relat. Phenom.* 231 (2019) 68–74. <https://doi.org/10.1016/j.elspec.2018.03.002>.
- [143] Y. Mikhlin, X-ray Photoelectron Spectroscopy in Mineral Processing Studies, *Appl. Sci.* 10 (2020) 5138. <https://doi.org/10.3390/app10155138>.
- [144] J. Woicik, ed., *Hard X-ray Photoelectron Spectroscopy (HAXPES)*, Springer International Publishing, Cham, 2016. <https://doi.org/10.1007/978-3-319-24043-5>.
- [145] A. Srinath, K. Von Fieandt, S. Fritze, L. Nyholm, E. Lewin, R. Lindblad, Near-surface analysis of magnetron sputtered AlCrNbYZrNx high entropy materials resolved by HAXPES, *Appl. Surf. Sci.* 666 (2024) 160349. <https://doi.org/10.1016/j.apsusc.2024.160349>.
- [146] L. Kövér, X-ray photoelectron spectroscopy using hard X-rays, *J. Electron Spectrosc. Relat. Phenom.* 178–179 (2010) 241–257. <https://doi.org/10.1016/j.elspec.2009.12.004>.
- [147] D. Cohen-Azarzar, M. Baskin, A. Lindblad, F. Trier, L. Kornblum, Scalable and highly tunable conductive oxide interfaces, *APL Mater.* 11 (2023) 111118. <https://doi.org/10.1063/5.0174283>.
- [148] M.H. Engelhard, D.R. Baer, A. Herrera-Gomez, P.M.A. Sherwood, Introductory guide to backgrounds in XPS spectra and their impact on determining peak intensities, *J. Vac. Sci. Technol. Vac. Surf. Films* 38 (2020) 063203. <https://doi.org/10.1116/6.0000359>.
- [149] M. Toulemonde, C. Trautmann, E. Balanzat, K. Hjort, A. Weidinger, Track formation and fabrication of nanostructures with MeV-ion beams, *Nucl. Instrum. Methods Phys. Res. Sect. B Beam Interact. Mater. At.* 216 (2004) 1–8. <https://doi.org/10.1016/j.nimb.2003.11.013>.
- [150] D.S. Jeong, H. Schroeder, U. Breuer, R. Waser, Characteristic electroforming behavior in Pt/TiO₂/Pt resistive switching cells depending on atmosphere, *J. Appl. Phys.* 104 (2008) 123716. <https://doi.org/10.1063/1.3043879>.
- [151] C.-J. Beak, J. Lee, J. Kim, J. Park, S.-H. Lee, Filamentary-based organic memristors for wearable neuromorphic computing systems, *Neuromorphic Comput. Eng.* 4 (2024) 022001. <https://doi.org/10.1088/2634-4386/ad409a>.
- [152] N. Sedghi, H. Li, I.F. Brunell, K. Dawson, R.J. Potter, Y. Guo, J.T. Gibbon, V.R. Dhanak, W.D. Zhang, J.F. Zhang, J. Robertson, S. Hall, P.R. Chalker, The role of nitrogen doping in ALD Ta₂O₅ and its influence on multilevel cell switching in RRAM, *Appl. Phys. Lett.* 110 (2017) 102902. <https://doi.org/10.1063/1.4978033>.

Acta Universitatis Upsaliensis

Digital Comprehensive Summaries of Uppsala Dissertations from the Faculty of Science and Technology 2644

Editor: The Dean of the Faculty of Science and Technology

A doctoral dissertation from the Faculty of Science and Technology, Uppsala University, is usually a summary of a number of papers. A few copies of the complete dissertation are kept at major Swedish research libraries, while the summary alone is distributed internationally through the series Digital Comprehensive Summaries of Uppsala Dissertations from the Faculty of Science and Technology. (Prior to January, 2005, the series was published under the title “Comprehensive Summaries of Uppsala Dissertations from the Faculty of Science and Technology”.)

Distribution: publications.uu.se
urn:nbn:se:uu:diva-580192



ACTA UNIVERSITATIS
UPSALIENSIS
2026